

## ABSTRACT

GANN, ELIOT HUGH. Using Resonant Soft X-rays to Reveal Internal Organic Thin Film Morphology. (Under the direction of Harald Ade).

This dissertation details the establishment and expansion of resonant soft X-ray scattering techniques to reveal the internal structure of organic thin films. These films are increasingly important in numerous electronic systems, including organic thin film transistors, organic photovoltaics, and organic light emitting diodes. These devices use the electrical properties of polymers to respectively turn on and off conduction, turn light into electricity, and create light. The performance of each of these systems depends critically on their physical structure but unfortunately, traditional techniques fail to adequately characterize that structure.

This dissertation will explore the use of soft X-ray scattering to reveal the mesoscale structure of organic electronic devices. This begins with an overview of the field to make the case for soft X-rays being an appropriate and novel tool. Next, to explain how to collect accurate soft X-ray scattering, the development of a new and unique soft X-ray scattering facility will be presented. Having the tools, the next step is to develop scattering theories and models for understanding and correctly analyzing scattering from these complicated devices. This includes development and comparison of analysis techniques and theory to simulate scattering. This simulation system is then used in the development of a theory to understand the novel phenomenon of anisotropic X-ray scattering from isotropic organic samples. Finally, I will describe the development and first use of a method able to simultaneously measure size scales and chemical structure with depth sensitivity in thin films: Grazing Resonant Soft X-ray Scattering. This work provides valuable understanding and tools to the field of materials characterization, opening up new opportunities for principled design of organic electronics.

© Copyright 2013 Eliot Gann

All Rights Reserved

Using Resonant Soft X-rays to Reveal Internal Organic Thin Film Structure

by  
Eliot Gann

A dissertation submitted to the Graduate Faculty of  
North Carolina State University  
in partial fulfillment of the  
requirements for the Degree of  
Doctor of Philosophy

Physics

Raleigh, North Carolina

2013

APPROVED BY:

---

Prof. Harald Ade  
Chair of Advisory Committee

---

Prof. Daniel Dougherty

---

Prof. Maurice Balik

---

Prof. Michael Paesler

## **DEDICATION**

To my family, who has always supported me.

## **BIOGRAPHY**

Eliot Gann was born June 15, 1983 in Bishop, California. Growing up in the remote Owens Valley, he attended Bishop Union High School, where he graduated as Salutatorian in 2001. He continued to University of California, San Diego where he graduated with Bachelor in Arts in Philosophy and Bachelor of Science in Physics in 2005. For the next three years, he worked as a post baccalaureate fellow at the Advanced Light Source in the Lawrence Berkeley National Laboratory, in Berkeley, California. Here he worked as a member of Experimental Systems Group to develop the Small and Wide Angle X-ray Scattering facility, including the initial building of the hardware, user community and computer control and acquisition software. While working at the lab, he made the decision to pursue a graduate degree in physics, working in the emerging field of soft X-ray scattering that was beginning to be developed at the Advanced Light Source. Having met Professor Harald Ade while working at the Advanced Light Source, Eliot decided to come to North Carolina State University and work with Professor Ade at the forefront of this exciting new field.

## ACKNOWLEDGMENTS

I would like to thank all the people who helped me complete this work. It was a great time in my life, made only better by the friendly helping hands along the way. First, my advisor Harald Ade, who through example and advice has guided my work. Completing this work required a lot of very long days at beamlines 11.0.1.2 and 7.3.3 at the Advanced Light Source. The staffs of these beamlines were often critical in collecting the data presented in this dissertation. Particularly Alex Hexemer and Cheng Wang were instrumental in both planning and carrying out this work. I am thankful to all the beamline staff including Steven Alvarez, Eric Schaible, and Anthony Young for discussions and their help in improving the beamlines. Brian Collins, now at NIST, who as a post graduate fellow for much of my time at NCSU helped me both in developing my analytical and computational skills as well as providing an example of tireless and unrelenting pursuit of science. Hongping Yan, now at Argonne National Lab, then a graduate student, likewise gave me a hand with many of my projects, and was cheerful company for many stressful late nights at the beamline. I'd like to thank all of my group members, who each gave me helpful advice and feedback along the way including John Tumbleston, Ma Wei, Terry McAfee, Anne Watson, Joshua Carpenter, Jaewook Seok, Sen Li, Subhrangsu Mukherjee, Aric Meyer, and Lewis Guignard. I am grateful to each of you for your help and camaraderie through this work.

My collaborators in Chris McNeill's group at Monash University, and in Michael Chabiny's Group at UCSB were all helpful and integral to the success of my projects.

Personally, I would like to acknowledge all the colleagues and friends who helped me through my time here at North Carolina State University. North Carolina has become a home for me over these years, one that will value wherever I end up.

## TABLE OF CONTENTS

<b>LIST OF TABLES .....</b>	<b>ix</b>
<b>LIST OF FIGURES .....</b>	<b>x</b>
<b><i>Chapter 1— CHARACTERIZING SOFT MATERIALS: THE NEED FOR SOFT X-RAY SCATTERING .....</i></b>	<b>1</b>
1.1 ORGANIC ELECTRONICS .....	1
1.1.1 WHAT ARE ORGANIC ELECTRONICS?.....	1
1.1.2 ORGANIC THIN FILM TRANSISTORS .....	2
1.1.3 ORGANIC PHOTOVOLTAICS .....	3
1.1.4 MEASURING ORGANIC DEVICES .....	9
1.2 DIFFICULTIES OF MEASURING MORPHOLOGIES .....	9
1.2.1 MATERIAL CONTRAST .....	10
1.2.2 NEUTRON SCATTERING AND REFLECTIVITY .....	11
1.2.3 ENERGY FILTERED ELECTRON MICROSCOPY .....	11
1.2.4 SOFT X-RAYS.....	12
1.3 SOFT X-RAYS .....	14
1.3.1 RESONANCE.....	14
1.3.2 STXM .....	15
1.3.3 REFLECTIVITY.....	16
1.3.4 SCATTERING .....	17
1.4 SOFT X-RAY SCATTERING .....	17
1.5 THESIS OUTLINE.....	18
<b><i>Chapter 2— SOFT X-RAY SCATTERING FACILITY AT THE ADVANCED LIGHT SOURCE WITH REAL-TIME DATA PROCESSING AND ANALYSIS .....</i></b>	<b>19</b>
2.1 ABSTRACT.....	20
2.2 MOTIVATION AND BACKGROUND.....	20
2.3 BEAMLINE DESCRIPTION .....	23
2.3.1 HARDWARE OF ADVANCED LIGHT SOURCE BEAMLINE 11.0.1.2.....	23
2.3.2 CONTROL ELECTRONICS AND SOFTWARE FOR INSTRUMENT CONTROL AND REAL-TIME ANALYSIS.....	32
2.4 BEAMLINE CHARACTERIZATION.....	34
2.4.1 CHARACTERIZATION SAMPLE PREPARATION .....	34
2.4.2 ENERGY CALIBRATION.....	35
2.4.3 HIGHER ORDER SPECTRAL CONTAMINATION .....	36
2.4.4 POLARIZATION.....	38
2.4.5 DETECTOR CHARACTERISTICS .....	41
2.4.6 DATA COLLECTION AND LIVE ANALYSIS.....	46
2.5 RESULTS.....	48

2.5.1	EXAMPLE OF DATA TILING AND LIMITS OF Q RANGE .....	48
2.5.2	EXAMPLE APPLICATION IN TRANSMISSION GEOMETRY: P3HT:PCBM .....	50
2.5.3	EXAMPLE APPLICATION IN GRAZING INCIDENCE GEOMETRY: BLOCK COPOLYMERS .....	52
2.6	V. DISCUSSION .....	54
2.7	VI. CONCLUSION .....	57
2.8	ACKNOWLEDGEMENTS .....	59
<b>Chapter 3— MODEL FREE ANALYSIS OF SOFT X-RAY SCATTERING IN PHASE SEPARATED SYSTEMS.....</b>		<b>60</b>
3.1	ABSTRACT .....	61
3.2	INTRODUCTION.....	62
3.3	THEORY .....	63
3.3.1	SCATTERING BASICS .....	63
3.3.2	CONTRAST DERIVED .....	65
3.4	BEYOND BORN APPROXIMATION .....	69
3.5	VOLUME FRACTION SIMULATIONS .....	72
3.6	CHORD LENGTH ANALYSIS .....	74
3.7	CONCLUSIONS .....	77
3.8	SUPPLEMENTAL INFORMATION.....	78
<b>Chapter 4— A MODEL FOR SYMMETRY BREAKING AT INTERNAL HETEROINTERFACES EXPLAINS ANISOTROPIC RESONANT X-RAY SCATTERING FROM ISOTROPIC ORGANIC SYSTEMS .....</b>		<b>80</b>
4.1	ABSTRACT:.....	81
4.2	INTRODUCTION.....	82
4.3	MORPHOLOGY MODELING .....	84
4.4	CALCULATING OPTICAL CONSTANTS .....	87
4.4.1	CALCULATING OPTICAL CONSTANTS FROM DFT.....	89
4.5	CALCULATING ALIGNMENT DENSITY.....	89
4.6	SCATTERING SIMULATION.....	90
4.7	TWO DIMENSIONAL SCATTERING PATTERNS.....	92
4.8	AZIMUTHAL SYMMETRIES .....	94
4.9	LORENTZ CORRECTED SCATTERING PATTERNS.....	97
4.10	CALCULATING ANISOTROPIC SIGNAL.....	99
4.11	DISCUSSION.....	103
4.12	CONCLUSION .....	105
4.13	SUPPLEMENTAL INFORMATION.....	106
<b>Chapter 5— X-RAY CONTRAST VARIATION AND WAVE GUIDING REVEAL MESOSCALE STRUCTURE AT BURIED ORGANIC INTERFACES .....</b>		<b>111</b>
5.1	ABSTRACT:.....	112
5.2	REPORT .....	113
5.2.1	ACKNOWLEDGMENTS .....	122

5.3	SUPPLEMENTAL INFORMATION.....	123
5.3.1	DATA ACQUISITION .....	123
5.3.2	PMMA/PEG BILAYER PREPARATION .....	124
5.3.3	PS/PBTTT BILAYER PREPARATION: .....	125
5.3.4	UNCERTAINTY IN MEASUREMENT.....	126
5.3.5	DETAILS OF DATA ANALYSIS:.....	127
5.3.6	CONTRAST: .....	131
5.3.7	EFI CALCULATION:.....	131
5.3.8	ADEQUACY OF PRESENT MODEL.....	135
5.3.9	INTERFACE TRACKING DISCUSSION: .....	136
5.3.10	EXPERIMENTAL FITTING DISCUSSION .....	137
5.3.11	FUTURE APPLICATIONS .....	138
<b>Chapter 6— CONCLUSIONS AND OUTLOOK.....</b>		<b>139</b>
6.1	BEYOND CARBON.....	139
6.2	COMBINING POLARIZATION AND GRAZING INCIDENCE .....	140
6.3	POLARIZED DEPTH-SENSITIVE REFLECTIVITY .....	141
6.4	OUT-OF-PLANE GRSOXS.....	142
6.5	RECIPROCAL SPACE PRINCIPLE COMPONENT ANALYSIS .....	143
6.6	MODEL FREE ANALYSIS – SOLVING FOR CHEMISTRY AND STRUCTURE SIMULTANEOUSLY .....	144
6.7	CONCLUSION .....	146
<b>REFERENCES.....</b>		<b>148</b>

## LIST OF TABLES

Table 1 Mie Scattering Results .....	71
Table 2 Volume Fraction Systems .....	79

## LIST OF FIGURES

Figure 1-1 Schematic of Organic Field Effect Transistor.....	2
Figure 1-2 Schematic of Organic Photovoltaic.....	3
Figure 1-3 Illustration of Molecular Miscibility.....	6
Figure 1-4 Fibrils .....	7
Figure 1-5 Depiction of the Resonance Effect.....	14
Figure 1-6 Illustration of Insensitivity to In-Plane Information .....	16
Figure 2-1 Beamline branch 11.0.1.2 conceptual schematic .....	25
Figure 2-2 Higher harmonic rejection mirror assembly .....	26
Figure 2-3 Views inside of the soft X-ray scattering chamber .....	30
Figure 2-4 Higher Harmonic Rejection Measurements .....	38
Figure 2-5 2D Anisotropic Scattering Map .....	40
Figure 2-6 Histograms of Pixel values.....	43
Figure 2-7. Noise Analysis of Detector .....	46
Figure 2-8 User Interface .....	48
Figure 2-9 Example of Tiling .....	50
Figure 2-10 RSoXS Example.....	51
Figure 2-11 Grazing Incidence Example .....	53
Figure 3-1 Scattering Contrasts .....	66
Figure 3-2 Mie Scattering results.....	70
Figure 3-3 Correlation of Scattering Measurables.....	73
Figure 3-4 Chord Length Analysis .....	74
Figure 3-5 Chord Length in Symmetric System.....	76
Figure 4-1 Morphologies .....	85
Figure 4-2 Optical Constants and Contrasts .....	88
Figure 4-3 Scattering Patterns.....	92
Figure 4-4 Scattering vs. Azimuth Angle – Face-on .....	95
Figure 4-5 Scattering vs. Azimuth Angle – Edge-on.....	96
Figure 4-6 Azimuthally Reduced Scattering.....	98

Figure 4-7 Face On Anisotropy Maps .....	101
Figure 4-8 Edge-on Alignment .....	102
Figure 4-9 Homopolymer Anisotropic Signal .....	104
Figure 4-10 Spheres Alignment Maps Matrix .....	107
Figure 4-11 Spheres Alignment Maps Dispersion.....	107
Figure 4-12 Cylinders Alignment Maps Matrix .....	108
Figure 4-13 Cylinders Alignment Maps Dispersions .....	108
Figure 4-14 Spinodal Decomposition Alignment Maps .....	109
Figure 4-15 Fibrils and Random Alignment Maps .....	109
Figure 5-1 GRSoXS Compared to Other Techniques.....	113
Figure 5-2 PMMA/PEG Theory and Experimental Setup.....	116
Figure 5-3 PMMA PEG GRSoXS Results .....	118
Figure 5-4 GRSoXS Results for OFET Device .....	120
Figure 5-5 AFM images.....	126
Figure 5-6 Data and Fit of PS/PBTTT OFET sample.....	128
Figure 5-7 Scattering patterns from the bare molded PEG.....	130
Figure 5-8 EFI of PMMA/PEG Device .....	133
Figure 5-9 EFI and Contrast of OFET .....	134
Figure 6-1 Reflectivity vs Energy and Momentum Transfer.....	141
Figure 6-2 Out of Plane GRSoXS.....	142
Figure 6-3 Solving for Unknown Refractive Indices from Contrast .....	145

# *Chapter 1*

## **CHARACTERIZING ORGANIC ELECTRONICS: THE NEED FOR SOFT X-RAY SCATTERING**

### 1.1 ORGANIC ELECTRONICS

#### 1.1.1 WHAT ARE ORGANIC ELECTRONICS?

Organic materials are carbon based. For the purpose of this paper, this largely means small molecules or polymers, which are chains of identical small molecules, composed mainly of carbon, hydrogen, nitrogen, and oxygen. Many of these materials have minority components including sulfur, fluorine and other low Z atoms. While organic materials have been very popular in structural applications for their ease of processing and inexpensive fabrication [2], in the 1980s a new class of polymers were found which had useful electronic properties as well. Conjugated bonding condition of carbon, which is alternating single and double bonds around a ring or in an extended chain, allows orbitals to extend across a molecule, and along the backbone of a polymer chain. The orbital overlap caused by conjugation adds to rigidity and also allows conduction of holes and electrons. While the electrical properties of polymers are often far lower than higher Z alternatives [1, 3], the ease of production with mass production techniques like roll to roll processing, when combined with the appealing mechanical properties (i.e. flexibility), have promise to overcome the relatively lower performance and create new categories of electronics. Already well established, and growing in application, Organic Light Emitting Diodes (OLEDs) [4] are commercialized, providing low cost, low voltage, flexible light sources in portable and weight sensitive applications. Emerging

fields, which will be the center of the work presented in this dissertation, include organic thin film transistors [5-8] (OTFTs), useful for thin, transparent, flexible electronics, and organic photovoltaics [9-12] (OPVs) which offer a cheap and mass-producible way to turn sunlight into electricity. The challenges of these two device types lead to two distinct device geometries, but both rely critically on interfaces between organic materials. Both of these geometries, planar and mixtures described below can be well characterized by soft X-ray scattering.

### 1.1.2 ORGANIC THIN FILM TRANSISTORS

Thin film transistors are largely planar in nature, typically a layer of a semiconducting material on top of a gate dielectric material, often a silicon oxide in test cells, but generally high k polymer dielectrics in final application. These cells function by field enhanced carrier concentration, meaning that when an electric field is applied to the material, mobile carriers concentrate at the edge of the material, and when the concentration is high enough, conduction is allowed [13]. Thus these devices are field effect transistors, and are often also called Organic Field Effect Transistors, or OFETs. When the gate field is turned off, the carriers diffuse back

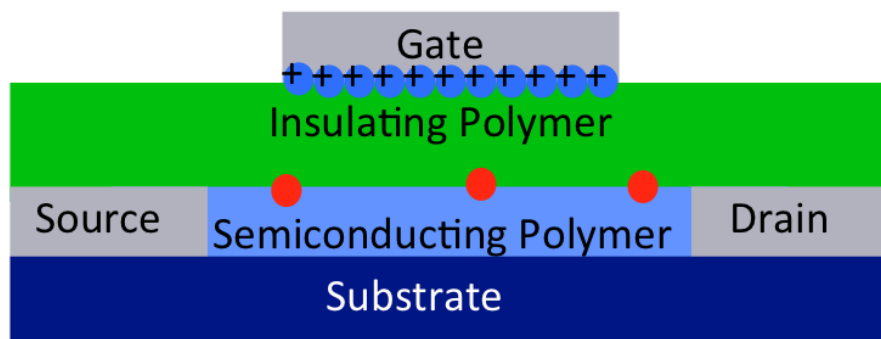


**Figure 1-1 Schematic of Organic Field Effect Transistor**

Drawing of a top gate organic thin film transistor. When the gate is charged (blue circles), the field draws carriers (red circles) to the surface of the semiconducting polymer, allowing conduction between the source and drain. In the illustrated case, a positive bias of the gate, attracts electrons to the surface, where they can conduct between the source and drain.

into the polymer, and conduction effectively ceases. It was shown recently that the location of charge transport and carrier enhancement is essentially right at the interface between the semiconducting polymer and the gate dielectric, and the transport is largely two dimensional in nature [14]. This leads to the natural concern about what exactly is happening at this interface. Many studies have tried to measure the nature of this interface, including the electronic states, [15] the crystal structure [16] and the topography [17], but as of yet, the structural information gained is unclear, and the actual interaction region between the polymers is unknown. The development of GRSoXS, presented in Chapter 5, addresses this problem with a unique method of measuring the interfacial structure.

### 1.1.3 ORGANIC PHOTOVOLTAICS

An effort to develop low cost and flexible solar cells which can be quickly and easily mass produced has been growing intensely recently with concerns of energy sources being

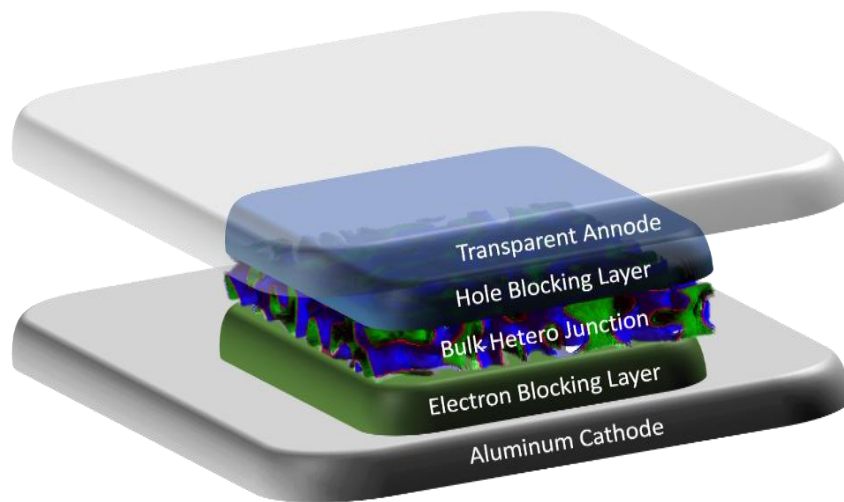


**Figure 1-2 Schematic of Organic Photovoltaic**

Illustration of an idealized structure of a typical organic photovoltaic device. Carriers generated in the Bulk heterojunction at the interface (red) travel through their respective materials (blue is donor, green is acceptor) through the respective blocking layer to the contacts, generating current.

unsustainable and increasingly expensive. Traditional solar cells based on silicon are quite effective at capturing light, but lacking in affordable scalability, particularly when compared with mass production techniques such as roll to roll processing [10] available with polymers. With the discovery of polymeric materials which can be made into solar cells from solution processing [18], it was quickly seen that such systems, if they could be made more efficient could be a viable energy source. Indeed, solar cells composed of mixtures of polymers and fullerene-derivative small molecules in the time of my graduate career have gone from 4% [19] to more than 10% [20] efficiency in test cells, and now companies like Solarmer and Helitek are creating polymeric solar cells as consumer products.

Despite the success over the last few years, fundamentals of how these devices function remain mysterious. The paradigm of a bicontinuous demixing of the materials into pure phases of electron donor and acceptor molecules (Figure 1.2) have been shown, in part by our 2010 paper [21] to be fundamentally flawed, and much more complex morphologies have been suggested. Unfortunately many of these morphologies differ at the nanoscale. Different materials with different crystallinities, molecular weights, miscibilities, and different fullerene derivatives have all been tried, and to some extent there has been success in all avenues [22, 23]. A single governing paradigm of what makes a good device has not been reached.

#### 1.1.3.1 Functioning of Organic Photovoltaics

Measurements on pure materials have revealed that when visual light hits these materials, free carriers are not usually created, but rather a bound electron hole pair is created, called an exciton. Measurements have revealed that the exciton diffusion length is generally <20 nm [24]. However, in order to collect enough light to have a hope of reaching high

efficiency, devices at least 100 nm thick are necessary [25]. Thus the conceptually simpler bilayer design used in other devices, is not an option, and the bulk heterojunction, is typically the only simple way of creating efficient devices, although other approaches have been attempted [26, 27]. In bulk heterojunctions, an exciton created in one material, must move to a material interface, where it can be split into two free carriers, which can then travel to their respective anode or cathode to generate current.

The problem is generally split into five critical parts. First absorption: the light must be effectively turned into excitons in the first place. Thicker devices and more absorptive materials are the obvious avenues to improve this characteristic. Second, exciton diffusion, or getting the created exciton to an interface with the other material. This is aided by small material domains, or from the other point of view lots and lots of interfaces. Next, charge separation, sometimes split into two constituent parts, exciton splitting, when one component (the hole or electron) jumps without its partner across the interface to the other material forming a charge (or in these materials, a polaron, which is a charge along with the lattice distortions which affect its behavior) pair across an interface and dissociation, at which point the polaron pair become free charges. This process is poorly understood, at least in terms of what morphological conditions are favorable for its efficiency. Conceptually a sharper interface is necessary to create an effective field at the interface which can aid the splitting, but also the molecular orientation and specifics of the orbital or band alignment between materials must play a role [28, 29]. Finally, the free charges must make it through the device, and be collected at the cathode or anode respectively. Here interfaces are the enemy, as recombination, and charge trapping, both loss mechanisms, are reduced when there is a clear path to the outside

of the device. At the cathode and anode end, the charges must travel in the correct direction, and be efficiently transferred to the conductor. Blocking and transport layers are important for performance [30], wetting layers in the bulk heterojunction, i.e., the polymer preferentially coating the cathode would block easy charge transport by electrons in the acceptor phase, effectively ruining a device. The careful application of the cathode is also critical to this step [31-33].

### 1.1.3.2 Miscibility

Molecular miscibility complicates this picture dramatically. In our 2010 paper [21], we show that even the “pure” regions of amorphous P3HT, more the 50% of the material, is molecularly mixed with approximately 20% PCBM, leading to the inevitable conclusion that there are potential traps and recombination sites everywhere in the film. Around the same time,

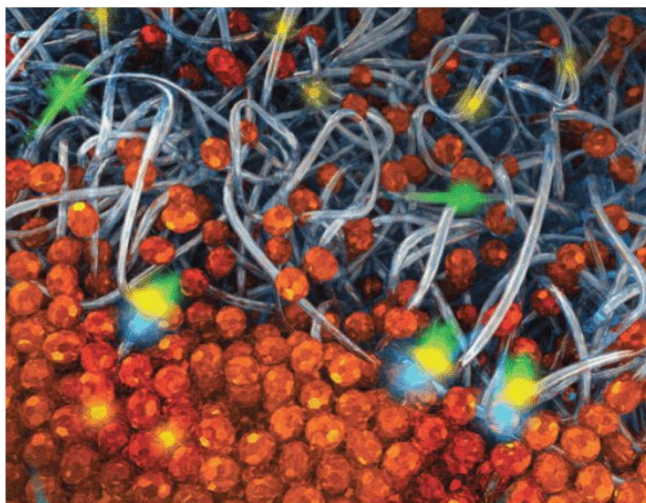


**Figure 1-3 Illustration of Molecular Miscibility**

The orange PCBM particles are shown to be both in pure phase as well as mixed with the polymer. Yellow excitons are split into blue (electron) and green (hole) pairs which travel through the polymer and fullerenes to reach the cathode or anode.

From: Collins, B. A., Li, Z., Tumbleston, J. R., **Gann, E.**, McNeill, C. R. and Ade, H. (2013), Organic Solar Cells: Absolute Measurement of Domain Composition and Nanoscale Size Distribution Explains Performance in PTB7:PC<sub>71</sub>BM Solar Cells (*Adv. Energy Mater.* 1/2013).

several groups looked at the vertical segregation of PCBM P3HT bilayers, showing that upon annealing, the P3HT layer is quickly filled with roughly 20% PCBM by volume [34, 35]. This can explain the relatively low exciton recombination signals measured in these devices, because there is generally always a PCBM molecule nearby, within easy diffusion distance. 20% is above the random three dimensional percolation threshold and so it is possible that molecular percolation paths are sufficient for charge transport. In this case, recombination would not be nearly the problem it was presumed to be, and once the charges separate, it may be rather difficult for them to recombine. If this were the case then this molecular network picture can explain the performance of OPVs despite miscibility.

### 1.1.3.3 Fibrils

Recently there have been reports that the fibrillar nature of P3HT is also a necessary component of performance in bulk heterojunctions, as fibrils can provide a pathway for hole

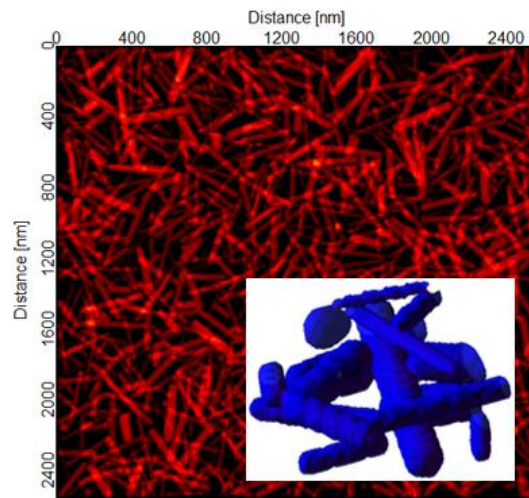


**Figure 1-4 Fibrils**

A simulation of fibrils with inset 3D model created for Chapter 4 based on recent morphology characterization done with energy filtered electron microscopy

conduction while the molecular percolation networks of PCBM handle the electron transport [36, 37]. Although not seen in many cases, the existence of fibrils is believed to be an interesting, potentially useful but perhaps optional component to high performing devices. At any rate, their presence and effects on morphology and performance should be examined in depth.

#### 1.1.3.4 Beyond P3HT: PCBM

P3HT:PCBM has been the workhorse, go-to system for organic photovoltaics with literally thousands of studies in the last 5 years [22], however its performance has been limited by its absorption spectrum to only collecting light efficiently in the short wavelength optical to UV range, missing the bulk of available solar power spectrum closer to infrared. To remedy this, there has been considerable effort to develop high performance low band gap materials. The idea is that just by virtue of absorbing a more power-rich spectrum of sunlight, these materials would increase potential performance dramatically.

Unfortunately, what this effort has revealed is a huge variability of essentially all the morphological factors of high performance devices. Volume fraction of components, crystallinity, optimal active layer thickness, and thermal stability all are very different than the rules of thumb developed with P3HT PCBM devices. On the positive side, much higher performance materials have been developed. Until recently the highest performing material was PTB7 mixed with PC<sub>71</sub>BM [12, 38, 39], although recent tandem cells [20, 40] have shown efficiencies greater than 10%.

It is clear that although the progress over the last few years on these devices has been very promising, the lack of tools suitable for determination of the structure of the materials has

limited understanding of their workings. Much of the success has been optimizing processes by trial and error, and in the design of novel polymers [41] not from a principled physics-driven paradigm.

#### 1.1.4 MEASURING ORGANIC DEVICES

Since their development, many techniques have been utilized to shed light on the properties of organic electronics. Traditional electronic performance measures including sensitive current voltage probes, optical absorption, and dynamic measurements able to determine lifetimes of transient energy levels and conduction properties [42] have been used to study the electronic properties of organic devices. Morphological techniques have included surface topography [43-45], and nuclear magnetic resonance [46], and neutron [47], electron [48] and X-ray imaging and scattering [34, 49]. Unfortunately fundamental problems have necessitated the development of a new suite of techniques, developed largely in the last few years, in large part specifically to measure properties of these important devices.

#### 1.2 DIFFICULTIES OF MEASURING MORPHOLOGIES

The main problems encountered with determining the morphological properties of organic electronic devices come from their largely low atomic weight constituents, their working size scales, and their plasticity. These properties combine in often unfortunate ways. Probes that have the necessary materials contrast often lack the ability to measure the size scales necessary, while those able to measure both will often damage the very film they measure [50].

### 1.2.1 MATERIAL CONTRAST

Being composed of primarily low atomic weight materials with very similar electron and neutron densities, organic materials have poor contrast with many conventional probes. Meanwhile the size scale of thin film devices is far too thin to give adequate absorption or scattering lengths for X-rays and neutrons, further compounding the problem. For electrons on the other hand, the size scale is too big to handle easily. 100 nm thick films are often too thick to measure easily with Transmission Electron Microscopy (TEM). Although cross sections can be used successfully [51], surface sensitive probes lack the ability to see what lies beyond the exposed surface.

Bilayer devices are conceptually much simpler, having planar symmetry, so that devices based on this geometry like OFETs should fare better. Unfortunately the interface of interest is the polymer-polymer interface which is formed when the device is created. Subsequent processing of the completed bilayer is often necessary to improve performance, potentially changing the once exposed interface dramatically. Any attempt to probe this altered interface by revealing it to a surface sensitive probe will result in possible changes to the interfacial structure. On the other hand, transmission type measurements will have only the interfacial region as signal, while all of the other interfaces and bulk layers that the probe beam will have to pass through to get to the interface of interest will act as background.

Several newer techniques, all alterations of more established techniques have been developed to overcome the short comings, and provide important tools for morphological characterization.

### 1.2.2 NEUTRON SCATTERING AND REFLECTIVITY

Neutron scattering and reflectivity often suffer from very similar scattering length densities between components, although in several notable cases, such as when fullerene derivatives are used in polymer solar cells, contrast can be sufficient to measure thin films. In general however, in order to get contrast between materials, one of the materials must be altered to have a much lower scattering length. Because cold neutrons interact heavily with deuterium, particularly when compared to Hydrogen, by changing a few of the hydrogens in a sample to a deuterium, the scattering length density is effectively changed a huge amount [52]. Components and full devices that mirror real devices can be made with these altered materials. Although their structure is different, and so the molecular conformations may be slightly changed [53], the hydrogens are rarely involved with electrical and structural properties. Thus deuteration is an effective way to change the contrast between materials with minimal alteration and gain contrast. Unfortunately, in order to tune the contrast to different values, whole new batches of materials must be made, making the process difficult and expensive.

Even undeuterated devices have recently been used in neutron scattering experiments, often by stacking or using especially thick devices [47], or coming into the thin film from a glancing angle [54]. All of these efforts effectively increase the flight path of neutrons in the material of interest, and so increase the chances of interacting, increasing the signal to noise.

### 1.2.3 ENERGY FILTERED ELECTRON MICROSCOPY

While TEM and SEM have been used to reveal the nanoscale of organic electronics, [51] until the use of electronic filtering, the identification of phases was difficult [55] requiring staining [56], and determination of structure was tenuous [47]. Energy Filtering can use the

same mechanism as will be described with resonant soft X-rays below in depth. Molecular structure, even near absorption edges of core electrons specifically the carbon core electron, can cause resonances dependent on the local molecular environment. This fine structure [36] can be used to provide contrast between materials, and allow chemical identification. Using energy filtered Electron Microscopy where the energy of the electrons measured can be finely controlled, only those electrons which have lost a certain energy level can be measured. For instance, if an electron has lost precisely 284.5 eV of kinetic energy, it can likely be attributed to the PCBM, whereas a loss of 285.2 can likely be attributed to P3HT. In this way, with enough incident photons, a material specific TEM image can be constructed. [36]

Downsides, as hinted at in the description above, include damage to the device being measured. The number of electrons incident on the device is much larger than those making the image meaning the total radiation dose is many times the number making the image. Other energy loss differences can be used, besides the carbon 1S, including the plasmonic resonances from 15-30 eV [37]. These loss mechanisms are much more common, and so the incident flux needed to create an image at these energies is lower. Unfortunately these energy ranges are harder to quantify to a single material, as the absorption spectra overlap significantly.

Despite this, energy filtered transmission electron imaging, including even energy filtered three dimensional reconstruction done by tomography has been recently accomplished [48].

#### 1.2.4 SOFT X-RAYS

X-rays have long been used to determine the molecular and nanostructure of polymer systems [57]. typically using electron density differences, hard (high-energy) X-ray scattering

has been used to determine crystal properties of polymers, including thin film devices. In these cases, the electron contrast is actually very high. That is, at the molecular level, the electron density difference between the backbone and side chains is large [58]. In part this is also why polymers are poor conductors. Metals have high electron densities essentially everywhere, creating an extended band structure whereas conjugation in organic materials is typically linear or in the case of graphene, planar at best, and in polymers not delocalized beyond the conjugation length [59].

Unfortunately when coarse graining away from the local molecular structure, and looking for larger scale properties, on the level of the exciton diffusion length in OPVs, or the mean path of carriers in OTFTs, these materials have very uniform averaged electron densities. With the development of synchrotron facilities able to produce different X-ray energies, the ability to extend sensitivity beyond simple electron density differences and use resonances near absorption edges to dramatically change the effective contrast between these organic materials.

## 1.3 SOFT X-RAYS

### 1.3.1 RESONANCE

As discussed above for Energy Filtered TEM, resonances in absorption of materials can reveal molecular chemical properties [60]. As shown in Figure 1.3-1, different bonding configurations change the local environment of a carbon atom, which changes the spectrum of energies available for that electron to move to. The Near Edge X-ray Absorption Fine Structure

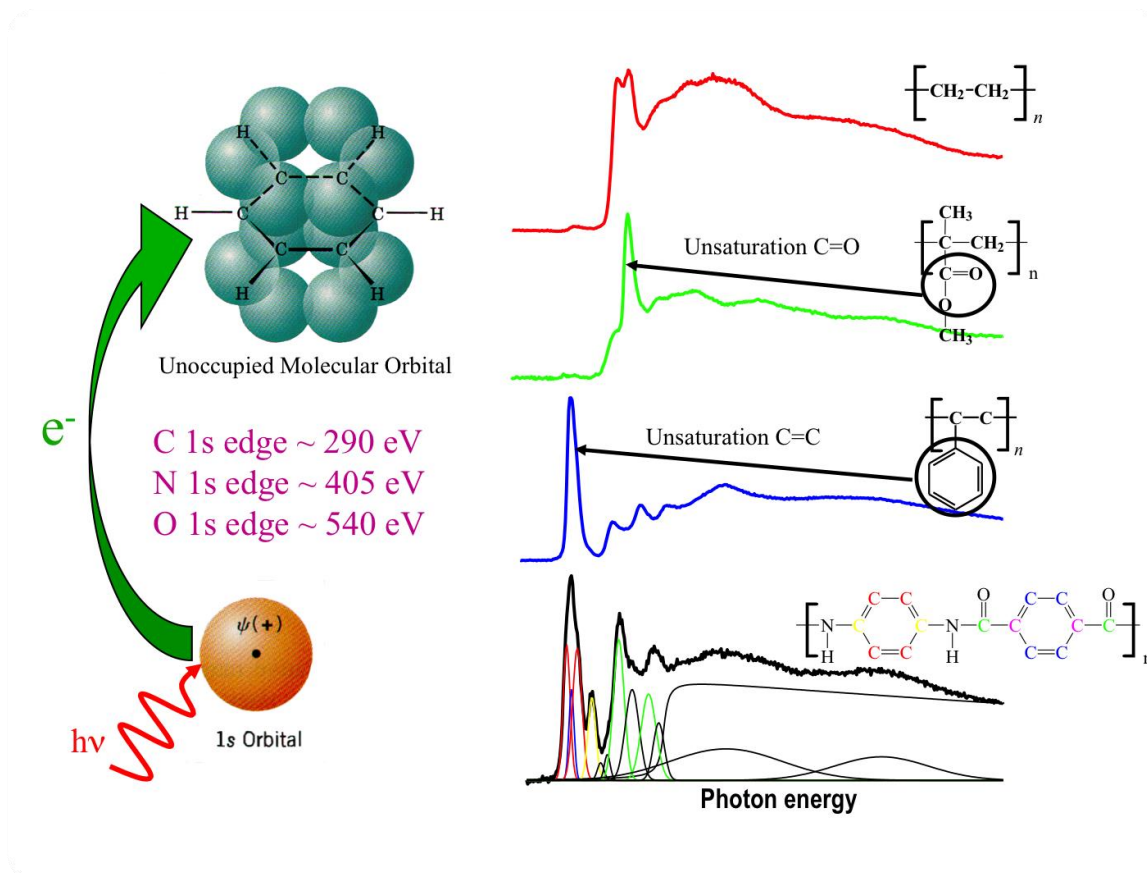


**Figure 1-5 Depiction of the Resonance Effect**

Schematic of the photo excitation of an electron from the 1S orbital into a molecular orbital. Changes in the molecular orbital affect the energy landscape of this excitation, and reveal molecular resonances, which can be used to identify materials. (Figure created by A.P. Smith)

(NEXAFS) can use this sensitivity to provide a unique fingerprint of different chemicals. Beyond this, by the Kramers-Kronig relations [61],  $\delta$ , or real part of the index of refraction can be calculated, which also changes accordingly in this region. This means the full complex index of refraction of materials at absorption edges can fingerprint that material, and can also provide contrast enhancement without actually absorbing photons (which can lead to beam damage).

### 1.3.2 STXM

The first nanoscale imaging done at the carbon 1S X-ray absorption edge was with Scanning Transmission X-ray Microscopy (STXM), developed at second generation synchrotrons [62-65]. While limited in resolution to roughly 30 nm, depending on the quality of zone plate optics which are used to focus the beam onto the sample, which is then rastered to make a 2D transmission image [66-68], this was the first chemically sensitive nanoprobe capable of imaging and chemically mapping an organic thin film. While still often used in for organic device measurement, the optics-limited size sensitivity makes the resolution just a bit too high for the majority of OPV samples, and the transmission geometry means sensitivity to the interface in OTFT samples is still low. The next generation of imaging techniques such as X-ray Ptychography [69] promise wavelength limited reconstructions

### 1.3.3 REFLECTIVITY

For bilayer devices, reflectivity at these resonant energies has been developed to reveal the out of plane structure, particularly the thickness of different components, and the roughness

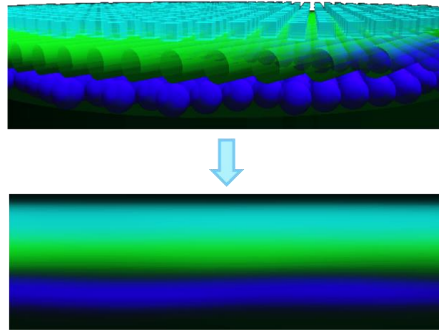


**Figure 1-6 Illustration of Insensitivity to In-Plane Information**

While measuring the out of plane structure very accurately, the in-plane information cannot be easily recovered from reflectivity.

of each interface, including internal interfaces [70]. Utilizing both the absorptive differences of materials, but also the refractive differences [29], it has been used in the last decade to reveal the structure of many thin film devices, including the interfaces of interest in OTFTs [71-73]. Unfortunately, the results obtained from reflectivity curves alone do not include easily accessible information of the in-plane structure of the roughness. So while we may be able to find out that there is a one nanometer wide interface for instance, we don't know if that one nanometer region consists of molecular interpenetration or larger scale undulations. What scale the roughness is at will potentially be critical in determining local slope variations, defects, nanoscale sharpness of the interface and other features which are presumably critical to performance.

### 1.3.4 SCATTERING

Reflectivity moving from a real space representation of the sample to a reciprocal space representation. We are replacing local knowledge of the sample with statistical ensemble average of local data. We don't know the thickness of the device at any specific region, but a probability of what the thickness is everywhere. This ensemble information available in Fourier space is also the strength of Resonant Soft X-ray Scattering (RSoXS).

Scattering, unlike imaging, uses a macroscopic (~100  $\mu\text{m}$  diameter) collimated beam incident on the sample, collecting only the far field scattered light, usually blocking the intense direct beam. The physics of scattering is discussed rigorously in Chapter 3. The benefits of scattering stem from the fact that focusing the probe beam down to a point on the sample is not necessary, rather wavelength (~4.5 nm at the carbon 1s edge) limited information is gathered from a comparatively larger region of the sample (often ~100 microns – see Chapter 2). This adds not only the statistical benefit, but also lowers the local flux density, and so lowers the chance of radiation damage.

## 1.4 SOFT X-RAY SCATTERING

The development of Soft X-ray scattering requires advanced X-ray sources such as third generation synchrotrons, and advanced in-vacuum imaging capabilities. The main distinction between hard and soft X-rays, is soft X-rays are absorbed in air. Unlike hard X-ray experiments, both the sample and detector, as well as the full path of the beam needs to be in high vacuum for soft X-ray scattering experiments.

Initial resonant scattering efforts on organic systems were on nanoparticles [74] and block copolymers [75] at the Advanced Light Source. These studies revealed the ability of

RSoXS to have both higher contrast between materials, and variable contrast with slight changes of energy. The first uses of RSoXS to reveal the internal structure of an OPV device [76, 77] was accomplished with a one dimensional scanning measurement. This form of scattering collection takes a long time to collect, and allows for a large amount of x-ray exposure potentially causing damage to the devices being measured.

The development of two dimensional in vacuum detectors allowed efficient collection of Soft X-rays [78]. Finally, the development of a scattering chamber on an undulator beamline, described in great detail in the previously published [79] Chapter 2, allowed efficient and accurate collection of Soft X-ray Scattering. Using this new tool, our group and others have used Soft X-rays to probe both OPVs and OFETS [1, 12, 80-89].

## 1.5 THESIS OUTLINE

This thesis presents several pieces of work using scattering from soft X-rays to further elucidate structure of both OPVs and OTFTs. First Chapter 2 presents the development of the scattering facility described briefly above. Next a review of analysis techniques applicable for OPV systems and for RSoXS in general is presented in Chapter 3. In Chapter 4, I present some theory work, developing a model to simulate anisotropic scattering often seen in OPV systems. Finally Chapter 5 shows the development and analysis of a new kind of scattering geometry, collecting RSoXS at a grazing angle. This geometry adds the extra benefit of giving depth and material specific sensitivity, capable of determining the internal structure of interfaces, critical to OTFTs. Chapter 6 provides a summary of the work, and discusses future outlook in this field.

## *Chapter 2*

### **SOFT X-RAY SCATTERING FACILITY AT THE ADVANCED LIGHT SOURCE WITH REAL-TIME DATA PROCESSING AND ANALYSIS**

Before I was able to develop techniques and utilize the power of soft X-rays, I first required a facility capable of produce high quality soft X-rays, in a well-defined, normalized and monitored beam. The following chapter is a published article from Review of Scientific Instruments, published April 12, 2012, describing this beamline, the first of its kind in the world. Coauthors of this paper include Anthony Young, Brian Collins, Hongping Yan, Jamie Nasiatka, Howard Padmore, Harald Ade, Alexander Hexemer and Cheng Wang. All of the work was accomplished in collaboration with the staff of the Advanced Light Source. I collected all the data presented in the paper, and conducted all the analysis save the grazing incidence Block Copolymer sample, provided by Cheng Wang. Brian Collins and Hongping Yan helped with data collection and analysis. Jamie Nasiatka designed and created the higher order suppressor. He along with Cheng Wang and Anthony Young built and conducted initial measurements at 11.0.1.2. Harald Ade, Cheng Wang, Alexander Hexemer, and Howard Padmore all had fundamental formative input on the beamline and in general on the field of Soft X-ray Scattering.

## Soft X-ray Scattering Facility at the Advanced Light Source with Real-time Data Processing and Analysis

E. Gann<sup>1</sup>, A.T. Young<sup>2</sup>, B.A. Collins<sup>1</sup>, H. Yan<sup>1,2</sup>, J. Nasiatka<sup>2</sup>, H.A. Padmore<sup>2</sup>, H. Ade<sup>1</sup>, A. Hexemer<sup>2</sup>, C. Wang<sup>2\*</sup>

<sup>1</sup> Department of Physics, North Carolina State University, Raleigh, NC 27695-8202

<sup>2</sup> Advanced Light Source, Lawrence Berkeley National Laboratory, Berkeley, CA 94720

\* To whom correspondence should be addressed: cwang2@lbl.gov

### 2.1 ABSTRACT

We present the development and characterization of a dedicated resonant soft X-ray scattering facility. Capable of operation over a wide energy range, the beamline and endstation are primarily used for scattering from soft matter systems around the carbon K-edge (~285 eV). We describe the specialized design of the instrument and characteristics of the beamline. Operational characteristics of immediate interest to users such as polarization control, degree of higher harmonic spectral contamination and detector noise are delineated. Of special interest is the development of a higher harmonic rejection system that improves the spectral purity of the X-ray beam. Special software and a user-friendly interface have been implemented to allow real-time data processing and preliminary data analysis simultaneous with data acquisition.

### 2.2 MOTIVATION AND BACKGROUND

Soft matter systems, including many high performance materials in novel devices, often consist of multiple components and are naturally or synthetically nanostructured for optimal properties and performance. To fully understand their structure-property and structure-performance relationships, quantitative compositional analysis and morphological characterization at the sub-100 nm or even sub-10 nm length scale is required. This need is generally addressed by various microscopy or scattering methods. The particular contrast

mechanism used defines the utility of the particular microscopy [90-94] or scattering method [95-100] for a given type of sample. Those capable of achieving high q-range and q-resolution include conventional small angle X-ray scattering (SAXS) and small angle neutron scattering (SANS). These are powerful characterization methods that are widely utilized to assess the morphology, size or shape of a wide range of material classes investigated in numerous disciplines [95-99, 101]. The intensity profiles of SAXS and SANS are the modulus squared Fourier transforms of the real space electron or scattering length density of the sample respectively, and so measure the statistical average of the sample morphology over the illuminated volume. A number of sophisticated analysis methods have been developed to also determine, for example, various correlation functions (i.e. height, density, and pair correlations of surface and bulk features), purity of domains, and the radius of gyration of polymers [95-97]. For soft, organic matter, scattering contrast using conventional SAXS at higher energies relies on electron density differences [95-97] unless energies near an absorption edge are used to exploit “anomalous” enhancements [102, 103]. Resonant soft X-ray scattering (R-SoXS) methods achieve contrast between functional moieties and can have orders of magnitude more scattering intensity than SAXS, facilitating investigations of very thin organic films in transmission [74-76, 104].

The physical basis of the contrast mechanism and the general advantages of R-SoXS have been described extensively before. Basically, the effects of the interaction of X-rays with matter is encoded in the complex index of refraction

$$n(E) = 1 - \delta(E) - i\beta(E). \quad (1)$$

These two energy dependent terms of the index of refraction are related to the complex scattering factor

$$f = f_1 + if_2 (= f_o + \Delta f' + i\Delta f'' \text{ in anomalous SAXS terminology}) \quad (2)$$

in the forward scattering or long wavelength limit through

$$\delta + i\beta = \alpha\lambda^2(f_1 + if_2), \quad (3)$$

where  $\alpha = n_a r_e / 2\pi$ , with  $n_a$  being the number density of atoms, and  $r_e$  being the classical radius of the electron. Consequently, bond-specific contrast can be achieved in a manner similar to Near Edge X-ray Absorption Fine Structure Spectroscopy (NEXAFS) microscopy, because  $\delta$  and  $\beta$  change rapidly as a function of photon energy near absorption edges and the quantity  $\Delta\delta^2 + \Delta\beta^2$  determines the materials contrast and scattering strength. The reader is referred to the literature for more details [75, 76, 78, 104-108]. More recently, it has been pointed out and shown that R-SoXS furthermore has unique contrast to bond orientation if polarization control of the incident photons is possible. [1, 109]

Although soft X-ray scattering systems and facilities with detection systems based on 2D detectors such as CCDs have been previously developed, these are mostly optimized for magnetic scattering [110] and/or coherent imaging [111-113]. The initial R-SoXS developments for soft matter and the first applications occurred with a point detector at a bending magnet beamline at the Advanced Light Source (ALS). This facility [114] was optimized for reflectivity and thus provides only slow R-SoXS data acquisition rates for any geometry other than  $\theta$ - $2\theta$  scans, which can lead to radiation damage [78]. In order to greatly improve data rates and experimental capabilities to study radiation sensitive soft matter, we developed a new endstation at the ALS Beamline 11.0.1.2 capable of scattering X-rays with

energies from 165 eV to 1.8 keV to probe size scales from 0.5 nm to 5  $\mu\text{m}$ . We describe the hardware components of the beamline and endstation. The in-vacuum 2D detector system [78] is capable of the equivalent small angle scattering experiments performed with conventional SAXS [57] and SANS [47, 115], but with unique tunable chemical sensitivity and bond orientation contrast afforded by the resonant interactions of soft X-rays.

There are numerous experimental challenges when operating near the carbon K absorption edge for which we present methods of characterization and mitigation. These include characterizing and controlling the degree of polarization of the X-ray beam and higher harmonic spectral contamination, as well as correcting for sources of detector noise and characterizing the detector spectral response. Additionally, we present a live scattering analysis system that performs data correction and reduction allowing for immediate determination of data quality and efficient use of experimental time.

## 2.3 BEAMLINE DESCRIPTION

The dedicated system described here has been retrofitted as a branch line to an existing ALS beamline that already supports a third generation Photoelectron Emission Microscope (PEEM-3) [116]. Initial developments of this scattering chamber and scattering efforts have been described by C. Wang et al [78].

### 2.3.1 HARDWARE OF ADVANCED LIGHT SOURCE BEAMLINE 11.0.1.2

#### 2.3.1.1 X-Ray Source and Upstream Optics

Beamline 11.0.1.2 is schematically depicted in Figure 2.1. It has as its X-ray source an Elliptically Polarizing Undulator (EPU). This 5 cm period EPU directly produces high brightness X-ray photons from 165 eV to 1.8 keV, with variable linear or elliptical polarization

[117, 118]. In this type of undulator, four rows of permanent magnets are placed along the axis of the electron beam. Two of the rows are placed above the plane of the storage ring and to either side of the electron beam, and two below, again with one on either side of the beam. By changing the distance (the “vertical gap”) between the upper pair and the lower pair, and the longitudinal position of the rows (the “row phase”) relative to each other, control of both the energy and polarization of the X-rays is obtained. Linear polarizations with E-fields oriented from  $0^\circ$  to  $90^\circ$  (measured relative to horizontal) are available at energies above 160 eV. Using the fundamental output from the undulator, pure circularly polarized X-rays can be produced from 130 eV-600 eV. For higher energies, the 3<sup>rd</sup> and 5<sup>th</sup> undulator harmonics must be used. However, using the harmonics generates elliptical rather than pure circular polarization. High flux and brightness can be retained in the 3<sup>rd</sup> and 5<sup>th</sup> harmonics with degrees of circular polarization of 0.8 to 0.9.

From this source, using a horizontally deflecting, vertically focusing sagittal cylindrical mirror, the X-rays are directed and focused into a vertically dispersing, variable line-spaced grating monochromator equipped with an horizontal entrance slit. The monochromator contains a grating that has three different line densities on a single substrate, optimized for the energy ranges 165-600 eV (250 line pairs per millimeter, lpm), 330-1300 eV (500 lpm) and 660-2000 eV (1000 lpm). A feature of the beamline is the inclusion of an adjustable bendable elliptical mirror just upstream of the monochromator exit slits. This allows for the adjustment of the horizontal beam size and position downstream of the monochromator. When optimized for the scattering chamber, it produces a minimum horizontal sample spot size of 300  $\mu\text{m}$  full width at half maximum. The exit slits of the monochromator are formed by four independently

controlled precision knife-edges, which allow for control of the spectral resolution (vertical aperture) and intensity (horizontal aperture.) After passing through the exit slits, the X-rays are deflected by a vertical focusing mirror, producing a vertical image at the center of the scattering chamber. This mirror has a magnification of 3, yielding typical vertical spot size (FWHM) of 100  $\mu\text{m}$ .

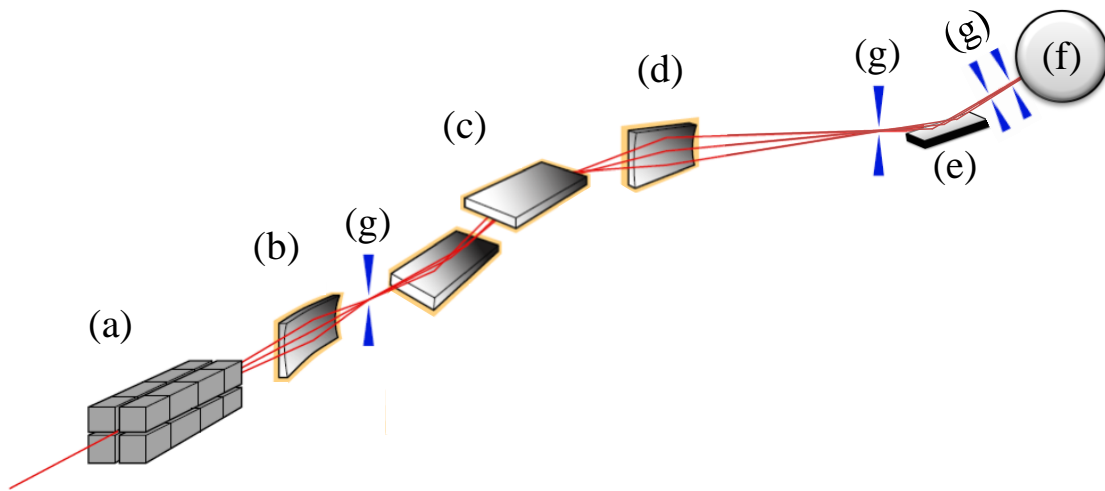


**Figure 2-1 Beamline branch 11.0.1.2 conceptual schematic**

(not to scale), showing placement of major beamline components: (a) elliptically polarizing undulator, (b) horizontal deflection vertical focus cylinder switchyard mirror, (c) vertical deflection spherical mirror and variable line spacing grating monochromator, (d) horizontal deflection bendable tangential cylinder focusing mirror, (e) 6 degree deflection mirror into the 11.0.1.2 branch line, and (f) sample chamber. (g) Blue triangles indicate locations beam defining and scatter slits except the final set which is inside the sample chamber. Each set of slits consists of one horizontal and one vertical slit.

### 2.3.1.2 Higher Order Suppressor

Before reaching the scattering chamber, the beam can optionally be passed through a four-bounce mirror assembly (Figure 2.2) that can filter out higher harmonics produced by the undulator and passed by the monochromator. The four-bounce design was chosen because of its superior order-suppression (2<sup>nd</sup> order  $>10^{-3}$ , and 3<sup>rd</sup> order  $>10^{-5}$  suppression over the 100 – 600 eV range), a constant exit path with an adjustable incidence angle, and a simple mechanical design. Pairs of parallel mirrors are placed in standard optical mounts that have been modified to allow each optic to be supported by springs attached to the back surface but held in position by clips on the front. These mounts are arranged to form a double periscope so that the exiting beam is co-linear with the entering beam. The periscope assemblies are positioned by sets of pivot/flexure bearings within a housing that directly connects to the vacuum chamber. A linear feedthrough presses on the periscopes adjusting the rotation angles in tandem. A pico-motor is mounted on the final optic for small adjustments and beam steering. There is no linear motion

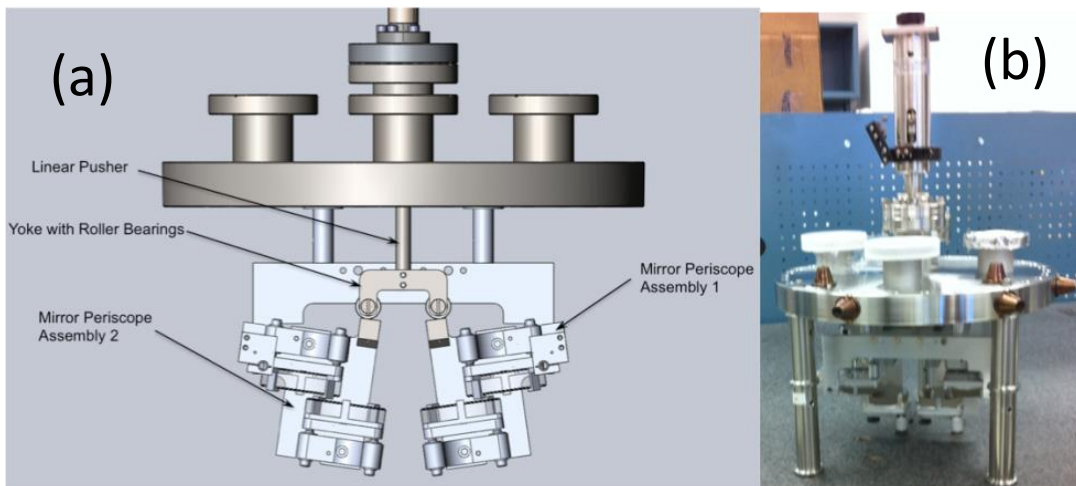


**Figure 2-2 Higher harmonic rejection mirror assembly**  
(a) Schematic and (b) photograph.

in the assembly, which means the beam will ‘walk’ across the mirrors as the angles are changed. This configuration minimizes both the amount of in-vacuum motion required as well as the number of components that could be misaligned after installation. The optical elements in this design are standard 2" diameter uncoated mirror blanks coated with 20 nm of Ni for optimized performance in the 200-600 eV energy range. The overall size of the optics are determined by the length of the beam as it intersects the optical surface combined with the distance the beam will walk across the length of the optic as the reflection angle is changed between 4° and 8°. The optics are also capable of being moved out of the beam-path, allowing for unfiltered light to freely pass through a 3.5 mm gap to the endstation when higher energies are needed or higher harmonics are not detrimental. This compact design requires only one motorized axis and produces a constant beam-path at any incident angle. A patent on this order suppressor, designed at the Advanced Light Source, is now pending.

### 2.3.1.3 Beam Definition and Monitoring

Three sets of horizontal/vertical slits are used to define the beam on the sample and minimize parasitic scattering. All are configured to independently adjust the positions of four beam-defining knife edges (left/right/top/bottom). The first set, manually actuated, is located approximately 1.5 m upstream of the sample chamber and allows for fine definition of the beam. The second set (JJ X-ray) is motorized and located just outside the chamber 0.6 m upstream of the sample. It is able to remove most of the remaining parasitic scatter produced by the first set of slits. The final set of slits is located inside the scattering chamber, about 0.2 m (adjustable) upstream of the sample. In-vacuum picomotors (New Focus) control the

position of these slits to produce a clean beam profile, allowing for measurements down to  $2\theta = 0.04^\circ$ , corresponding to a feature size of  $\sim 4 \mu\text{m}$  with energies near the carbon K edge, matching the coherence size of the X-ray beam.

Beamline 11.0.1.2 includes the capability in a number of locations to measure the photon flux for diagnostic and experimental needs. Of experimental interest, located after the six degree deflection mirror, an assembly with a gold mesh can be lowered into the beam and connected to a picoammeter to allow measurement of photoelectric current. However, because this filter assembly is upstream of the higher harmonic rejection mirror assembly, the spectrum of X-rays measured here is not suitable for normalization of scattering intensities when higher harmonic contributions are significant, as is the case during operation at energies that correspond to the carbon dip (see section III.C). In this case, a second gold mesh, directly downstream from the higher harmonic suppression mirrors but before the first set of slits can be used as an incident flux measurement.

A pneumatic photon shutter just upstream of the sample chamber allows the X-ray beam into the sample chamber, and is synchronized to the 2D detector exposure. This shutter allows the CCD detector to accurately and reproducibly collect 2D scattering intensities down to 0.1 s exposures.

#### 2.3.1.4 Sample Chamber

The high vacuum sample/detector chamber shown in Figure 2.3 houses a sample stage and the detector, which are mounted on independent goniometers in a 2-circle diffractometer geometry. The sample stage is able to move in three spatial and one rotational direction, allowing multiple transmission or reflectivity/ grazing samples to be loaded at the same time.

The sample translation stages have 50 mm total of travel, allowing a total accessible area in one sample load of  $\sim 2500 \text{ mm}^2$ .

The sample chamber can be opened in roughly 10 minutes by warming up the camera to room temperature, closing all the valves and shutters and subsequent venting the chamber with dry nitrogen. Samples can be accessed through a small door or a larger door, depending on need for access. Pumping down the chamber to  $10^{-6}$  torr and cooling the detector to its normal working temperature of  $-45^\circ\text{C}$  takes  $\sim 20$  minutes, resulting in a total sample exchange time of approximately 30 minutes.

The sample stage is held by a kinematic mount with three points of contact, which is electrically isolated from the goniometer, allowing for the measurement of photocurrents generated during X-ray exposure. This setup can be used to measure total electron yield near edge X-ray absorption fine structure (TEY-NEXAFS) spectra from the sample. Two photodiodes (5 mm x 5 mm GaAs photodiode from Hamamatsu and 1 mm x 3 mm Si photodiode from Advanced Photonix) are mounted on the  $2\theta$  detector arm. The first is designed to be in the direct beam when  $2\theta = 0^\circ$  and is used for  $\theta$ - $2\theta$  reflectivity scans and NEXAFS spectroscopy in a transmission geometry. During these types of measurements, the 2D detector is rotated away from the optical axis and thus protected from the direct and reflected beams. The second photodiode is mounted on the beamstop protecting the 2D detector from the direct X-ray beam. This allows simultaneous flux monitoring and absorption measurements while 2D scattering data are being collected.

Cross calibration of the first diode has been measured by comparison within the narrow overlap of flux at which both the CCD detector and photodiode are usable (see results of

spectroscopic response of 2D detector, below), and determined to be  $9.8 \times 10^9$  photon/nA at 283 eV.

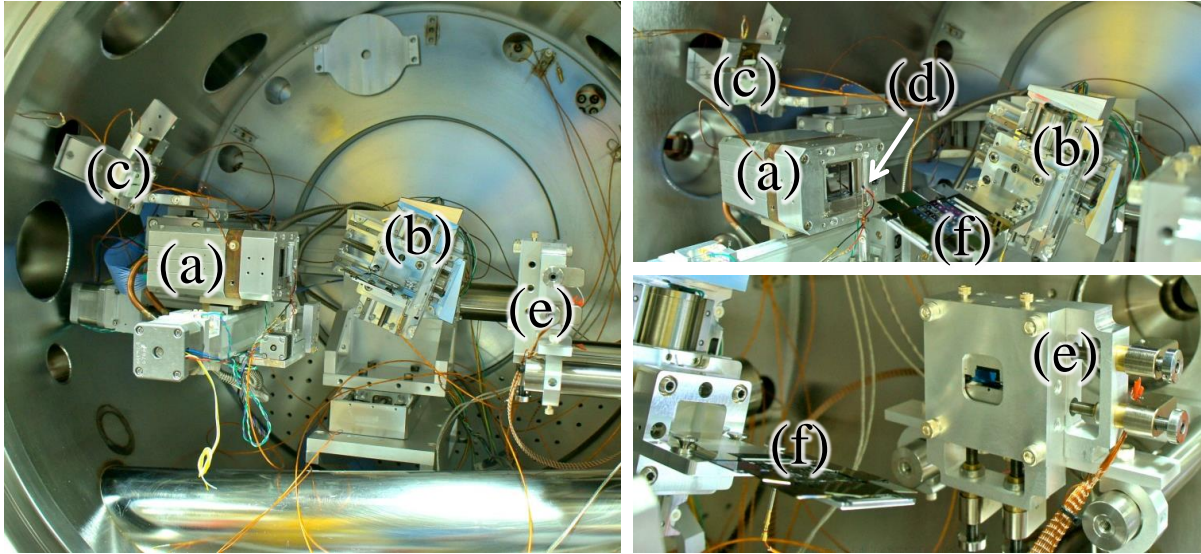


**Figure 2-3 Views inside of the soft X-ray scattering chamber**

Located at ALS BL11.0.1.2. (a) 2D scatter detector, (b) sample goniometer, (c) photodiode, (d) beamstop photodiode, (e) exit slits and (f) sample stage

### 2.3.1.5 Soft X-ray CCD Detector

The in-vacuum, back-illuminated CCD soft X-ray detector (Princeton Instruments PI-MTE) is thermoelectrically cooled to  $\sim 45^\circ$  C. Heat produced by the thermoelectric cooler is removed by circulating chilled liquid ethanol through the copper heatsink to which the camera is mounted. The heatsink is connected through flexible hoses via a vacuum feedthrough to a chiller outside the chamber. The CCD consists of a 2048 x 2048 array of  $13.5 \mu\text{m} \times 13.5 \mu\text{m}$  pixels. The detector is installed on a 2D stage with 80 mm x 80 mm of movement, which is mounted on the  $2\theta$  arm of a goniometer rotating in the vertical plane. This allows the sample-

detector distance to be adjusted from 80 mm to 160 mm while the allowing the detector collect to scatter from  $-25^\circ$  to  $+160^\circ$  from the incident X-ray beam. By acquiring exposures at varying detector positions and angles, a large q-range can be covered efficiently. At energies near the carbon edge, this procedure allows collection of scattering data that corresponds to feature sizes from less than 3 nm at  $2\theta = 110^\circ$  to greater than 3  $\mu\text{m}$  at  $2\theta = 0.04^\circ$ . Utilizing the extreme energies available on the beamline (165 eV – 2000 eV) the accessible feature size spans four orders of magnitude from 0.5 nm to 5  $\mu\text{m}$ .

#### 2.3.1.6 Calibration Samples

Geometrical calibration samples are a necessary component of any scattering facility, as the incredible variety of experimental setups available entail that accurate measurement of the sample and detector geometry is often very tricky and can vary with each individual experiment. Although monitoring motor positions can give a very good idea of the geometry (discussed in Section III.F), when possible, calibration scattering sets are taken with each set of data to ensure the correct scattering angles are collected. Calibration samples which cover the energy and q range of this scattering facility are more complicated in comparison to higher energy beamlines. Samples with well-defined scattering peaks in the 10-1000nm range are less common than the crystalline systems available in the .1-10nm region. At higher photon energies or for very large scattering angles, standard hard X-ray calibration samples such as silver behenate [119, 120], which has well ordered 5.8 nm lamellae, can be used. However, for typical soft X-ray photon energies and the size scales probed with them, this 5.8nm ring is not useful. For this reason, we have developed a set of samples suitable for calibration with the use

with soft X-rays to cover the  $q$  and energy range available at this facility. Our primary calibration is a manufactured linear grating with 200nm spacing (described in Section III.C), although it is of little use in beam centering because it is a linear grating and so only usable in one dimension. Thus one or more of a set of secondary calibration samples each on a 100nm silicon nitride film supported on a 1x1mm silicon window for transmission geometry is typically loaded directly along with each sample load. First, a silver behenate powder as mentioned above is used for very large angle scattering or higher energies where features near from 1-10nm are probed. Second, 300 $\pm$ 1 nm diameter poly(styrene) nanospheres with well characterized scattering maxima, drop cast and dried from an aqueous solution are used for very low angles (large features) and low energy scattering (these two calibration sample scattering examples are shown in Figure 2.9). Finally, for general scattering of 10-100nm features, where neither of these calibrants are ideal, a poly(isoprene-*b*-styrene-*b*-2-vinyl pyridine) (PI-*b*-PS-*b*-P2VP) triblock copolymer  $\sim$ 1 $\mu$ m thick film [56] that has a well characterized 39.1 nm hexagonal cylindrical lattice with high scattering contrast at 280 eV is often a convenient calibrant (discussed in a thin film grazing geometry in Section IV.C).

### 2.3.2 CONTROL ELECTRONICS AND SOFTWARE FOR INSTRUMENT CONTROL AND REAL-TIME ANALYSIS

Standard ALS beamline control software orchestrates control of all motors and acquisition at the endstation. X-ray energy, polarization, mirror and monochromator settings, as well as the locations of the sample, detector, filters and slits can all be electronically controlled and queued up for extensive automated 2D scattering data acquisition. This software controls over 35 motors, inputs 9 analog channels and video from inside the sample chamber

to help with placing the X-ray beam where necessary, and controls the exposure of X-rays in both photodiode and CCD exposures. A separate program based on the software package NIKA [121] (Described in section III. D ) reads CCD scattering data as it is written, and is able to automatically reduce the 2D scattering datasets into  $I(q)$  plots. The orchestrating nature of this control system, requiring simultaneous changes of both the undulator and the monochromator to change photon energy for instance, makes typical one dimensional scans such as scattering versus energy and absorption spectra somewhat more time consuming than at a simpler beamline, however such delays are appropriate when reading out this CCD, which has a readout time of  $\sim 5$  seconds at full resolution or  $\sim 2$  seconds in a  $2 \times 2$  binned mode.

The queuing capability of the beamline control software allows automation of the data acquisition of many samples in one large scan. First, all the sample locations are found and recorded. Next, values of the desired independent variable for each sample (e.g. energies, polarizations, etc.) are determined. The user creates a scan file with these variables, which the program can use to automate the collection of scattering patterns at each beamline configuration listed in the scan file, adjusting the beamline parameters between exposures as necessary. CCD exposure time can additionally be varied to insure proper levels of exposure for different scattering intensities. In many cases, energies are difficult to pick ahead of time, in which case a quick scatter scan of a sample over a range of X-ray energies can be easily collected. With 1 second exposures, the energy range covering the carbon edge can be collected in  $\sim 10$  minutes. If the automatic scatter analysis tool running, maximum contrast energies are readily found by noticing when the scatter profile is maximized, at which point a targeted scan with longer exposures at these appropriate energies can be created and executed.

## 2.4 BEAMLINE CHARACTERIZATION

In order to properly normalize 2D scattering data and achieve quantitative information, the X-ray beam and the 2D detector have to be well characterized. Properties of the X-ray beam that need to be determined include measurements of incident flux and absorption as a function of photon energy, the actual polarization of light when it reaches the sample, the beam size in the scattering chamber, the nominal energy of the photon beam, and the fractional intensity due to higher order spectral contributions. Important detector properties are fixed pattern and read noise as well as spectral response.

### 2.4.1 CHARACTERIZATION SAMPLE PREPARATION

Polystyrene nanospheres are supplied by Microspheres-Nanospheres. The supplied solutions of 300 +/- 1 nm nanospheres in 25 mg/ml, suspended in water, were drop cast on 100 nm silicon nitride windows and dried in ambient conditions for approximately 30 minutes.

The Poly(3-hexylthiophene) (P3HT) and phenyl-C61-butyric acid methyl ester (PCBM) blend (P3HT:PCBM) bulk heterojunction thin film Consisted of Regioregular (93%) P3HT supplied by Rieke, and PCBM supplied by Nano C. P3HT:PCBM blend films were spin-cast onto sodium poly(styrenesulfonate) (NaPSS)-coated glass substrates from a chlorobenzene solution with 1:0.8 weight ratio in a N<sub>2</sub> atmosphere and annealed on a hot plate at 150°C for 30 minutes. The film thickness was measured as ~250 nm via ellipsometry. The film was then floated off the substrate by dissolving the NaPSS in water. It was transferred to a 5 mm × 5 mm Aluminum frame with a 1 mm × 1 mm open window in the center, resulting a standing-alone film in the window area for transmission scattering experiments.

Other tests samples include a P3HT:P(NDI2OD-T2) blend spun cast and transferred onto a 5 mm  $\times$  5 mm Aluminum frame with a 1 mm  $\times$  1 mm open window in the center in transmission geometry used for polarization characterization<sup>24</sup> and poly(1,4-isoprene)-*block*-polystyrene-*block*-poly(2-vinylpyridine) (PI-*b*-PS-*b*-P2VP) triblock copolymer [1, 56] used in a  $\sim$ 1  $\mu$ m thick transmission sample on a silicon nitride transmission window for geometry characterization and a 40 nm thin film on a silicon wafer in grazing geometry. These samples have been described in depth previously and the reader is directed to those publications for sample details [1, 56].

#### 2.4.2 ENERGY CALIBRATION

The monochromator has a maximum resolving power ( $\lambda/\Delta\lambda$ ) of  $\sim$ 3000. Near the carbon edge, this translates into an energy width of  $\sim$ 0.1 eV. Calibration of the X-ray energy is accomplished by collecting transmission or TEY NEXAFS spectra of known polymer systems or highly ordered pyrolytic graphite (HOPG) and comparing measured resonance features to known values. Polystyrene (PS) and poly(methyl methacrylate) (PMMA) are two common polymers with known NEXAFS spectra [60]. Even though the resonant absorption peaks of these polymers are rather broad ( $\sim$ 300- 500 meV) compared to HOPG, they are suitable for easy energy calibration in transmission to within the bandwidth of the beamline. HOPG is available and is utilized in a TEY NEXAFS measurement if a more accurate energy calibration is desired [122, 123].

### 2.4.3 HIGHER ORDER SPECTRAL CONTAMINATION

The undulator produces and the monochromator passes not only X-rays with the nominal energy, but also higher harmonics of this energy. Typically these higher harmonic contributions are an appreciable, but tolerable fraction (~5-20%) of the X-ray beam. However, the flux of X-rays at energies near the carbon K edge is often significantly affected by even nanoscopic layers of carbon contamination on the X-ray optical elements of the beamline. This contamination [124, 125] reduces the reflectivity in this energy range and can result in a dramatic reduction in the flux of these first harmonic photons. This reduction is often referred to as the “carbon dip”. The pronounced reduction in available beam intensity due to the carbon dip is shown in Figure 2.4(a) and inset. Unfortunately, the affected energy range is often quite useful in probing organic systems [74, 75, 78, 104]. Since the reflectivity of the higher order X-rays are virtually unaffected by carbon contamination, the reflected beam is enriched in photons of the wrong energy. This increased fraction of higher harmonics make normalization to incident flux and quantitative analysis of experiments exploiting the unique contrasts available in this energy range difficult if not impossible. A harmonic suppressor assembly as described above (Section II.A.2) is required.

To quantify the fractional intensities of the different harmonics in the beam, we use a transmission diffraction grating with a line spacing of 300 nm and compare the intensities of the different diffraction orders at 284 eV, in the middle of the carbon dip. The diffraction grating is mounted at the sample location and the diffracted beam is recorded with the CCD detector. Figure 2.4(b) shows the resulting diffraction patterns as measured by the 2D detector. With the harmonic rejection mirrors adjusted to 5.4° incident angle, the diffracted higher order

peaks are more than two orders of magnitude lower in intensity than the first harmonic light and essentially in the background. Thus the use of the four bounce harmonic rejection assembly at or above  $5.4^\circ$  is determined to provide a sufficiently monochromatic beam at the difficult energies around the carbon absorption edge for typical experiments, although higher angles continue to improve the spectral purity. These scattering patterns shown in Figure 2.4(b) reveal that the higher harmonics are a substantial fraction of the beam when the order suppressing mirror is not utilized. Flux measurements in this energy range with a photodiode detector with no higher order rejection in place reveal that the measured intensity at 284 eV is 13% of the measured intensity at 270 eV. While the higher harmonic rejection assembly is in place, this percentage drops to 2.8% (see Figure 2.4(a)). Comparing these measurements, we can conclude that in general 10% of the photons in the beam at the time of this measurement (before carbon mitigation measures described below) are higher harmonic contributions. However, in the carbon dip, when first order light is selectively absorbed,  $\sim 80\%$  of the X-rays were higher harmonic photons. This underscores the severity of carbon contamination and the necessity of having adequate higher harmonic suppression. Although higher harmonic rejection eliminates the deleterious impact of the carbon contamination when it comes to spectral purity, the useful flux is still greatly reduced. In addition, the effects of the carbon contamination on the polarization state of the photons cannot be easily mitigated as discussed in section III.D. It is important to point out that although the 2.8% flux in the carbon edge is far from ideal, measuring it precisely as we have here shown, allows very high quality scattering data to be obtained (see section IV). Recent efforts to remove carbon contamination from several of the optics (described in Section V) and optimization of the optical configuration has significantly

decreased the carbon contamination and increased the X-ray flux. In the beamline's current state as of publication, the flux of first order X-rays has increased significantly to above 50% of the total incoming photons, which when combined with an improved optical path, results in more than an order of magnitude improvement in this critical energy range.

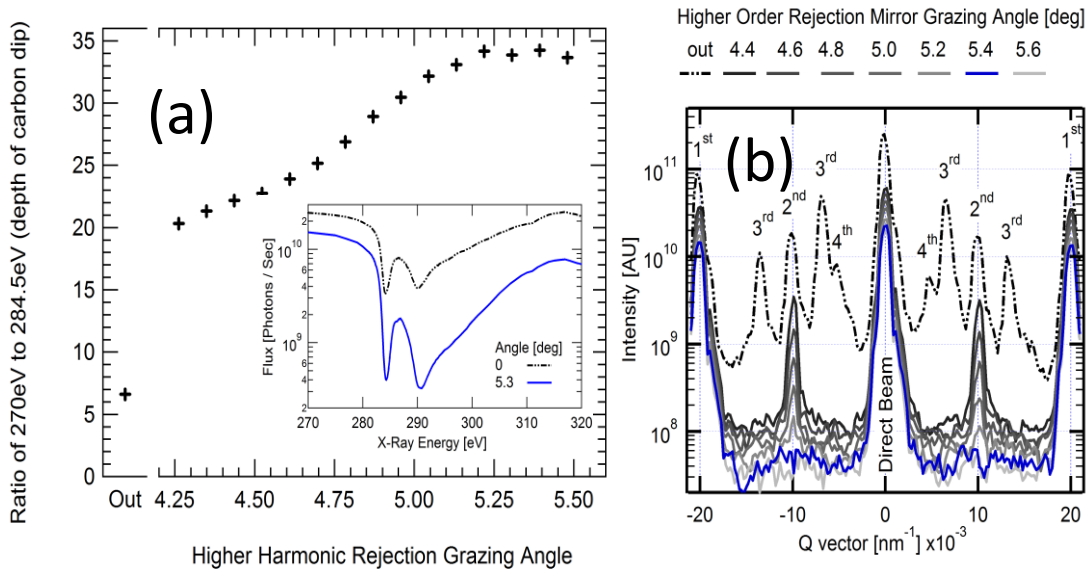


**Figure 2-4 Higher Harmonic Rejection Measurements**

(a) Depth of the carbon dip vs. higher harmonic rejection mirror incident angle. Inset are two example energy scans with and without the higher harmonic rejection mirror assembly. (b) the diffraction from a 300 nm manufactured diffraction grating at 284 eV at various settings of the higher harmonic rejection mirror. The harmonic contributions are identified.

#### 2.4.4 POLARIZATION

An elliptically polarizing undulator allows adjustment of the direction of linear polarization and the ability to switch to circular and elliptically polarized X-rays. These unique properties allow for a novel technique, resonant scattering with polarized soft X-rays (P-SoXS), in which the morphology of molecularly oriented regions of a sample is probed by scattering preferentially from bonds with anisotropic transition dipole moments, for instance

the p-orbitals in conjugated polymers. If there is some larger range order in the arrangement of similarly aligned orbitals, polarized soft X-rays tuned to an energy with sensitivity to that orbital can then exploit that unique contrast to probe the ordering, even if the sample has a uniform electron density and is chemically homogenous or even amorphous. An example system with this behavior, measured in transmission geometry is P3HT:P(NDI2OD-T2), as shown in Figure 2.5. Here, it is clear that with different polarization of light, a corresponding scattering anisotropy is apparent. With vertically polarized photons, the scattering is enhanced in the horizontal direction and suppressed in the vertical direction. The anisotropy is reversed for horizontally polarized photons and disappears when scattering at non resonant energies when the photons are no longer resonant with the anisotropic p-orbital.

We can now use this material system as a soft X-ray polarimeter and determine limits of the actual polarization of the 285 eV X-rays. The various linear polarizations vs. anisotropic angle shown in Figure 2.5(e) show well behaved linear polarization control. However, changing to circularly polarized light, we see that not all the anisotropy has disappeared. Regardless of orientation of the sample and between different samples, there remains a smaller anisotropy aligned at approximately  $60^\circ$  from the horizontal, revealing an elliptically polarized X-ray beam. Although the EPU can produce elliptically polarized light (and is set to do so, intentionally, when creating 3<sup>rd</sup> and 5<sup>th</sup> harmonic radiation) the residual linear polarization from these settings is either horizontal or vertical, and will not be oriented at an angle. One possible explanation is the carbon contamination discussed above (Section III.C). A small layer of carbon on the optics can cause dramatic phase shifts and selective absorption of reflected X-rays, causing initially circularly polarized light to become elliptically polarized upon

reflection. Limits on the percentage of linear polarization of the light that reaches the endstation can be obtained by comparison of the anisotropy (Figure 2.5). By fitting an azimuthal cross section of the scattering peak to an offset sinusoid, we can decompose a minimally linear component of the beam, by presuming actual circular light does not produce any anisotropy, but only an isotropic offset. Assuming the sample is perfectly anisotropic (zero scattering in

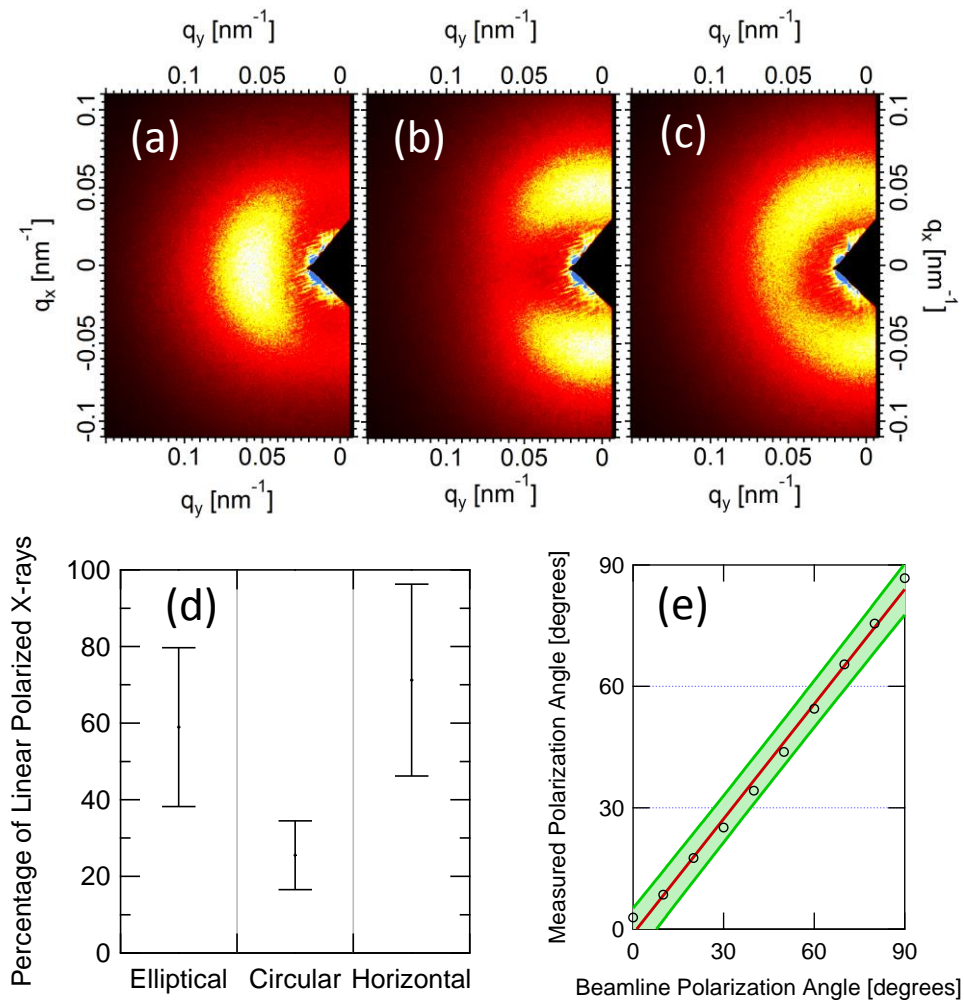


**Figure 2-5 2D Anisotropic Scattering Map**

the same P3HT:P(NDI2OD-T2) sample illuminated with: (a) vertically, (b) horizontally, and (c) circularly polarized X-rays. (d) Range of possible circular and linear components of different settings of polarization. (e) Orientation of anisotropy vs. beamline polarization angle.

the appropriate direction) when probed with truly linear aligned light, we measure a lower limit of 18% actual linearly polarized light when the beamline is set to produce circular. This also gives a lower limit on the purity of the linear polarized light of ~50%. On the other hand, we can find the upper limits by presuming the sample itself produces a certain amount of isotropic signal (a linear offset to the sinusoid) even if the beamline produces purely vertically polarized X-rays when we set polarization to vertical. Analyzing this limiting case, we calculate an upper limit on the amount of linear light while the beamline is set to circular to be 40%. Using similar logic the other limits of in polarization can be determined and are summarized in Figure 2.5.

#### 2.4.5 DETECTOR CHARACTERISTICS

The characteristics of the 2D X-ray detector, i.e. the response to X-rays of different energy, readout properties, and sources of noise need to be understood to allow for quantitative analysis of scattering data.

##### 2.4.5.1 Calibration of Spectral Response of CCD Detector

When striking the back-illuminated CCD, an incoming photon frees some number of electrons in the active layer of the device. The number of these free electrons is proportional to the photon energy.

$$F(E) = kE \quad (4)$$

The fraction of these electrons that avoid recombination long enough to be collected in the CCD pixel over the number initially created is defined as the quantum efficiency  $\eta_e$  of the CCD pixel. This value changes with the energy of the photon, as different energies of photons tend to be absorbed at different depths in the device, creating longer or shorter paths for the electrons they produce to be collected in the pixel and eventually summed by the analog to

digital converter when the CCD is read out. For a single pixel the resulting digital readout  $S$  in Analog to Digital Units (ADUs) is then

$$S(E) = N_{ph}\eta_e(E)F(E)g_e \quad (5)$$

Where  $N_{ph}$  is the number of photons incident on the pixel and  $g_e$  is the electron gain of the analog to digital converter. This relation can be simplified by combining the constants into one effective photon spectroscopic gain  $g_{ph}$ , which will vary with energy along with the quantum efficiency.

$$g_{ph}(E) = \eta_e(E)g_e \quad (6)$$

Thus the number of photons  $N_{ph}$  that actually hit the pixel using equations (4), (5) and (6) is

$$N_{ph} = \frac{S(E)}{g_{ph}(E)E} \quad (7)$$

The quantum efficiency is well understood [126], and so if we can measure the photon spectroscopic gain at one energy, we can calculate it at any energy using equation (6) and use this value to convert the output of ADUs/ pixel into an actual number of photons/ $\Delta q$  and thus a quantitative scattering cross-section.

We measure the photon spectroscopic gain of the 2D detector by exposing it to evenly dispersed, sparse, relatively high energy photons, such that the exposure of the CCD consists of well-separated, single photon events. The spatial spread of secondary electrons (the point spread function) produced by a single photon is not guaranteed to lie entirely within one pixel. It is in fact a minority of pixels that contain all the electrons produced by a single photon. This causes the histogram of ADUs per pixel to be spread out, making it difficult to distinguish

single photons, particularly when the electron yield is low (generally at lower energies). At 1500 eV however, a separate peak of pixel values is clearly distinguishable from the distribution of partially filled and unilluminated pixels ( $\sigma \sim 8$  ADUs) (Figure 2.6). Repeated measurements and histograms of resulting pixel values at X-ray energies down to approximately 1000 eV were possible as this peak remained clearly separated from the

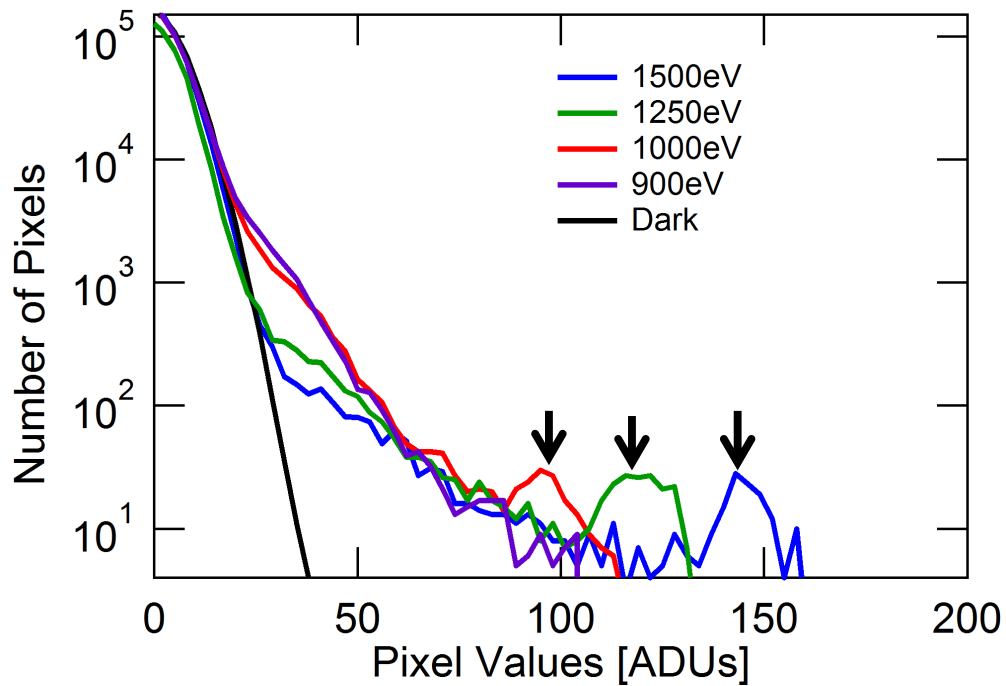


**Figure 2-6 Histograms of Pixel values**

CCD readout at 1500 eV, 1250 eV, 1000 eV, and 900 eV for low intensity illumination ( $\ll 1$  photon/pixel) and dark counts for comparison. Single photon event peaks in the histograms are pointed out for the higher photon energies.

background peak. No peak is observed when the CCD is exposed to 900 eV and lower energies.

To extrapolate from these values to the photon gain at different energies, the varying quantum

efficiency [126] must be taken into account. At the carbon edge,  $\eta_e(285eV)$  is roughly equal to  $\eta_e(1500eV)$ , meaning

$$g_{ph}(285eV) \cong 10 \pm 1 \frac{ADU}{Photon \times eV} \quad (8)$$

so at 280 eV the CCD returns ~28 ADUs per photon.

#### 2.4.5.2 Noise Characteristics of Detector

Noise in a CCD originates primarily in two ways: dark noise is accumulated along with the data during integration and read noise is generated effectively once per exposure during readout. With any detector geometry, light-leaks in the chamber and noisy pixels will cause a certain fixed-pattern dark noise proportional to the exposure time. Fortunately for any set of data, a set of dark datasets in the same detector geometry and same exposure time can be subtracted from the collected 2D scattering patterns prior to analysis to essentially remove dark noise. It is found that careful covering of all windows on the chamber and cooling the detector to  $-45^\circ$  C once under vacuum, reduces the dark noise to low levels, however exposures over a second in duration still improve dramatically with subtraction of an identically exposed image keeping the X-ray shutter closed. In this way fixed pattern noise that accumulates in an identical exposure time and geometry can be removed. While taking longer dark images would reduce the additional uncertainty added by the Poisson statistics of the fixed pattern noise, the properties of the detector change substantially both with the immediate light conditions of the sample chamber and the longer term growth of hot pixels. For these reasons we find that to ensure optimal data reliability, it is best to take an identically exposed dark image with each set of exposures.

Readout noise is in general much more difficult to predict and mitigate, particularly with current in-vacuum CCD Systems. We show that in this system read out noise changes significantly with each exposure. A histogram of the offsets and standard deviations of a set of identically exposed dark images (Figure 2.7(a) and (b)) shows the variability of both of overall scale and functional form of the readout noise. The height of the horizontal profile in Figure 2.7(c) shows that the variation in the intensity within a single exposure can account for as much as 2 photons/pixel from the left to right side of the detector. The problem seems to arise from electronic heating during readout and is difficult to mitigate electronically for in-vacuum systems. Vertical profiles show no significant variation because this is the fast readout direction of the CCD and significant electronic heating cannot occur over this timescale. Single frame variation can be reduced by going to a 2 x 2 binned mode, however there is still an exposure to exposure shift, which is much more difficult to correct for. The width of the histogram of average values before background correction shows that the shift from exposure to exposure can be as much as 10 photons/pixel in overall background intensity. To correct for each of these readout errors and their variations over time, both within each individual exposure and between subsequent exposures, we blocked the lower section of the detector, insuring that part of each 2D data set is essentially a simultaneous dark exposure. The dark portion can then be vertically integrated to a horizontal profile and fit to an empirical double exponential function (Figure 2.7(c)). This fit can then be used to correct each row of the exposure for both the variation in readout level and overall background level of that dataset. The results of readout correction are shown in the histograms of data (Figure 2.7(a) and (b)) before and after application of the correction process. After correction, the variation in overall

offset is essentially removed to less than one ADU, while the shift in the background within each exposure is reduced significantly as can be seen in the histogram in Figure 2.7(b) and the 2D dataset example shown in Figure 2.7(d).

#### 2.4.6 DATA COLLECTION AND LIVE ANALYSIS

Software developed for 11.0.1.2 has features including correction for photon quantum efficiency and automatic background correction as described in the previous sections. In addition, routines have been developed that make it possible for live analysis of scattering data while the data is being read out from the detector. An IGOR-based analysis program (Figure

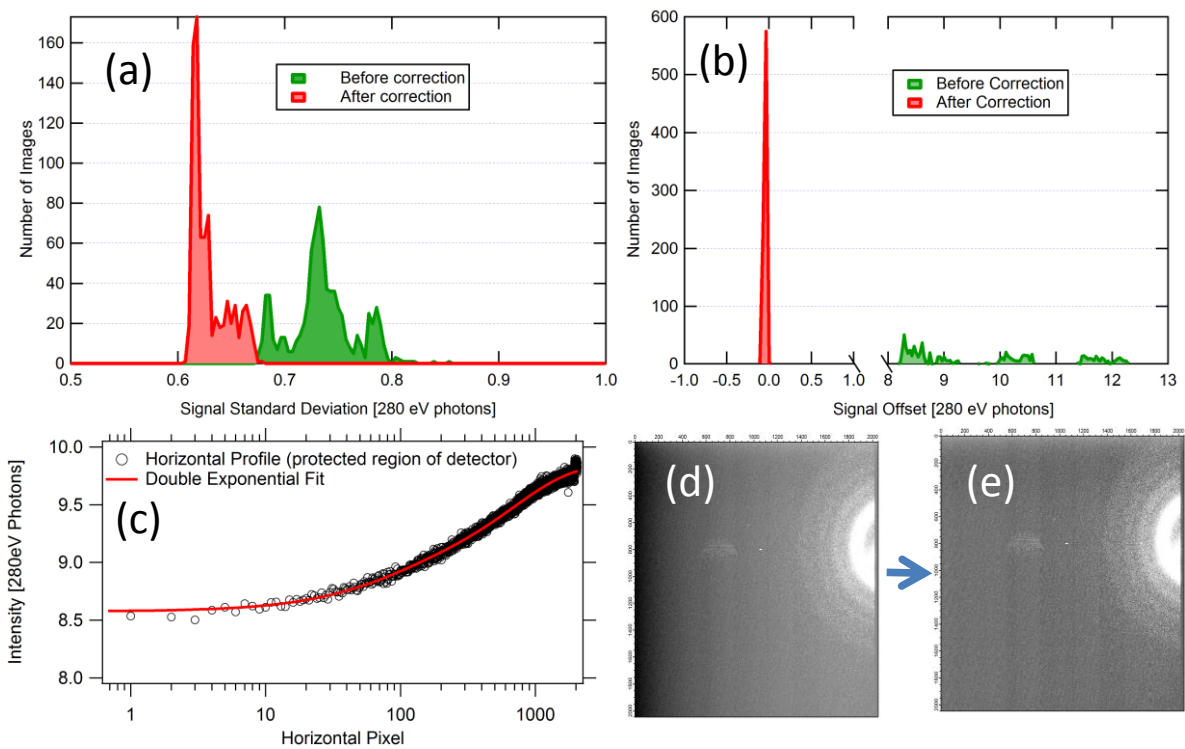


**Figure 2-7. Noise Analysis of Detector**

(a) Histograms of the standard deviations and (b) average values of all the pixels in each of 800 dark exposures before (green) and after (red) correction by subtracting a horizontal double exponential from each frame. c.) A double exponential fit to the ADU values in a covered section of the detector in one exposure. (d) An example of uncorrected and (e) corrected scattering pattern, illustrating the flattening process.

2.8), based on the NIKA data processing program [121] has been implemented that can perform all the typical analysis steps as data is recorded. First the geometry and energy calibrations are measured using a set of calibration samples with known spacings and energy responses. The analysis program fits the characteristic scattering rings from the chosen calibrant to determine the geometry of the sample and detector in the same procedure as in hard X-ray scattering calibration [119]. Various forms of data analysis are available, including radial integrations, sector integrations, line cuts, or some combination. After the data analysis mode is chosen and a dark image or series of dark images is acquired with the same exposure times of the data to be collected, the “auto analyzer” feature is turned on. As data is collected, a reduced form of the data (typically an  $I(q)$  graph) is produced and optionally plotted, allowing for immediate feedback of data quality, ensuring efficient and effective use of beamtime. Movements of the sample or CCD geometry, the parameters of the X-ray optics and apertures including the polarization and energy are recorded and data processing parameters are automatically adjusted as necessary (i.e. for a new beam center) to reflect the new state of the beamline.

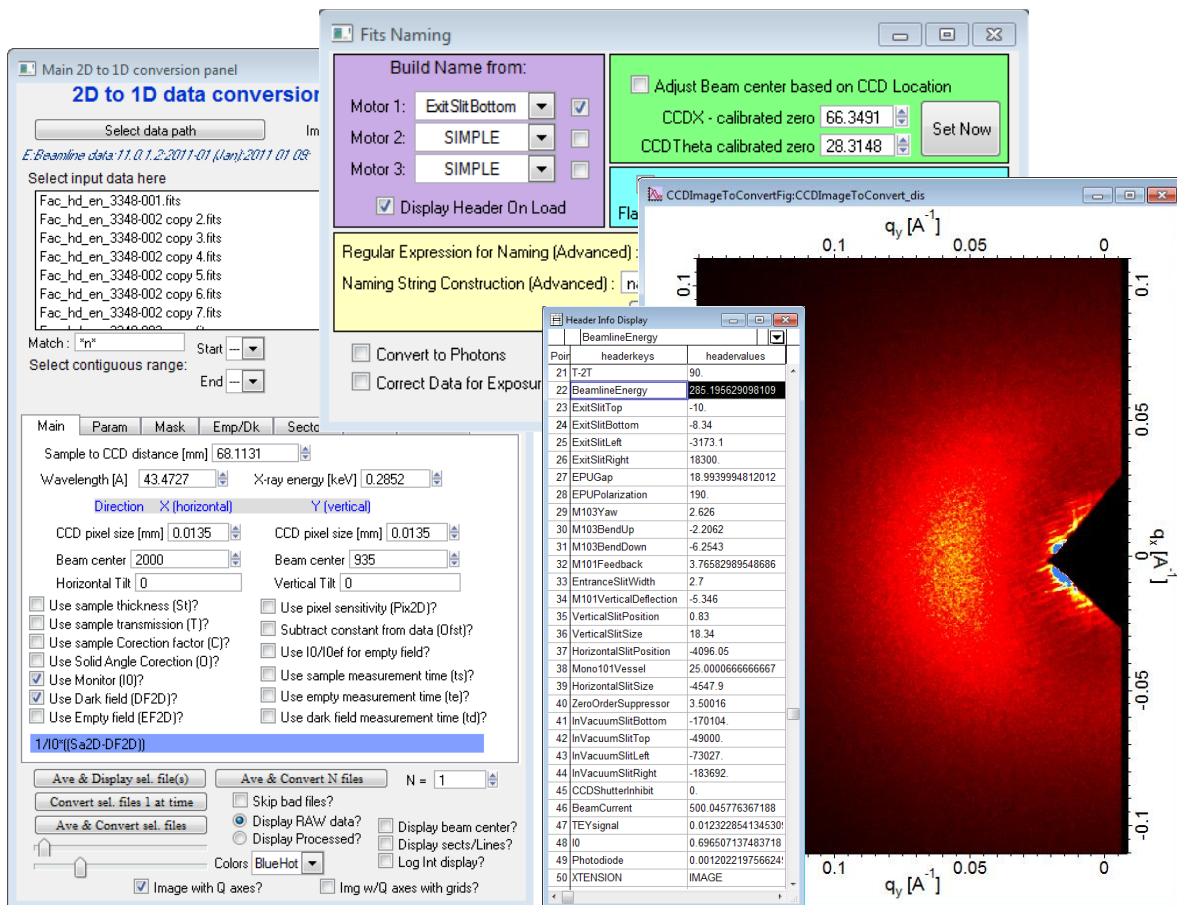


**Figure 2-8 User Interface**  
Program created for Beamline 11.0.1.2 real time quantitative scattering analysis.

## 2.5 RESULTS

### 2.5.1 EXAMPLE OF DATA TILING AND LIMITS OF Q RANGE

To reach the maximum range of momentum transfer that the beamline is capable of, exposures at varying detector locations are necessary. Procedures have been developed to allow acquisition of scattering to  $2\theta > 90^\circ$  although certain geometrical aspects of the sample environment have thus far limited acquisition to  $2\theta < 50^\circ$ . This corresponds to reaching a small feature limit of approximately 5 nm with use of 280 eV photons (see Figure 2.9). For the lowest

q possible, the detector is moved to its furthest distance from the sample (168 mm). In transmission geometry, an additional 25 mm of distance can be gained for a total distance of 195 mm by moving the z motor of the sample stage to the upstream limit. In four exposures, one with the CCD centered and the sample-CCD distance maximized at 193 mm and one each with sample located in the center of the goniometer at a distance of 80 mm and while the detector is at 10°, 25° and 45° from horizontal, a q range spanning nearly 3 orders of magnitude is readily obtainable. This is shown on a sample of drop cast 300 nm polystyrene nanospheres in Figure 2.9. At each location, calibration data could be recorded, but the live analysis software can also extrapolate the change in geometry automatically by monitoring the motor positions. Thus, a single plot of scattered intensities vs. momentum transfer can be built by simply moving the detector and taking successive exposures.

Operation in grazing geometry makes using the extra distance afforded by moving the sample to the upstream limit more difficult if not impractical, as the exact grazing angle determination is only readily done when the surface of the sample is in the center of rotation of the 2-circle diffractometer. Although the low q-limit is thus theoretically slightly increased over use of the facility in transmission geometry, the added geometrical benefit of stretching the in plane scatter in the specular direction actually allows measurement beyond the limit allowed in transmission, probing features up to the coherence limit of 5  $\mu\text{m}$  in the plane of the sample.

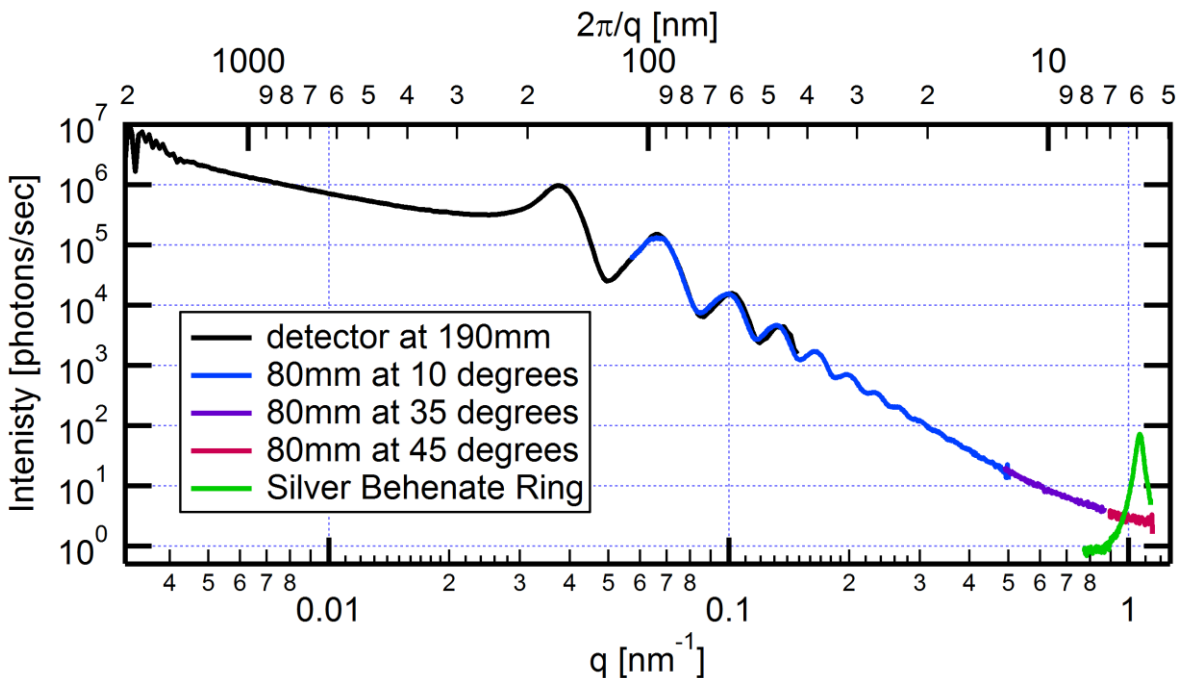


**Figure 2-9 Example of Tiling**

Tiled detector geometries generate a single scattering intensity vs.  $q$  plot for drop cast 100 nm poly(styrene) nanospheres spanning an effective size range of 5 nm to 2  $\mu\text{m}$ , and a silver behenate powder diffraction ring at 5.8 nm for reference

### 2.5.2 EXAMPLE APPLICATION IN TRANSMISSION GEOMETRY: P3HT:PCBM

R-SoXS has been found useful in characterizing a number of blends used for organic bulk heterojunction (BHJ) solar cells [21, 34, 76, 127]. Samples are conveniently investigated in transmission as thin films prepared precisely in the way they are for the devices. We show as an example the R-SoXS results of a P3HT:PCBM blend, a relatively high-performing system used in organic solar cells. The radially averaged R-SoXS intensities from a 250 nm thick film annealed at 150°C for 30 min are plotted in Figure 2.10 for 284.2 eV and 270 eV photon energy. Due to the energy dependence of the optical constants of the constituents and thus their contrast, the scattering intensity profiles show strong energy dependence. At 284.2 eV, the scattering contrast between P3HT and PCBM constituents is optimized. The spacing

corresponding to the feature observed is  $2\pi/q \approx 20$  nm. At 270 eV, the contrast between P3HT and PCBM is much reduced. The energy dependence of R-SoXS can thus be readily exploited and provides crucial information that can be taken into consideration when analyzing the data with more conventional methods.

Other applications to date in the transmission geometry include various block copolymer systems [56, 75, 127], dilute solutions and suspensions [77], low dielectric polymer thin films [104], and organic thin film transistors [1].

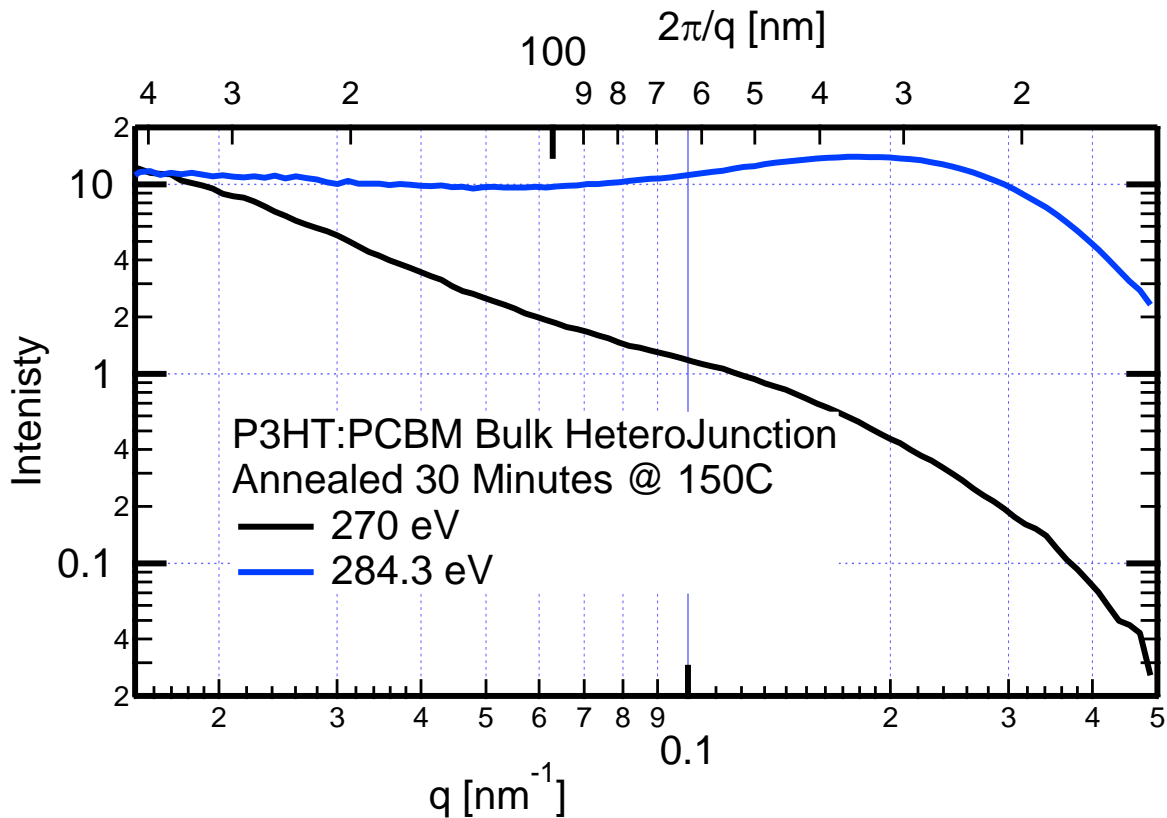


**Figure 2-10 RSoXS Example**

Scattering intensity vs. momentum transfer for transmission X-rays at resonant (284.3 eV) and nonresonant (270 eV) X-ray energies for annealed (30 min 150 °C) P3HT:PCBM BHJ film.

### 2.5.3 EXAMPLE APPLICATION IN GRAZING INCIDENCE GEOMETRY: BLOCK COPOLYMERS

Scattering from grazing incidence geometry has numerous benefits. As in hard X-ray grazing incidence scattering, the incident X-ray dose on the sample is minimized, while the scattering path in the sample is maximized, meaning sample damage is minimized while scatter intensity can be simultaneously maximized. In addition, a single CCD exposure can capture both the in-plane structure as probed in transmission geometry and out of plane structure as probed in reflectivity. When this is added to the chemical sensitivities of soft X-rays, a powerful and unique tool for measuring thin film structure is achieved. For example, the structure of an IS2VP tri-block copolymer thin film was characterized using grazing incidence soft X-ray scattering as shown in Figure 2.11. 2D scattering intensities in the in-plane ( $q_{xy}$ ) direction integrated within a narrow rectangle along the Bragg-rods are shown in Figure 2.11. The location of the Bragg rods (see 250 eV data as example) reflects the in-plane structure, while the modulation along the rods in the  $q_z$  direction reveals the out-of-plane structure – the film thickness in this case. Based on the in-plane  $q$ -spacing of the first, second and third diffraction order, we can conclude that the 40 nm thin film contains hexagonal packed in-plane structure with long-range order. Interestingly, the variation in the relative diffraction peak intensities at different energies suggests a core shell structure.

Traditional techniques have difficulty determining this structure because the scattering intensity is the multiplication of the form factor and the structure factor (interference function) and when samples contain long range order, the diffraction from the structure factor dominates the form factor. Decoupling the form and structure factors requires changing the relative contrasts, which can be rather challenging with traditional techniques. While contrast matching is possible in neutron scattering, it requires adjusting the  $^1\text{H}/^2\text{H}$  ratio during synthesis of one or two of the blocks. R-SoXS, as demonstrated in this case can tune the contrast between the polymer blocks simply by changing photon energy. Varying the effective contrast changes the form factor of the object and relative peak intensities in the scattering pattern, while the structure factor remains the same. As can be observed in Figure 2.11, the relative peak intensity of the various diffraction orders is indeed a strong function of photon energy, confirming a

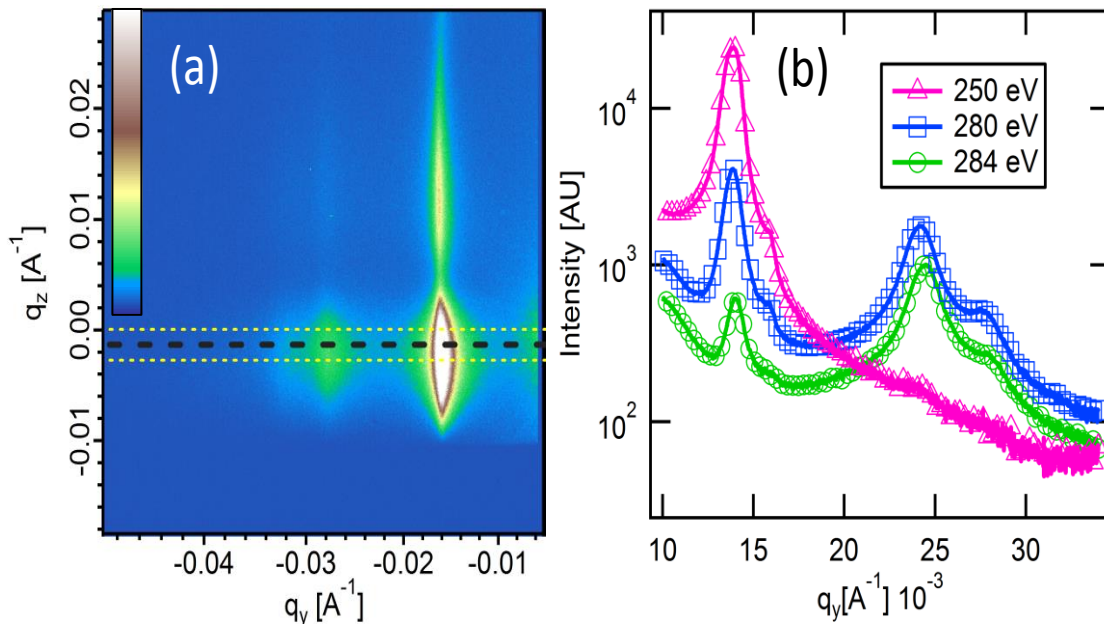


**Figure 2-11 Grazing Incidence Example**

(a) 2D scatter plot from IS2VP thin film. Increasing in plane momentum transfer ( $q_{xy}$ ) is to the left, while increasing out of plane momentum transfer ( $q_z$ ) is upward with zero offset to the reflected beam center. (b) Horizontal ( $q_{xy}$ ) profiles

dual cylindrical structure. Quantitative modeling as well as stained electron tomography confirm this result and provides additional details about the relative length scales and geometry of different cylinders [56].

## 2.6 V. DISCUSSION

We have shown methods addressing many of the difficulties encountered with obtaining artifact free scattering data near the carbon K absorption edge. Higher harmonic spectral components of the beam are measured with a diffraction grating and removed by a four bounce Ni-coated mirror adjusted to a sufficiently high angle. New methods in measuring the polarization content of the X-ray beam around the carbon edge were presented and show that actual circular polarization is difficult to obtain, which is likely the result of carbon contamination on beamline optics. Methods for obtaining photon counts from the readout of a 2D in-vacuum back illuminated CCD were developed. Procedures to measure and correct for noise sources applicable to any in-vacuum 2D detector system able to record photon energies in this range were developed. Finally, we have presented a live analysis system that is able to accomplish the initial reduction and analysis of data immediately as data is acquired. With all these methods and characterizations, we ensure efficient, normalized, corrected and quantified scattering data acquisition in this difficult but uniquely useful X-ray energy range.

In spite of the significant improvements achieved with the present facility and the procedures for working around certain difficulties, there are several aspects that can and must be improved in order to take full advantage of the intrinsic capabilities. Foremost amongst these are the carbon contamination on the optics, improved accuracy of absolute scattering intensity, and control of the sample environment.

Mitigating carbon contamination is a central concern for soft matter systems, in which case those energies that are most effective in probing morphology are also those affected most by carbon contamination. The negative impact on the polarization by the anisotropic carbon contamination is particularly detrimental and cannot be compensated for by longer exposure times or use of higher order suppression. There has been success on other beamlines of cleaning the optics in situ by leaking in a low pressure of O<sub>2</sub>, which when exposed to X-rays or secondary electrons near the optics creates reactive oxygen species that react with the carbon on the surface to create volatile compounds that can be pumped away [128, 129]. Alternatively, direct creation of an reactive glow-discharge plasma can be used [130]. This method, however, works best with line-of sight between the RF-reactor and the optics. It also necessitates a bake-out after cleaning. Alternatively, optics can be cleaned ex-situ with a UV-lamps or a standard UV-ozone cleaner, or the coating can be stripped and a new one evaporated. Very recently, an effort at 11.0.1.2 to mitigate the carbon contamination by removing and cleaning the main mirrors in this way was completed successfully, improving the flux of 284eV photons by more than an order of magnitude.

Certain problems with the beamline and facility are intrinsic to the specific hardware installed and can thus be mitigated only by upgrading the hardware. In vacuum, two dimensional soft X-ray detectors have been very useful for efficient scattering detection. However, the detector currently installed in 11.0.1.2 has been shown to have various readout issues that affect absolute measurements which we describe above. Even though we have mitigated these issues with automated corrections, newer detector technology such as active pixel arrays with single photon counting capabilities will be ideal for future development.

Although the present detector and facility provides a significant improvement over use of point detectors, only approximately 3% of the desired solid angle of  $\Omega = 2\pi$  is detected. 2D detectors or arrays of detectors that cover a larger angular range would be able to further improve the throughput and signal/noise ratio for intensity measurements at high  $q$  while also reducing the radiation damage of the organic samples. This will become increasingly important as more tightly focused X-ray beams might be used to investigate smaller samples. Given the large scattering angles present for scattering of soft X-rays, development and implementation of a large solid angle detector will be not trivial to achieve.

The present low  $q$  limit cannot be significantly improved given the source and beamline optics and the current sample-detector distance, which is limited by the size of the scattering chamber. A second detector mounted permanently on the X-ray axis in the upstream wall of the scattering chamber will decrease this low  $q$  limit to the coherence minimum of the X-ray beam.

Sample environmental control such as heating/cooling, the use of liquid or gas cells, and magnetic and electric fields, would further broaden the utility of the facility presented, allowing *in-situ* measurement of the evolution of numerous systems.

There are many further areas of development for soft X-ray scattering. Grazing incidence developments include utilizing the varying optical properties of various materials near absorption edges, which should enable selectively scattering from an internal interface by careful choice of X-ray energy where the contrast of that particular interface is maximized. In all scattering experiments, but in soft X-ray systems perhaps even more so, the development of analytical and statistical modeling and fitting tools are critical to fully utilize the power of

these techniques. In this direction, new tools are being developed to allow real space and Fourier space techniques to work together to determine both local and structure and long range order within important systems.

## 2.7 VI. CONCLUSION

By utilizing the selective contrast to composition and orientation afforded by use of photon energies near the carbon absorption edge, R-SoXS is proving particularly valuable in revealing structure-properties relationships. Most applications to date have focused on characterizing systems based on synthetic materials. Similar to other scattering methods, R-SoXS is however a general characterization method that we expect to be used in many disciplines and across many materials classes that will eventually include biological, environmental and organic geochemical materials. We anticipate a development similar to what has occurred in the field of transmission NEXAFS microscopy, which has initially also been demonstrated utilizing polymers [91, 92] and which has subsequently been used in wide range of disciplines that span geology [131], chemistry [132], polymer science [133], and biology [134]. However, unlike the situation in microscopy where edges of samples are of little consequence and rather small samples can be studied with ease, edges introduce strong unwanted parasitic scattering if the sample is smaller than the photon beam. This parasitic scattering might limit the range of samples that can be investigated until such time that more tightly focused X-rays beams become available.

In many instances, quantitative analysis required for many applications necessitates knowing the correct intensity across the full  $q$ -range in order to achieve correct structure factors and correlation functions, and calculation of the scattering invariant  $Q$ . Given that the desired

data often spans six orders of magnitude, the limited per-pixel dynamic range of the present CCD to a little more than  $10^3$  and the various sources of noise thus necessitate extensive experimental care when tiling q-ranges or comparing data sets at different energies. Development and use of more advanced detectors that facilitate accurate measurements is thus highly desirable. In general, the goal for the R-SoXS community will have to be to match the accuracy achieved by the more developed and matured ASAXS and SANS communities. The developments presented here are a necessary first step.

An interesting direction for future development of this facility would take advantage of the high brightness of the undulator source by illuminating the sample coherently. Recent developments in X-ray photon correlation spectroscopy and coherent diffractive imaging techniques such as HERALDO and ptychography show great promise for characterizing nanoscale morphologies in real space or probing dynamic phenomena [113, 135]. These methods take advantage of the full-beam coherence to invert the scattering pattern into a real space image. This would allow for truly diffraction-limited resolution, thus affording much higher spatial resolution X-ray microscopy than current techniques can provide.

There are several soft X-ray scattering facilities existing or under construction at synchrotron facilities around the world, including efforts at SOLEIL, Electra, and NSLS. However, these facilities are not specifically designed to characterize soft matter and so aren't necessarily concerned with carbon contamination and the numerous problems it creates. Our focus on optimizing work near the vicinity of the carbon K absorption edge, combined with the high brightness available at the ALS, makes the facility described here a unique and important characterization tool for soft matter systems.

## 2.8 ACKNOWLEDGEMENTS

We gratefully acknowledge fruitful discussion about the facility and soft X-ray scattering in general with E. Gullikson (CRXO, LNBL) and J. Kortright (LBNL). We thank E. Gullikson for providing the diffraction grating, C. McNeil (Monash University) for the P3HT:P(NDI2OD-T2) sample, and Dong Hyun Lee for the (PI-*b*-PS-*b*-P2VP) triblock copolymer sample. We thank J. Seok (now at Intel) for creating the P3HT:PCBM bulk heterjunction sample. We also gratefully acknowledge E. Domning and B. Smith from the ALS controls group for their continuing development of the 11.0.1.2 control software. Funding at NCSU provided by DOE (DE-FG02-98ER45737). EG and HY were also supported by a GAANN and ALS Fellowship, respectively. Data acquired at ALS beamline 11.0.1.2. This work was supported by the Laboratory Directed Research and Development Program of Lawrence Berkeley National Laboratory under the Department of Energy Contract No. DE-AC02-05CH11231.

## *Chapter 3*

### **MODEL FREE ANALYSIS OF SOFT X-RAY SCATTERING IN PHASE SEPARATED SYSTEMS**

This chapter is a prepared manuscript delineating and testing analysis techniques and rules of thumb commonly used in soft X-ray scattering experiments from phase-separated systems such as OPVs. There is confusion and disagreement in the field as to how to analyze results, and what exactly a scattering pattern can say about the system it comes from. For this reason, we decided that some modeling was appropriate to quickly test hypotheses, concerns, and analysis techniques robustly. Particularly, it has become necessary to rigorously prove the central theory of soft X-ray scattering, the mechanism of contrast, and how it is properly calculated and understood. Although the topics in the paper may seem somewhat disparate, they all fall into the general category of determining quantitative information in high volume fraction, phase separated systems.

Maolong Tang wrote the initial proof which turned into section 3.3.1, as well as the Mie scattering code which produced the raw data that went into section 3.4. John Tumbleston and Harald Ade aided in the initial conception of the need for this paper, and what should be shown. I performed the design and writing of all the analysis techniques and simulations, and chose the simulated parameters.

## Model Free Analysis of Soft X-ray Scattering In Phase Separated Systems

Eliot Gann<sup>1</sup>, John R. Tumbleston<sup>1</sup>, Maolong Tang<sup>1</sup>, Harald Ade<sup>1</sup>

<sup>1</sup> Department of Physics, NCSU, Raleigh, NC 27695-8202

### 3.1 ABSTRACT

A strategy of maximizing the utility gained by the use of Soft X-ray Scattering in the morphological characterization of high volume fraction systems is examined. Blends of organic materials are often central to important devices, such as organic photovoltaics (OPVs). In these materials, it is generally a near-equal mixture of materials that is spun cast from solvent into a thin film, which is then scattered from in a Resonant Soft X-ray Scattering (RSoXS) experiment. Yet, the analysis of this scattering is done in relatively disparate and contradictory ways, applying different models to the same system, and obtaining inconsistent results. Full advantage has not been taken of the full potential of model free analysis available with only minimal information such as the volume fraction and optical constants of components. We derive the contrast mechanism of soft X-rays, and test the validity of the Born approximation in simulated systems, determining some practical limits of the approximation in organic systems. We show through a multitude of simulations the correlation between different measures often used in analysis of scattering patterns and the designed morphology particularly the average domain size and spacing that created the pattern. Finally we examine several ways of retrieving size scales from a system with multiple length scales, including a combination of Lorentz corrected one dimensional patterns and Chord Length Distributions.

## 3.2 INTRODUCTION

Soft X-ray scattering is a burgeoning technique which has recently been used in the determination of morphology of organic blend systems [75, 77, 136]. The unique contrast enhancement available at the carbon absorption edge allows fingerprinting of materials, and targeting certain structures within a thin film [12, 82]. Determining the optical constants of pure materials ahead of a scattering experiment [137], and determination of all the potential contrasts in the system and the energy behavior of them, can allow much more precise knowledge to be gained.

Next, we rigorously prove the often stated relationship between the index of refraction and scattering in these systems, that the scattering is proportional to the modulus squared index of refraction. We also calculate the full scattering solution in systems of relevant scales and contrasts to OPV experiments, and show that the Born approximation is appropriate for these materials, even at resonance peaks. The scattering patterns from a full treatment and the Born approximation are nearly indistinguishable.

The interpretation of scattering patterns often either identify peaks and shoulders of one dimensional radially averaged scattering patterns as size scales, or use a model to derive morphological size scales present in the system. In these irregular systems, it is often appropriate to use liquid-liquid models, which do not often give morphological information of interest, which are generally domain size and spacings. We examine the fundamental principles of scattering from a binary system, and take a statistical look at what connections can be made concretely between realistic scattering patterns and morphology without imposing a model.

Finally, beyond just obtaining average properties of a system, we show how multiple size scales can be recovered from scattering patterns reliably, by looking at the chord length distribution.

### 3.3 THEORY

#### 3.3.1 SCATTERING BASICS

Developing the scattering theory in the Soft X-ray regime, it is informative to go back to basic principles. We define an incident x-ray wave  $\vec{E}_i(\vec{r}, t)$  as a plane wave, where  $\vec{E}_0$  is a constant electric field vector,  $\vec{k}_i$  is the incident wave vector.

$$\vec{E}_i(\vec{r}, t) = \vec{E}_0 \cdot e^{i\vec{k}_i \cdot \vec{r} - i\omega t} \quad (1)$$

And the displacement vector field  $\vec{D}(\vec{r}, t)$  in a dipole field of permittivity  $\epsilon$

$$\vec{D}(\vec{r}) = \epsilon \vec{E}(\vec{r}) = \vec{E} + 4\pi \vec{P} = (1 + 4\pi\chi_e)\vec{E} \quad (2)$$

Where  $\vec{P} = \chi_e \vec{E}$  is polarization field and  $\chi_e$  the electric susceptibility. We connect  $\epsilon$  to  $n$  by the relation

$$n^2 = \epsilon = 1 + 4\pi\chi_e \quad (3)$$

Which is technically a tensor. This relation is correct when the magnetic permeability  $\mu$  is very close to 1. Then the born approximation gives  $\vec{E} = \vec{E}_i$  or

$$\vec{P} = \overleftarrow{\chi}_e \vec{E} = \frac{\tilde{n}^2 - 1}{4\pi} \cdot \vec{E}_i = \left( \frac{\tilde{n}^2 - 1}{4\pi} \cdot \vec{E}_0 \right) e^{i\vec{k}_i \cdot \vec{r} - i\omega t} = E_0 e^{i\vec{k}_i \cdot \vec{r} - i\omega t} \vec{K} \quad (4)$$

Where  $\vec{K} = \overleftarrow{\chi}_e \cdot \hat{E}_0$  and  $E_0 = |\vec{E}_0|$ . In the far field (in the direction of  $\hat{r}$ ), only the transverse or off diagonal elements contribute to  $\vec{K}$

$$\vec{K}_\perp = (I - \hat{r}\hat{r}) \cdot \vec{K} = (I - \hat{r}\hat{r}) \cdot \left( \frac{\vec{n}^2 - 1}{4\pi} \cdot \vec{E}_0 \right) \cdot \frac{\vec{E}_0}{E_0} \quad (5)$$

So the electric field  $\vec{E}$  and magnetic field  $\vec{H}$  in the far field are

$$\vec{E}_{\text{ff}} = -\frac{k^2 E_0 e^{i(kr - i\omega t)}}{r} \int d^3\vec{r}' \vec{K}_\perp(\vec{r}') e^{i(\vec{k}_i - \vec{k}_o) \cdot \vec{r}'}$$

$$\vec{H}_{\text{ff}} = \hat{r} \times \vec{E}_{\text{ff}}$$
(6)

where  $k = |\vec{k}|$ , which is the magnitude of the wave vector ( $\frac{2\pi}{\lambda}$ ). The scattered intensity ( $I$ ) is equal to the time averaged Poynting vector in the far field, which is therefor (see Jackson [138] page 411)

$$I = \langle \vec{S} \rangle = \frac{c}{8\pi} \vec{E} \times \vec{H}^*$$

$$= \frac{c}{8\pi} (\vec{E} \cdot \vec{E}^*) \hat{r}$$

$$= \frac{ck^4 E_0^2 \hat{r}}{8\pi r^2} \int d^3\vec{r}_1 d^3\vec{r}_2 (\vec{K}_\perp(\vec{r}_1) \cdot \vec{K}_\perp^*(\vec{r}_2)) e^{i(\vec{k}_i - \vec{k}_o) \cdot (\vec{r}_1 - \vec{r}_2)}$$
(7)

Going back (5) and simplifying in the case that  $n$  is a scalar to

$$\vec{K}_\perp(\vec{r}_1) \cdot \vec{K}_\perp^*(\vec{r}_2) = \frac{1}{4\pi^2} (1 - (\hat{r} \cdot \hat{E})^2) (n(\vec{r}_1) - 1)(n^*(\vec{r}_2) - 1) \quad (8)$$

where  $\hat{r}$  is the unit vector in the direction of the outgoing wave front  $\vec{k}_o$ , i.e. towards the observer, and  $\hat{E}$  is the polarization of the incoming wave, so that  $\hat{r} \cdot \hat{E} = \cos \theta$  and  $1 - (\hat{r} \cdot \hat{E})^2 = \sin^2 \theta$  where  $\theta$  is the angle between the polarization and outgoing vectors. Using this, by defining  $\vec{q} = \vec{k}_i - \vec{k}_o$ , and (8), we can simplify (7).

$$I(\vec{q}) = \frac{ck^4 E_0^2 \hat{r}}{8\pi r^2} \sin^2 \theta \left| \int d^3\vec{r}_1 d^3\vec{r}_2 (n(\vec{r}_1) - 1)(n^*(\vec{r}_2) - 1) e^{i\vec{q} \cdot (\vec{r}_1 - \vec{r}_2)} \right|^2 \quad (9)$$

$$I(\vec{q}) = \frac{ck^4 E_0^2 \hat{r}}{8\pi r^2} \sin^2 \theta \left| \left( \int d^3\vec{r}_1 (n(\vec{r}_1) - 1) e^{i\vec{q} \cdot \vec{r}_1} \right) \left( \int d^3\vec{r}_2 (n^*(\vec{r}_2) - 1) e^{i\vec{q} \cdot \vec{r}_2} \right) \right|^2 \quad (10)$$

$$I_{eq}(\vec{q}) = \frac{ck^4 E_0^2 \hat{r}}{8\pi r^2} \sin^2 \theta |\tilde{n}(\vec{q})|^2 \quad (11)$$

where  $\tilde{n}(\vec{q})$  is the Fourier transformed  $n(\vec{r})$  and we have discarded the constant offsets which when Fourier transformed only contribute  $\delta(q)$  functions at  $\vec{q} = \vec{0}$ . Scattered photons at  $\vec{q} = \vec{0}$  are not experimentally measurable, so  $I_{eq}(\vec{q}) \equiv I(\vec{q} \neq \vec{0})$

### 3.3.2 CONTRAST DERIVED

When we make the simplification at these energies that  $n - 1 \ll 1$  so it is useful to split  $n$  into the very small real deviation from 1 ( $\delta$ ) and the imaginary absorptive deviation from zero ( $\beta$ )

$$n = 1 - \delta + i\beta \quad (12)$$

Consider a binary system where the two components with indices of refraction  $n_1$ , and  $n_2$  fill all space. This means that the relative concentrations  $c_i(\vec{r})$  have a value between 0 and 1 for all  $\vec{r}$  and

$$c_1(\vec{r}) + c_2(\vec{r}) = 1 \quad (13)$$

We can do some math and redefine the index of refraction in terms of these spatial variations

$$n(\vec{r}) = n_1 c_1(\vec{r}) + n_2 c_2(\vec{r}) \quad (14)$$

Using (13) and defining  $\Delta n \equiv n_2 - n_1$

$$\begin{aligned} n(\vec{r}) &= n_1 + (n_2 - n_1)c_2(\vec{r}) \\ &= n_1 + \Delta n c_2(\vec{r}) \end{aligned} \quad (15)$$

This usefully puts all the spatial variations into one scalar field  $c_2(\vec{r})$ . Using the properties of the Fourier transform, if again we are only interested in  $|\vec{q}| \neq \vec{0}$ , the constant offset in the Fourier transform drops out, and we can further simplify equation (9) to

$$\langle \vec{S} \rangle = \frac{ck^4 E_0^2 \hat{r}}{8\pi r^2} \sin^2 \theta |\Delta n|^2 |\tilde{c}_2(\vec{q})|^2 \quad (16)$$

We can now define the contrast between the two materials as  $|\Delta n|^2$  which from (10) can be written as

$$|\Delta n|^2 = |\delta_1 - \delta_2|^2 + |\beta_1 - \beta_2|^2 = \Delta\delta^2 + \Delta\beta^2$$

This definition is useful in comparing different systems as delta and beta change, the scattering form factor encoded in  $|\tilde{c}_2(\vec{q})|^2$  will not change, while the materials contrast does.

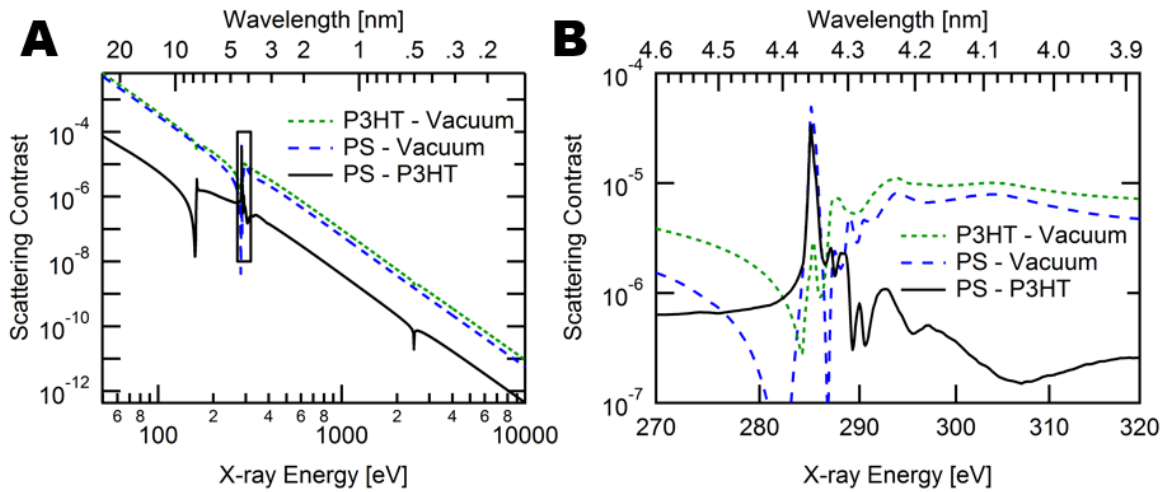


**Figure 3-1 Scattering Contrasts**

Scattering contrasts calculated from absorption data for two materials, P3HT and PS in vacuum. (both of these materials, along with PCBM are used in the Mie scattering simulations in Fig. 3.2) A) A zoomed out view of scattering contrasts over a huge range of X-ray energies, from the UV into the hard x-rays. The vacuum contrasts are dominant through much of this range with the one exception being near the carbon edge. B) A Zoom into the boxed region in A, showing the complex contrast behavior near the carbon absorption edge.

Also, interestingly, all the X-ray energy (or wavelength) dependence is in  $\Delta n$  not  $c_2(\vec{r})$ . Example contrasts are shown in Figure 3.1

The same behavior here derived for a binary system, can be derived for a systems composed of many elements. In each case, the contrast between any two elements can be defined, although the total scattering factor is a sum of all of the spatial functions. When the  $c_{i,j}(\vec{r})$  are incoherent, as in disordered systems is often the case (see Chapter 5 for an example) these scattering spatial factors can be simply linearly combined with their relative offset being the contrast between the two relevant materials. This implies that a linear decomposition of these systems is possible into paired contrasts.

From this, we can determine a rule of thumb for scattering acquisition of complicated systems. To determine the structure of any one material in a system of  $m$  components, each pair should be measured, resulting in

$$N_m = \sum_{i=2}^m (i - 1) = \frac{1}{2}(m^2 - m) \quad (17)$$

Scattering measurements. So for a two-component system, one energy is needed, because there is only one combination, while for a three-component system, three energies should be measured to ensure that a given scattering pattern comes from a particular element. It should be noted that vacuum is always one of the components in every scattering experiment. Vacuum contrast should always be considered and removed from scattering patterns if material contrast is desired. For a ten-component system, there are 45 necessary energies, at which point complicated fitting routines will be needed to decompose each component. Rather than just taking the minimum number of measurements, taking a whole range of measurements at different energies can constrain scattering results and ensure that a certain measured structure

is from a particular material. Of course, in many experiments, multiple contrasts can be ruled out at once, i.e. scattering well below or above the absorption edge should maximize the vacuum contrast of all the materials in the sample at once, and minimize materials contrast. Careful NEXAFS measurements [137] and judicious use of multiple energies in every scattering experiment should become standard practice in using Resonant Soft X-ray Scattering.

In cases where  $n$  is not reducible to a scalar, but instead molecular alignment dramatically changes the optical properties, as are the case in many conjugated polymer systems [1, 79], each orientation (parallel, perpendicular to incident E-field) can be considered as different materials, increasing the number of scalar elements by one for uniaxial symmetric systems. (see Chapter 4 for a detailed derivation of scattering in these cases)

This technique of reducing scattering to pairs of materials at different energies, requires knowing the optical constants before experiment very accurately, which in many cases may be challenging or impossible. In these cases we propose that a principle value decomposition of an over-constraining set of energies can fit contrasts that are known, and return the residual scattering patterns, along with their individual contrasts, as accomplished successfully in our recent GRSOXS application (see Chapter 5). Such a complete model free analysis would require excellent normalization and background subtraction and the ability to measure absolute scattering intensities accurately, which are still challenging [79]. Nonetheless, the potentials of determining both chemical and structural information simultaneously in a single set of scattering experiments is an exciting possibility.

### 3.4 BEYOND BORN APPROXIMATION

There are concerns in organic thin films systems, specifically OPV systems, that the contrast enhancement at the carbon 1S absorption edge is so high, that the Born Approximation (BA) used with hard X-rays may no longer hold, and higher order forms may be necessary to accurately model the scattering as is done with techniques where multiple scattering events are possible [139]. This section will examine this claim for several realistic samples. First we will simulate commonly sized particles of PCBM in a P3HT matrix (or equivalently in the calculation, because of Babinet's Principle, P3HT domains in a PCBM matrix). Several studies have found domain sizes of ~20 nm - ~100 nm in this or similar systems [12, 140]. Next, the contrast peak of poly(styrene) (PS) is an example of a typical upper bound for organic materials, where  $|\delta|^2 + |\beta|^2 > 10^{-5}$  (Figure 3.1).

To test BA, we need a more precise theory to test it against. Although dynamical scattering theories are routinely used in many highly interacting probe systems, and are quite accurate, we consider the efficient and exact solution to the scattered field available using Mie scattering theory on dilute spherical dispersions [141]. While Mie scattering is not appropriate for high volume fraction systems like those we are considering, the change in form factor we can calculate with Mie scattering will indicate the limits of the BA in organic systems. This general limit will be equally applicable in high volume fraction experiments. At a minimum, by determining size scales and contrast levels at which Mie scattering no longer matches the BA, then those same size scales and contrast levels should be of concern in OPV thin film systems.

As we can see in Figure 3.2 and the results presented in Table 1, the scattering intensities even at the contrast peaks of the P3HT PCBM system are nearly identical between Mie Scattering and the BA. Only when we consider 300 nm particle radiuses at high contrast does Mie Scattering begin to significantly deviate. This (~300 nm) is generally the upper limit of sample thicknesses used in experiments, and simultaneously the maximum contrast usually

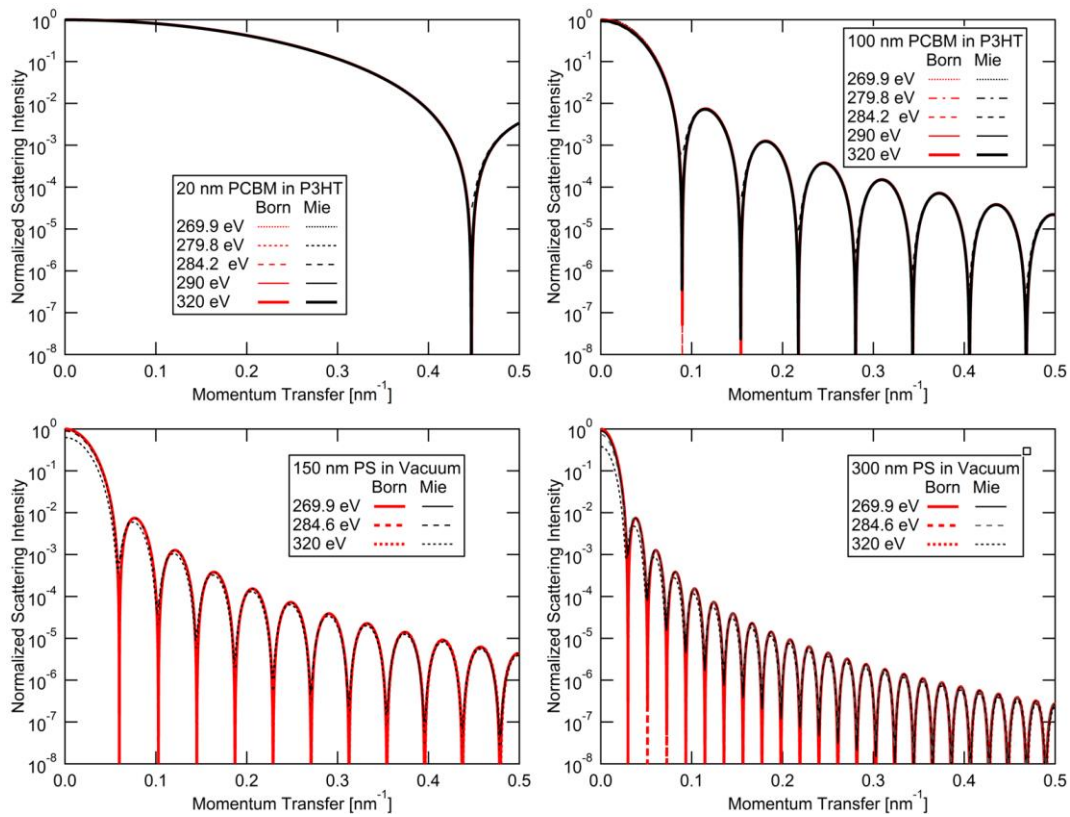


**Figure 3-2 Mie Scattering results**

BA compared to the exact Mie scattering solution for A) 20 nm and B) 100 nm radius PBCM particles in a P3HT Matrix, C) 150 nm and 2) 300 nm radius PS particles in vacuum. Each pair of scattering curves are normalized to the Born result at  $q=0$ , i.e. the Mie result is scaled by the same factor, thus when the Mie result at  $q=0$  deviates from 1, the results are no longer equivalent, and the Born Approximation is breaking down. This also means the contrast differences at different energies are normalized away.

**Table 1 Mie Scattering Results**

Material	radius (nm)	X-ray Energy (eV)	Ratio of Q	Ratio of Intensities
<b>PCBM in P3HT</b>	20	269.9	0.999	1.018
<b>PCBM in P3HT</b>	20	279.8	0.999	1.018
<b>PCBM in P3HT</b>	20	284.2	1.003	0.988
<b>PCBM in P3HT</b>	20	290.0	1.000	1.009
<b>PCBM in P3HT</b>	20	320.0	1.001	0.989
<b>PCBM in P3HT</b>	100	269.9	0.994	1.090
<b>PCBM in P3HT</b>	100	279.8	0.995	1.085
<b>PCBM in P3HT</b>	100	284.2	1.009	0.894
<b>PCBM in P3HT</b>	100	290.0	0.999	1.030
<b>PCBM in P3HT</b>	100	320.0	1.004	0.947
<b>PS in Vacuum</b>	150	269.9	1.002	0.959
<b>PS in Vacuum</b>	150	284.6	1.008	0.897
<b>PS in Vacuum</b>	150	320.0	1.030	0.626
<b>PS in Vacuum</b>	300	269.9	1.006	0.895
<b>PS in Vacuum</b>	300	284.6	1.021	0.737
<b>PS in Vacuum</b>	300	320.0	1.064	0.380

Data from fits to the data in Figure 3.2. Ratio of intensities are the Mie scattering intensities at  $q=0$  divided by the BA results. Ratio of Q is determined by the location of the first minimum from Mie Scattering divided by the first minimum found by BA.

achievable. While as discussed above, this result is not identically applicable to non-spherical or high volume fraction systems, a general rule seems to be that deviations in intensity are to be expected when either particle sizes or thicknesses are larger than  $\sim 300$  nm and the contrast of the system  $> 10^{-5}$ . Of course, there is a tradeoff between these measures. As the contrast goes down, thicker systems can be safely measured without multiple scattering events becoming a problem, and for thinner systems, somewhat higher contrasts should also be fine.

This appears to be the practical limits of BA, meaning that near these limits, multiple scattering events should be considered in the analysis. However, it should be noted that even in the worst cast considered, the measurable deviation in size scale measured is considerably

smaller , ~5%, than the deviation in intensity of ~60%. So when determining only size scales, and not total scattering intensity, multiple scattering events are less of a concern.

### 3.5 VOLUME FRACTION SIMULATIONS

A common characteristic of OPV Bulk Heterojunction systems is that they are composed of roughly equal fractions of two main compounds which have to some degree phase separated (by crystallization [49], agglomeration [142], or spinodal ripening [143]). Generally RSoXS measurement are used to determine the domain phase size, purity and interfacial characteristics [12, 82, 87, 89, 144]. Many models exist [145], but they can be difficult to fit, and if a fit is completed, it is often not straightforward to connect the parameters to characteristics of interest. A model free analysis is generally preferable if useful parameters can be extracted.

We conduct a statistical numerical analysis of common measures of domain size or spacing [1, 12, 77, 82, 87, 127, 136, 146, 147], including peak locations, zero crossings and minima of the autocorrelation, and various higher order derivatives corresponding to the Chord Length Distribution (presented in next section). We choose a simple system, one of randomly spaced cylinders with varying distributions, average size, distribution size, distribution type, and multiple distributions of different sizes, all at volume fractions from .1 to .7 of the system occupied. .We choose a dispersed system for the unambiguous knowledge of absolute length scales in the system, and while this limits the applicability of the results, comparisons to the values in spinodal decompositions and more ordered morphologies are straight forward and discussed below. In a sense, the dispersion case is a worst case scenario, as in these systems, there is still a form factor component which might complicate things, and lead to spurious

peaks in some analyses [96]. The results of correlation vs. volume fraction for all the measurable quantities described above from the scattering pattern, and all of the actual statistical information about the system are presented in Figure 3.3.

To mimic a real system, only  $q$  values from a reasonable collectable range of  $q$  values,  $.03$  to  $.5 \text{ nm}^{-1}$  were used in these simulations. The Lorentz corrected [97] intensity mean value is correlated to both domain size and domain spacing with the Pearson linearity coefficient of  $r > .995$  over the simulated volume fractions from  $.1$  to  $.7$ . It is important to note that certain simulated systems (described in Supporting Information) were only able to be calculated up to

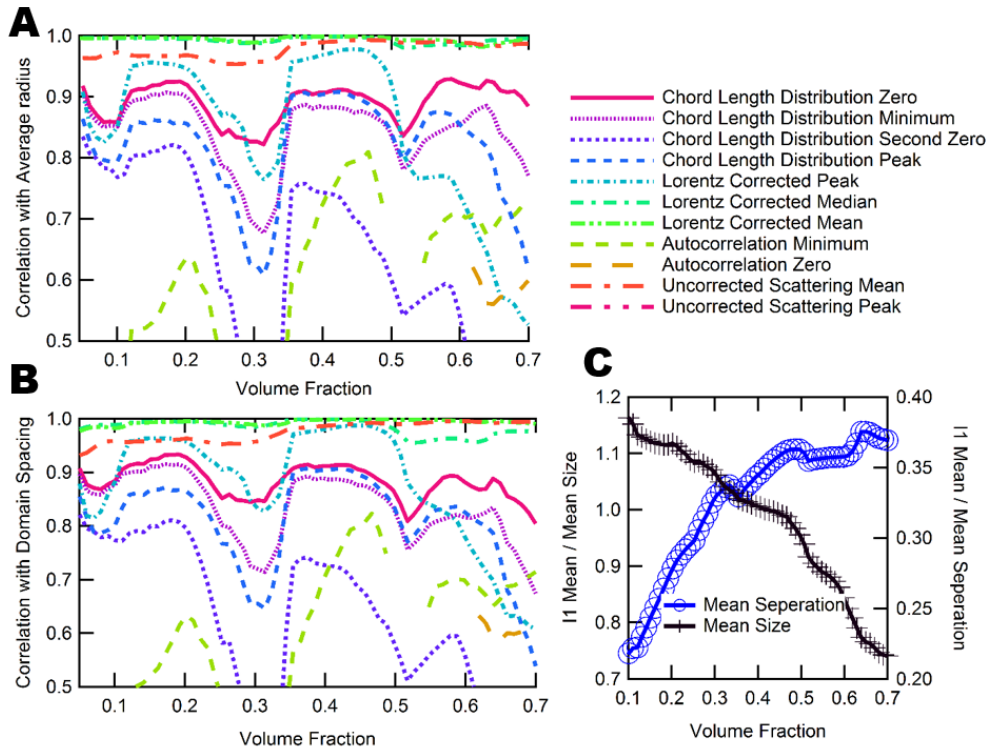


**Figure 3-3 Correlation of Scattering Measurables**

The correlations between measurables and the two basic ensemble properties of a system, A) the average radius of particles, and B) domain spacings. In both cases, the highest correlation is with the Lorentz corrected mean value. C) The linear coefficient between Lorentz corrected mean and domain spacing and mean size vs. volume fraction.

limited volume fractions, resulting in the periodic dips as these algorithms could no longer create higher volume fraction systems. These systems allow each cylinder to have an exclusion zone some percentage of the radius extending beyond the surface, where other cylinders could not be added. Despite all these variations, the Lorentz corrected mean is always a reliable method to determine these average system properties.

### 3.6 CHORD LENGTH ANALYSIS

Despite its obvious use in characterizing the average properties of a system, the mean domain size and domain spacing are only rough averages of the whole system. It is often important to look for details of the system, particularly important is recognizing multiple size scales in a single system [127]. Figure 3.4 presents one of the many systems contributing to

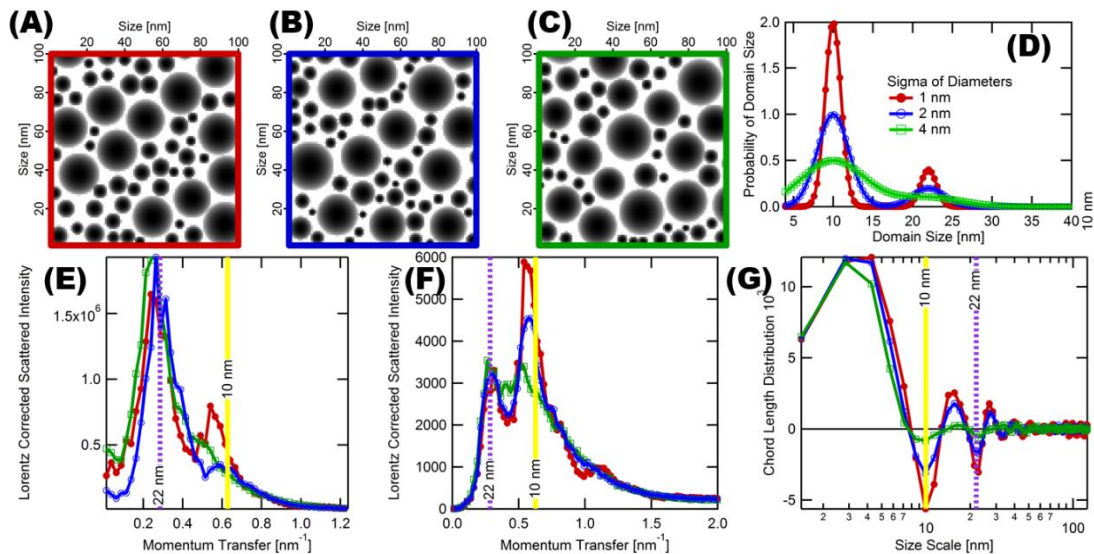


**Figure 3-4 Chord Length Analysis**

Figure showing selection of systems of cylindroids with populations of 10 nm and 22 nm diameters, with sigma of A) 1 nm B) 2 nm C) 4 nm. D) The probability density functions diameters of spheres were chosen from. E) The uncorrected scattering and F) Lorentz corrected scattering curves from these systems with locations of 10 and 22 nm marked on the frequency axis. G) The Chord Length Distribution, with the diameters marked.

Figure 3.3, a bimodal system with average diameters of 5 nm and 11 nm. The different scattering curves and the locations of the radiuses of the two dominant species of domains that are present in the system. As can be seen in Figure 3.4, each way of viewing scattering from the sample can be used to obtain rough ideas of the population densities of different size scales in the system, however as polydispersity is increased, the chord length analysis remains the most reliable method of reconstructing something approaching the true density function.

The Chord Length Distribution (CLD) is defined as

$$CLD(x) \equiv \frac{d^2}{dx^2} \left( \int_0^\infty dq I_1(q) e^{-i q \cdot x} \right) \quad (18)$$

Which has been shown [97] to be equivalent to

$$CLD(x) = \sum_{i=1}^{\infty} (l_{2i-1}(x) - l_{2i}(x)) \quad (19)$$

Where  $l_i(x)$  is the probability of starting at an interface and traveling through  $i-1$  interfaces before ending on another interface. It is a combination of both phases, and so in high volume fraction experiments it is helpful to model  $l_1(x)$  first from a test morphology. Also, this means that the peaks are not readily turned into domain sizes for complex systems. Importantly, this measure  $l_1(x)$  is exactly the fundamental exciton diffusion length. This is exactly applicable to the measure of the linear distance an exciton or free charge has to move before hitting another interface, at least in a straight line.

To test the application of equation (18), we simulate a symmetric system, created by the often used and efficient Cahn-Hilliard approach [148-151]. In this system, each material is structurally identical, so concerns about the different chord length distributions for the two different materials are not relevant. We obtain  $l_1(x)$  by tracing random trajectories through the

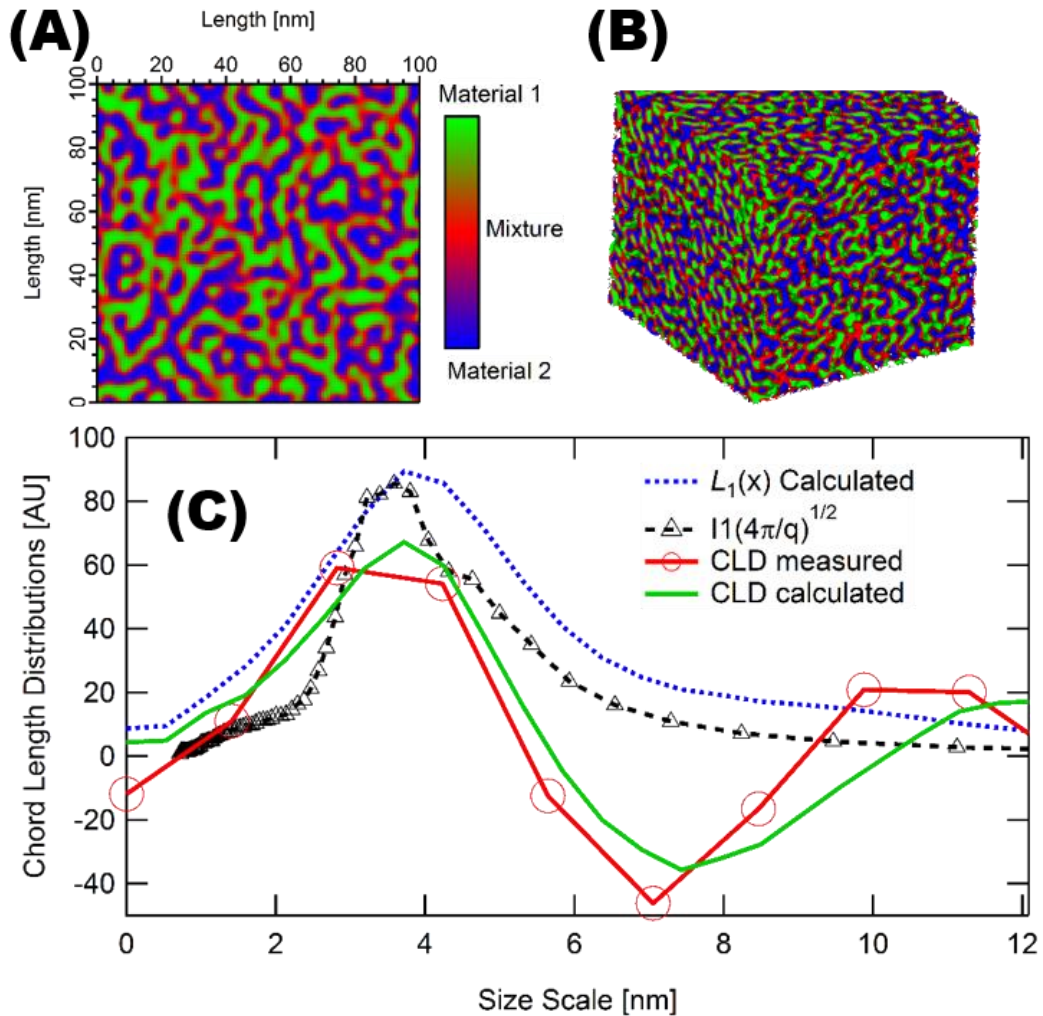


**Figure 3-5 Chord Length in Symmetric System**

A) A two dimensional slice of the 3D spinodal decomposition. B) 3D isosurface of the same spinodal decomposition. C) The calculated first chord length distribution  $l_1(x)$  along with the calculated full CLD, and the square root of Lorentz corrected scattering pattern  $I_1(q)$  adjusted to real space and corrected for 50% volume fraction to give the domain size, along with the “measured” CLD calculated from  $I_1(q)$ .

three dimensional space, histogramming the distances between crossings of 50% contours. In this system, having no long range order and symmetric between phases.  $l_n(x) = l_1\left(\frac{x}{n}\right)$ . Thus we can calculate an effective CLD by summing sufficient (in this case 20) terms in equation (18). Comparing this result to the CLD calculated through the scattering simulation by equation (17), we get very good agreement, giving credence to the link between (17) and (18) and indicating that this is an important morphological characterization which is currently infrequently used even when apropos to the very measurement often desired.

### 3.7 CONCLUSIONS

Starting from basic scattering theory, we have shown the benefits of soft X-ray scattering on high volume fraction systems. We have derived the contrast function and showed that in the soft X-ray region, materials contrast can exceed vacuum contrast. We have tested and found practical limits of the Born Approximation in simplified systems, giving credence that this approach is correct. Using the Born approximation, Lorentz correction, and the CLD obtainable through derivatives of the auto correlation function, we show that statistically we can have very reliable correlation between the mean of the Lorentz scattering intensity and domain spacings and domain sizes. For more complicated systems, we delved into the CLD, comparing the information readily available from raw scattering, Lorentz corrected scattering, and the CLD, for determining populations of scatterers. Finally, we confirm the property of CLDs revealing the often critical information about the distances between interfaces. We hope that this work will aid the community in interpreting and presenting scattering data, and determining critical device-critical morphological characteristics.

### 3.8 SUPPLEMENTAL INFORMATION

The morphologies created to compare in figure 3.3 were based on the following table of sample morphologies. Scattering patterns were simulated for each system at every volume fraction until the system failed to add any more cylinders. As it became impossible to add larger cylinders, the distribution of radii in the system became skewed towards smaller radii, but at every step, the actual mean domain size and spacing was calculated from the actual cylinders in the system, not the distribution by which the radiuses were picked, so this skewing did not influence the final correlation. Each distribution was calculated three times, with exclusion zones of 1.1, 1.4, and 1.7 times the diameter. This disallowed future cylinders from being placed that distance from the each cylinder, forcing well-spaced cylinders. These

**Table 2 Volume Fraction Systems**

<b>Population 1</b>			<b>Population 2</b>			<b>Ratio of Populations</b>
<b>Type</b>	<b>Center</b>	<b>Width</b>	<b>Type</b>	<b>Center</b>	<b>Width</b>	
Gaussian	8	0.1				
Gaussian	8	0.5				
Gaussian	8	2				
Gaussian	3	0.5				
Gaussian	5	0.5				
Gaussian	12	0.5				
Lognormal	8	0.1				
Lognormal	8	0.5				
Lognormal	8	2				
Lognormal	3	0.5				
Lognormal	5	0.5				
Lognormal	12	0.5				
Gaussian	5	0.1	Gaussian	11	0.1	1
Gaussian	5	0.5	Gaussian	11	0.2	1
Gaussian	5	0.5	Gaussian	11	0.5	1
Gaussian	5	1	Gaussian	11	1	1
Gaussian	5	2	Gaussian	11	2	1
Gaussian	5	1	Gaussian	11	1	2
Gaussian	5	1	Gaussian	11	1	5
Gaussian	5	1	Gaussian	11	1	0.5
Gaussian	5	1	Gaussian	11	1	0.2

All of the systems simulated to produce Figure 3.3. The above the parameters of the probability distribution from which cylinders were added to the system. Centers and widths refer to the center and sigma (or log sigma) of the distribution in radius.

populations with extra excluded area could not reach the higher volume fractions, and so these resulted in the non monotonic deviations vs. volume fraction in all the fit parameters in figure 3.4.

## *Chapter 4*

### **A MODEL FOR SYMMETRY BREAKING AT INTERNAL HETEROINTERFACES EXPLAINS ANISOTROPIC RESONANT X-RAY SCATTERING FROM ISOTROPIC ORGANIC SYSTEMS**

This chapter is a prepared manuscript on the first systematic theory to explain anisotropic scattering which changes with the polarization of the incident x-rays from isotropically created samples. In January 2011, I collected the initial anisotropic scattering pattern which led to our 2012 Nature Materials paper. In that paper, we proposed that the scattering might come from interface alignment, but we showed no rigorous theory of how that scattering signal could come about. Since then, I have been working on the theoretical backing which has resulted in this paper. Brian Collins collected and calculated the anisotropic optical constants which were needed for the calculations. John Tumbleston and Harald Ade helped with the conception of this project. Maolong Tang wrote the basic Lattice Boltzmann simulation code that was used in the creation of that particular morphology. Finally Subhrangsu Mukherjee calculated the aligned optical constants from DFT for comparison to those calculated from experiment by Brian Collins. I designed and wrote the scattering simulation, the alignment Monte Carlo, and the morphology creation codes, and conceived of all of the systems to be presented and compared in this paper.

# A Model for Symmetry Breaking at Internal Heterointerfaces Explains Anisotropic Resonant X-ray Scattering From Isotropic Organic Systems

Eliot Gann<sup>1</sup>, Brian Collins<sup>2</sup>, John R. Tumbleston<sup>1</sup>, Subhrangsu Mukherjee<sup>1</sup>, Maolong Tang<sup>1</sup>, Harald Ade<sup>1</sup>

<sup>1</sup> Department of Physics, NCSU, Raleigh, NC 27695-8202

<sup>2</sup> Electronic Materials Group, NIST, Gaithersburg, MD 20899-1070

## 4.1 ABSTRACT:

Several thin film systems consisting of spincoated all-polymer and polymer-fullerene blends have been observed recently to have anisotropic scattering when probed near the carbon 1S absorption edge with polarized soft X-ray scattering. This anisotropy in otherwise isotropic samples must require a breaking of isotropic symmetry, but no model for the required local symmetry breaking has been explored. We investigate how the uniaxial optical and organizational properties of conjugated polymer samples can produce this scattering anisotropy. We simulate four binary, thin film systems with near equal volume fraction of components: spheres in a matrix, cylinders in a matrix, spinodal decomposition of two materials, and a fibril-type network. Using a combination of techniques to generate these disordered morphologies, we use a Monte Carlo relaxation algorithm to propagate alignment from the interfaces into the bulk of one of the materials. Then using uniaxial optical constants of the polymer poly(3-hexylthiophene) (P3HT) and the radially symmetric optical constants of

the small molecule C60 based fullerene [6,6]-phenyl-C61 -butyric acid methyl ester (PCBM), we simulate the anisotropic scattering intensities. We compare the results in several forms both two and single dimensional cuts, revealing a rich new measurable parameter which allows for new details of the interface alignment, molecular orientation, and morphology to be measured.

## 4.2 INTRODUCTION

It has been reported recently [1, 79, 144] that a globally isotropic mixture of polymers when spun cast, can produce an anisotropic scattering signal when probed by polarized X-rays at certain energies. Rather than a more common symmetry breaking produced by an external angular dependent source including substrate templates, surface energy effects at the substrate or free surface, or a unidirectional application or processing technique, this observed anisotropy changes depending on the electric field polarization of incident resonant X-rays. Thus, it was proposed that the breaking of symmetry must be from molecular alignment, templated by otherwise isotropic morphological features. Interfaces between separated phases are a natural source of the necessary symmetry breaking [1, 144]. Another view is that fibril morphology accounts for anisotropy. We will examine these two possibilities as well as showing random molecular alignment without morphological templating does not lead to anisotropic scattering. In the same way that second harmonic generation [152] can ensure interface sensitivity because that is the location of symmetry breaking, we develop criteria to recognize anisotropy driven from interfacial interactions from that produced in the bulk. We will show that by analyzing the anisotropic signal, we can distinguish between these sources, and learn details about the structure at the interface.

The difference between anisotropic and non-anisotropic signal may even solve the problem posed by Babinet's principle, i.e. to identify which material is in the dispersed and which is in the matrix phase in an asymmetric structure [153]. However, until now, there has been no effort at modeling the mesoscale structure of these systems to link the measured anisotropic signal to morphology quantitatively. For these devices, interfacial alignment is likely critical to device performance due to anisotropic charge transport and molecular orbitals [154]. So a quantitative theory of the nanostructure that leads to anisotropic scattering, if indeed indicating average molecular alignment near material interfaces, is important to both quantify system morphology, and improve system performance.

This paper presents and compares several methods of simulating and analyzing scatter from aligned systems. Our model is a combination of two procedures, first generating morphologies of material compositions through various methods, followed by a Monte Carlo relaxation algorithm which propagates alignment from the interface into the bulk of one of the components. Conjugated polymers, like those studied in this work, are uniaxially anisotropic largely both in their spectroscopic properties [155, 156] in the x-ray regime and in their organizational packing [157]. Because of this concurrence, the morphology as influenced by packing, likely correlates with refractive properties. We simplify the full tensor form of the statistical alignment and thus refractive index to a vector representing the preferential alignment ( $\vec{s}$ ), and a scalar representing the relative material composition at that point ( $\Phi$ ). The axis of these uniaxial polymers when coarse grained is defined by the carbon core 1S to pi\* orbital transition dipole moment (TDM). These molecules also commonly stack in this direction, called  $\pi$ - $\pi$  stacking. The direction of the TDM is called the "face" of the molecule,

so when the TDM is aligned towards a direction of interest (i.e. an interface or surface), it is said to be “face-on” whereas all other orientations are “edge-on”. The terminology is useful, however, hereafter in this work, if not specified it is understood that the polymer is oriented face-on or edge-on with respect to the internal material-material heterointerface, not to either the film-substrate or film-air surface, as these terms may be commonly used.

The materials used in these simulations are P3HT and PCBM, because this system is widely used [80] and both components are well studied. Although the specific simulations here presented here are limited to systems composed of these commonplace materials, the general richness of anisotropic behavior should be expected with any polymer system that forms similar morphologies, and the methods presented will apply equally well to complex systems when multiple components each have their own alignment behavior.

### 4.3 MORPHOLOGY MODELING

As discussed above, our model coarse-grains the polymer mixture onto a lattice of relative material composition and preferential molecular alignment. Each point in space is characterized by a scalar ( $\Phi_i$ ) for each material  $i$  representing relative composition and a vector ( $\vec{s}_i$ ) representing the preferential statistical alignment of the transition dipole moments of that material. The total composition  $\Phi = \sum \Phi_i \cong 1$  and  $\Phi_i$  and  $|\vec{s}_i|$  are constrained to be less than 1 and positive.  $\vec{s}_i$  is a director field because of the symmetry of the dipole moment, so that  $\vec{s}_i = -\vec{s}_i$ . Morphologies are completely determined by  $\Phi_i(\vec{r})$ , and are calculated by a number of methods described below. Alignment maps  $\vec{s}_i$  are calculated subsequently by a Monte Carlo method, except for the fibril morphology, in which both morphology and alignment are created in the same step.

We pick several common morphologies in this study. All are modeled in three dimensions in a thin film morphology, on grids with dimensions of 2,560 nm X 2,560 nm x (80, 120, 160 or 240) nm. The voxel size is 5 nm meaning the number of grid points is 512 x 512 x (16, 24, 32 or 64) voxels. This simulation size is adequate to model the real resolution and coherence limit of soft x-ray scattering beamlines [79] on realistically scaled thin films. X-rays will be simulated with the incoming  $\vec{k}$  perpendicular to the thickness of the film, modeled on the usual arrangement for thin film P-SoXS experiments. [1]

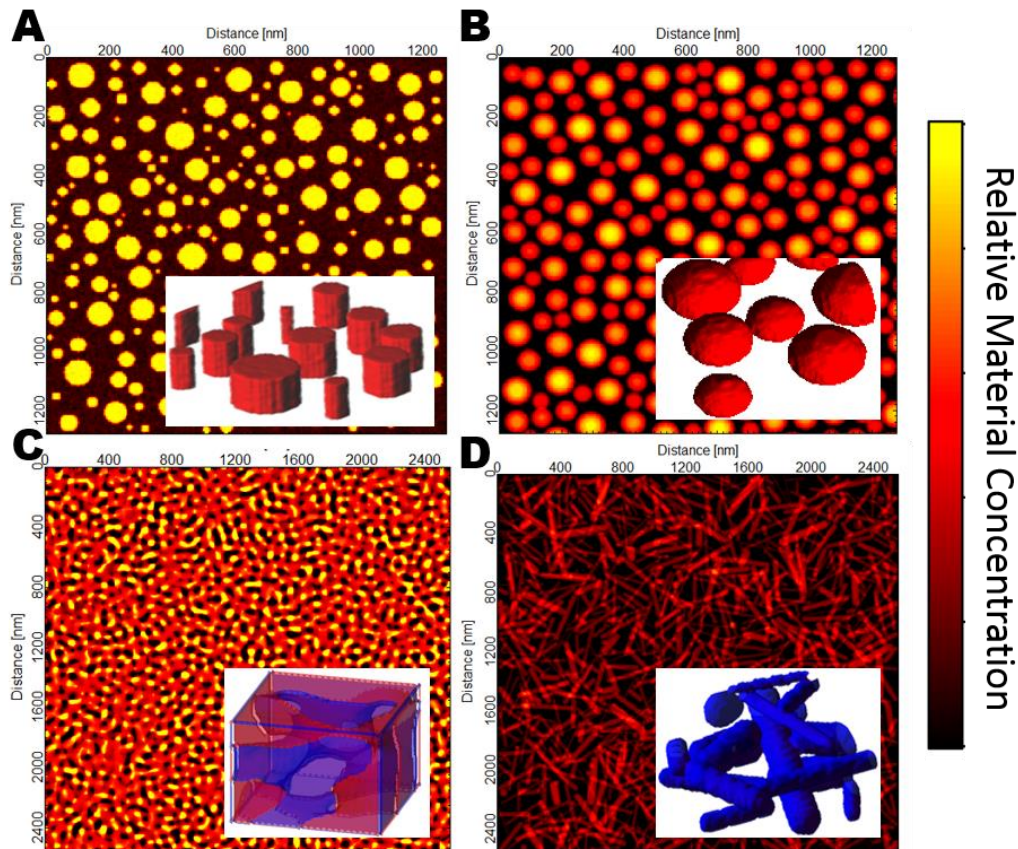


#### Figure 4-1 Morphologies

Figure 1 Averages of the relative material composition along the path of the X-rays for the four thin film morphologies: A) Cylinders aligned with the path of X-rays B) Spheres C) a Spinodal demixed blend and D) fibrils, which are modeled as cylinders generally aligned in the plane of the thin film. Inset are 3D renderings of the composition.

First we create a three dimensional system of cylinders (Figure 4.1A). The cylinders are placed randomly on the a 2D grid perpendicular to film thickness. Each cylinder radius is chosen from a log normal distribution with a center at 25 nm and width of 10 nm. Placement of each cylinder is constrained to not overlap with previous cylinders with an exclusion zone of 10% of the radius. Cylinders were continually placed until 30% of the volume consisted of cylinder dispersions. This morphology, depicted in figure 4.1 is consistent with thin-film systems where two-dimensional real space techniques reveal circular domains [12] which may extend through the thickness of the device. We next create a system of random spherical dispersions by sequentially adding non-overlapping spheres, with radius chosen from a log normal distribution, to a 3D system until 30% volume fraction is achieved, depicted in Figure 4.1B. The width of the log normal distribution of radiuses for spheres is 5 nm, compared with 10 nm for the cylinders, which makes the volume distributions of the two systems more comparable. Next, we create a bicontinuous or symmetric materials phase (Figure 4.1C) by use of a Lattice Boltzmann method (LBM). LBM was developed from lattice gas automata [158] overcoming some defects in that earlier method. LBM is commonly used to accurately calculate computational fluid dynamics. The governing equation of CFD, Navier-Stokes, can be completely recovered by LBM [159, 160]. It has also been proven that LBM can be directly derived from the Boltzmann equation [161], providing a robust physics foundation. Interactions between multiple components and phases with different properties can be accurately and efficiently calculated [162-164], so LBM is an ideal method for spinodal decomposition [165]. Finally, we model a fibril-like network of polymer crystallites. It is well known that the fibril axis is along the  $\pi^*$  transition dipole moment of the polymers [36, 166].

Thus, the system consists of largely in-plane cylinders, as depicted in Figure 4.1D. As only a portion of the material is known to crystallize, the matrix phase is a mixture of amorphous polymers and fullerene [21, 23, 34, 167-169]. The system as a whole is constrained to have a 50% volume fraction. Each of these systems described are depicted in thin film projection and (inset) three-dimensional representation in Figure 4.1.

#### 4.4 CALCULATING OPTICAL CONSTANTS

Anisotropic optical constants are calculated from absorption spectroscopy of pure components. Optical constants from perfectly aligned materials cannot be experimentally collected for these largely disordered materials, but rather must be extrapolated from experimentally collected spectra. First absorption spectra are collected at the “magic” angle of  $54.7^\circ$  from the normal to a spincoated thin film. This angle is where contributions between any in-plane or out-of-plane preferential alignments are balanced, so that, as long as there is no other preferential alignment direction, the faces of the molecules are on average 1/3 aligned with the electric field and 2/3 are unaligned. This magic angle measurement is thus a measure of the perfectly isotropic molecule. This assumption is typically valid in spincoated systems, where the only preferential direction is normal to the surface, and so any macro scale preferential alignment must be either along or perpendicular to this direction.

At normal incidence, the spectroscopic signal changes significantly, particularly at the P3HT C1S to  $\pi^*$  TDM peak near 285 eV. Although we have no knowledge of the absolute fraction of face-on molecules that are aligned along the polarization vector at this orientation, all that is required is that we can quantify the difference between the normal-incidence signal and the unaligned, magic angle signal. Using this difference, we linearly extrapolate from the

isotropic spectra until the  $\pi^*$  peak is very close to completely gone, i.e. When the TDM has no overlap with  $\vec{E}$ . This linear extrapolation is valid in the case of uniaxial symmetry and roughly flat conjugation present in these conjugated systems [155, 156].

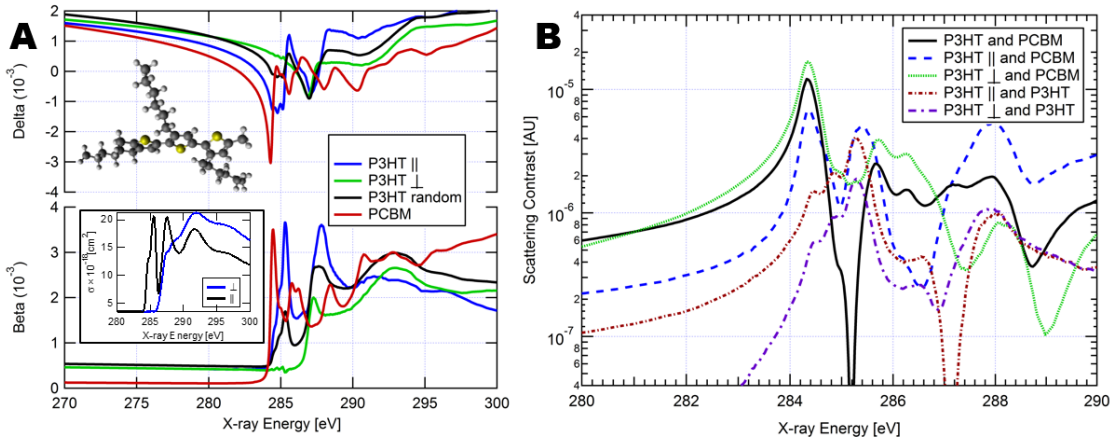


**Figure 4-2 Optical Constants and Contrasts**

Figure 2 A) Optical constants, the real part ( $\delta$ ), and the imaginary part ( $\beta$ ) of the index of refraction ( $n = 1 - \delta + i\beta$ ), measured and calculated at different angles relative to the polarization axis of incident X-rays. Inset is calculation of parallel and perpendicular  $\beta$  for comparison and a drawing of the P3HT molecule B) Scattering contrasts calculated between different components in a P3HT PCBM film with molecular alignment of P3HT.

This set of optical constants, with the  $\pi^*$  peak reduced to nearly zero, we call the perpendicular optical constants or  $(\delta_{\perp i}(\lambda), \beta_{\perp i}(\lambda))$  because the  $\pi^*$  dipole moment is as close as possible to perpendicular to  $\vec{E}$ . Comparing these optical constants with the magic angle optical constants we extrapolate back in the opposite direction twice the factor that was needed to remove the  $\pi^*$  peak, and obtain the 100% aligned optical constants  $(\delta_{\parallel i}(\lambda), \beta_{\parallel i}(\lambda))$ . All of these optical constants are shown in Figure 4.2.

#### 4.4.1 CALCULATING OPTICAL CONSTANTS FROM DFT

We confirm the validity of these results by comparing them with simulated optical constants obtained by density functional theory (DFT), shown in Figure 4.2A inset. The equilibrium geometry for P3HT was determined by molecular mechanics using a universal force field [170]. The X-ray absorption spectra (C and N 1s) of the molecule were calculated by DFT with the computer code StoBe [171]. For the purpose of our calculations, we used all-electron triple- $\zeta$  valence plus polarization (TZVP) atomic Gaussian basis sets for carbon and sulfur centers, while the hydrogen basis sets were chosen to be of the (311/1) type [172]. To calculate x-ray absorption spectra, the Slater transition state method was applied [173]. In this case the optimized geometry obtained from the geometry optimization calculation was kept fixed and polarization and angle dependent absorption spectra were calculated. In order to obtain an improved representation of relaxation effects in the inner orbitals, the ionized center was described by using the IGLO-III basis [174]. A diffuse even-tempered augmentation basis set was finally included at the excitation center to account for transitions to unbound resonances. The absorption spectra were generated through a Gaussian convolution of the discrete spectra with varying broadenings.

Having these optical constants, we can calculate the respective binary contrasts between each of the potential components in the thin film, shown in Figure 4.2B. These will be useful in understanding the anisotropic scattering signals in the following sections.

#### 4.5 CALCULATING ALIGNMENT DENSITY

A Monte Carlo method propagates alignment from the interfaces into the material. The spatial gradient of composition is used to determine the interfaces in the system. We define an

energy cost to be differently aligned from this gradient, a cost to be differently aligned from nearest neighbors, and an entropic energy cost of having any preferential alignment. Creating an initial grid of very small random preferential alignment vectors for all points in space, the algorithm calculates the total energy of the configuration. A metropolis test applied to each alignment location to evolve the system forward. The Monte Carlo proceeds through the system, and after approximately 200 steps / grid location, an energy minimum can be reached. This results in a preferential alignment field  $\vec{s}_i(\vec{r})$  (Figure 4.3A).

#### 4.6 SCATTERING SIMULATION

Scattering simulation is done by first turning the scalar material composition field and vector preferential alignment field  $(\Phi_i(\vec{r}), \vec{s}_i(\vec{r}))$  created by the model into an index of refraction map  $n(\vec{r}, \lambda, \vec{E})$  at each X-ray incident energy and polarization  $\vec{E}$  (depicted in Figure 4.3B). First the composition of each element that is parallel  $\vec{E}$  ( $\Phi_{\parallel i}(\vec{r})$ ) is found

$$\Phi_{\parallel i}(\vec{r}) = \Phi_i(\vec{r}) \left( \vec{s}_i(\vec{r}) \cdot \vec{E} + \frac{1}{3} (\Phi_i(\vec{r}) - |\vec{s}_i(\vec{r})|) \right) \quad (1)$$

The second term in (1) comes from the amount of material randomly aligned in any given direction within the unaligned portion of the material. For example in a system with no preferential alignment (i.e.  $\vec{s}_i(\vec{r}) = 0$ ) one third of the transition dipole moments are aligned with  $\vec{E}$  regardless of its direction and at the other extreme, a system perfectly aligned in any direction, this second term is zero as  $|\vec{s}_i(\vec{r})| = \Phi_i(\vec{r})$ .

The remaining population of molecules whose TDMs are not aligned with the polarization vector are calculated

$$\Phi_{\perp i}(\vec{r}) = \Phi_i(\vec{r}) - \Phi_{\parallel i}(\vec{r}) \quad (2)$$

And the effective index of refraction map for each point on the grid and for each wavelength ( $\lambda$ ) is calculated

$$n(\vec{r}, \lambda, \hat{E}) = 1 - \sum_i \Phi_{\parallel i}(\vec{r})(\delta_{\parallel i}(\lambda) - i\beta_{\parallel i}(\lambda)) + \Phi_{\perp i}(\vec{r})(\delta_{\perp i}(\lambda) - i\beta_{\perp i}(\lambda)) \quad (3)$$

The 3D index of refraction map (the imaginary part of which is depicted in Figure 4.3C) is then transformed into spatial frequency ( $q$ ) or Fourier space by the Born approximation. Depicted in the inset of Figure 4.1A.

$$I(\vec{q}, \lambda, \hat{E}) \propto \left| \int n(\vec{r}, \lambda, \hat{E}) e^{i\vec{q} \cdot \vec{r}} d\vec{r} \right|^2 \quad (4)$$

This produces the full three dimensional  $q$ -space representation of possible scattering. The experimental x-rays are modeled to be along the axis perpendicular to the film, which we define as the x axis. Thus the wave vector if the incoming X-ray beam  $\vec{k}$  is.

$$\vec{k}_{in} = \frac{2\pi}{\lambda} \hat{x} \quad (5)$$

The Ewald sphere construction intersects  $\vec{q}$ -space at the origin. The surface of the sphere in  $\vec{q}$  space measures the Intensity of each point that matches

$$\vec{k}_{out} = \vec{k}_{in} + \vec{q} \quad (6)$$

With the condition of elastic scattering being

$$k \equiv |\vec{k}_{in}| = |\vec{k}_{out}| \quad (7)$$

Thus, the elastic scatter forces the condition

$$q_x = k - \sqrt{k^2 - q_y^2 - q_z^2} \quad (8)$$

So the intensity measured at a pixel location corresponding to a  $q_y$  and  $q_z$  (a  $q_x$  and  $q_y$  grid is shown in the Figure 4.2D) measures

$$I(q_y, q_z, \lambda, \hat{E}) = I\left(k - \sqrt{q_y^2 + q_z^2} - k^2, q_y, q_z, \lambda, \hat{E}\right) \quad (9)$$

#### 4.7 TWO DIMENSIONAL SCATTERING PATTERNS

Using (9), we simulate a two dimensional scatter pattern as measured by the experiment, shown below in Figure 4.3 for the spheres with thin face-on alignment in the matrix phase, along with a 3D representation of a portion of the sample showing visually equation (1) and the results of equation (9). The scattering intensities are splotchy because this treatment mimics a perfectly coherent beam, meaning the scattering pattern is speckled [175].

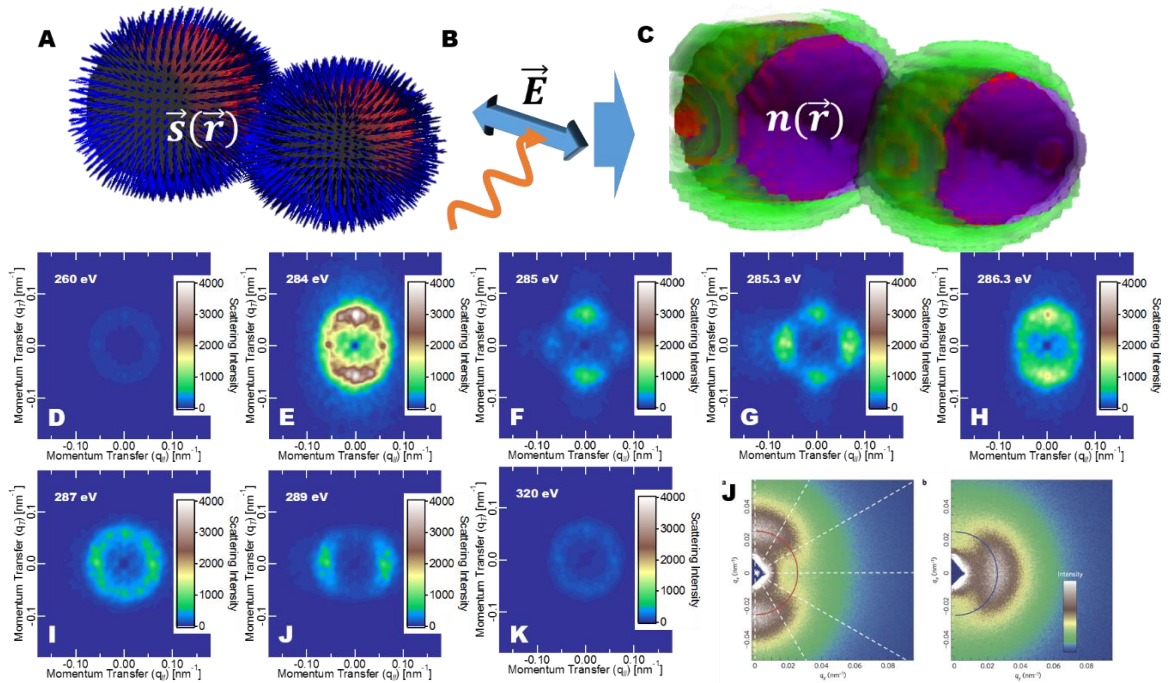


**Figure 4-3 Scattering Patterns**

Figure 3 A) a 3D director plot of  $\vec{s}(\vec{r})$  in P3HT surrounding red isosurface of P3HT domains. B) a schematic of the electric field of the incoming X-ray beam which with  $\vec{s}(\vec{r})$  from equation (1) can be used to calculate C)  $n(\vec{r})$  (the imaginary part of  $n$  is shown as semitransparent isosurfaces surrounding the same PCBM domains as pictures in A. Green isosurfaces are higher  $\beta$  while purple isosurfaces are lower  $\beta$  than the surrounding P3HT medium. D-K) are two dimensional scatter plots calculated from  $n(\vec{r})$  and equation (4) and (9). The electric field is horizontal in all cases. J) a reproduction of Figure 4 from a publication by Collins et al. in Nature Materials 2012 [1] for comparison to the simulated scattering patterns.

Much of the speckle has been removed from the displayed data by applying a Gaussian filter with sigma of  $.01 \text{ nm}^{-1}$  to the 2D pattern. A beamstop is simulated to block the scatter at  $|\vec{q}| < .01$ , which is a conservative estimate of the amount of scatter obtainable in a single exposure [79].

Comparisons between the patterns (Figure 4.3) and the contrasts (Figure 4.2) reveal the sources of anisotropy. In all simulations,  $\vec{E}$  is horizontal. At 260 and 320 eV all contrasts are low, but particularly the contrasts between the different alignments of P3HT reduce faster than the contrast between any of the P3HT (aligned or not) and PCBM. 284 eV has the maximal contrast between PCBM and all alignments of P3HT, and accordingly, the scattering both parallel and perpendicular to the electric field is the highest at this energy, although the perpendicular alignment contrast and scattering is higher than parallel. At 285 eV, an previously unreported phenomenon is observed. At this energy, contrast between unaligned P3HT and PCBM goes to zero, leaving only the contrasts involving the aligned portions of P3HT to contribute to scattering. Here, although the contrasts are similar in magnitude, they are not in the same direction. The imaginary parts of the indices of refraction both have large differences at this energy, but in the opposite direction from PCBM. This results in the material aligned parallel with the beam and the material aligned perpendicular are highly scattering, but the material in between the two has low contrast with both the PCBM dispersion and unaligned P3HT core. This results in almost four-fold symmetric pattern in the scattering map, rather than the usual two-fold symmetry at other energies. At 289 eV there is only one major contrast in the system, between parallel P3HT and PCBM, and this produces the cleanest anisotropic signal, (and the maximum of anisotropic signal as shown in Figures 4.7 and 4.8 below).

Comparing these results to the previously published experimental results [1] is possible, although only qualitatively. The system in question was composed of different materials, with different NEXAFS spectra than the system modeled, and so particular energy dependence of features we see here are not applicable. So while an energy to energy comparison of the simulation and previous result cannot be accomplished, qualitative comparison of the scattering patterns is possible. The scattering pattern from the experiment most closely resembles the simulated scattering pattern at 284 eV so it is likely that a similar index of refraction distribution produced both patterns.

We can create a few rules of thumb from this simulation. When compositional contrasts between all elements are high, a scattering pattern similar to 284 eV is expected. If a single orientation has much higher contrast with the other material than other combinations, then a scattering pattern similar to 289 eV should be expected. When both anisotropic contrasts are large and in the opposite direction of each other, then we expect to observe a four-fold symmetric pattern similar to 285 eV.

## 4.8 AZIMUTHAL SYMMETRIES

To explore the azimuthal symmetries in depth not easily seen in the 2D scattering patterns, particularly to distinguish between morphologies and different types of alignments, we present azimuthal plots of intensity vs. radial momentum transfer. Figure 4.4 shows face-on alignment and Figure 4.5, edge-on alignment, at the same energies discussed above, 284 eV, 285.1 eV, and 289 eV for spinodal and spherical systems.

There are several interesting trends to note from reducing the full two dimensional data sets in this way. It should be noted that each of these scattering patterns in an experiment will likely be in combination coherently or incoherently with other sources of scatter including mass thickness variations, which will add essentially a constant flat (isotropic) background when plotted as in Figures 4.4 and 4.5. Thus the lower intensity anisotropic features are likely

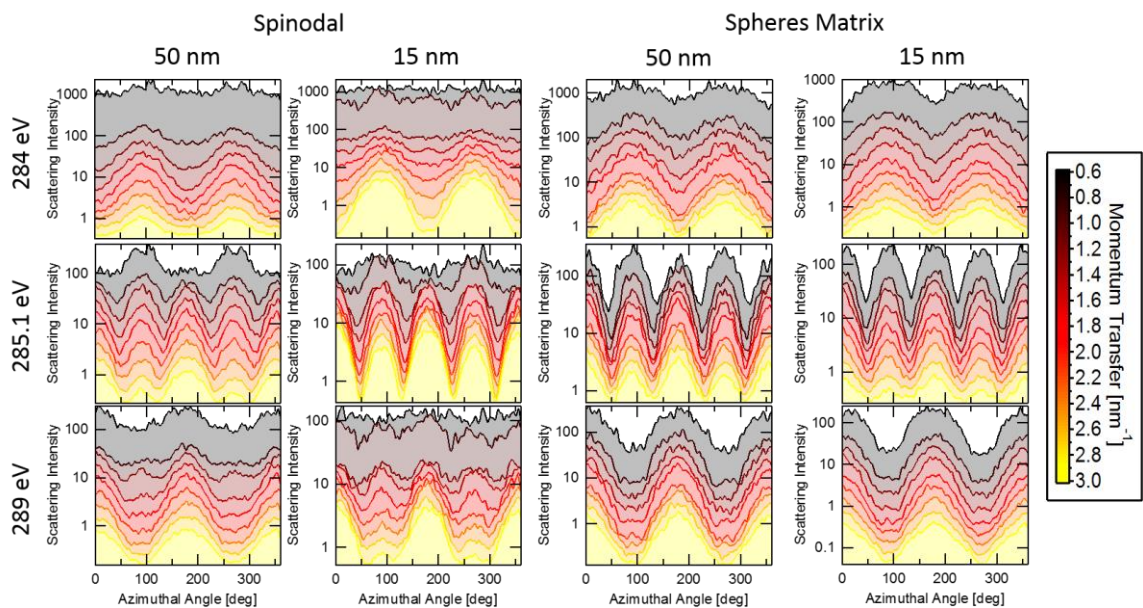


**Figure 4-4 Scattering vs. Azimuth Angle – Face-on**

Figure 4 Lorentz-corrected scattering vs. azimuth angle at different momentum transfers for Face on alignment. Graphs in the same columns are of the sample labeled above the column, from left to right, spinodal decomposition with alignment extending 50 nm from the interface, spinodal decomposition with alignment extending 15nm from the interface, Spheres with alignment extending 15nm from the interface, and spheres with alignment extending 15nm from the interface. Rows are at (from top to bottom) 284 eV, 285.1eV, and 289 eV. Azimuthal angle is relative to the incident X-ray E-Field.

to be difficult to measure. All plots have the y axis logarithmically scaled, so nearly sinusoidal signals (such as fibrils at 284 eV) may not appear sinusoidal by eye.

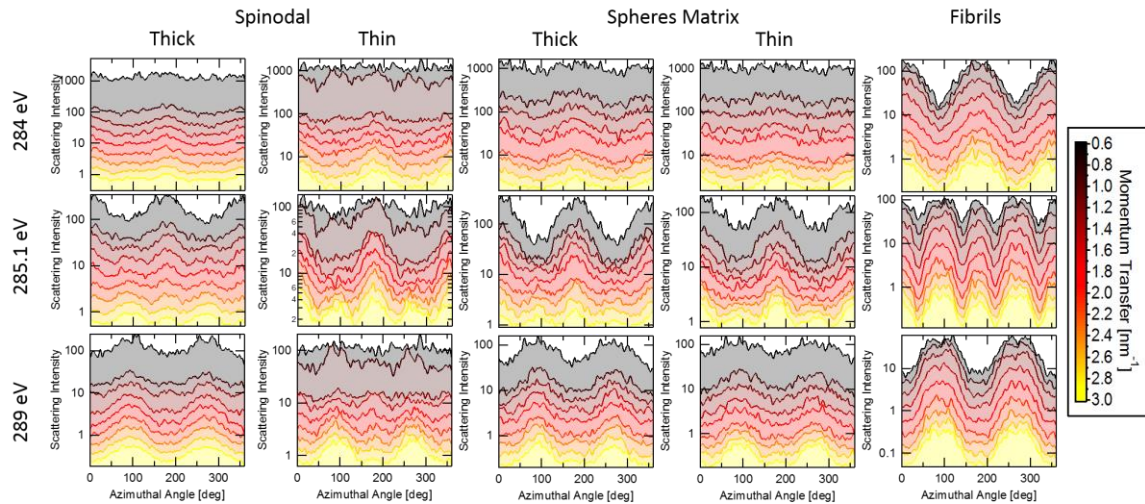


**Figure 4-5 Scattering vs. Azimuth Angle – Edge-on**

Figure 5 Lorentz-corrected scattering vs. azimuth angle at different momentum transfers for Edge on alignment. Graphs each column are from left to right, spinodal decomposition with alignment extending 50 nm from the interface, spinodal decomposition with alignment extending 15nm from the interface, Spheres with alignment extending 15nm from the interface, spheres with alignment extending 15nm from the interface, and Fibrils with alignment throughout the fibril along the fibril axis. Rows are at (from top to bottom) 284 eV, 285.1eV, and 289 eV. Azimuthal angle is relative to the incident X-ray E-Field.

First, the general differences between 284 eV and 289 eV appear to be a phase shift of 90 degrees for all the samples. The phase of the signal at 284 eV is generally indicative the alignment, face on resembles a sin wave generally, whereas edge on anisotropies resemble cosines. This relationship flips at 289 eV however, the differences between 284 eV and 289 eV are not a simple phase shift. In general, at 289 eV the troughs of the anisotropic signal are flattened out, and in the spinodal morphologies even slightly peaked.

Differences between the different morphologies are easiest to pick out in the q dependence of anisotropy. For the spinodal samples, the higher intensities, lower q values have the lowest apparent anisotropy, while the higher q values have increasing anisotropies. Spheres

have generally similar anisotropies at different  $q$  values, while fibrils have essentially identical anisotropy at every  $q$  value.

285.1 eV is a generally very useful energy to distinguish all the different morphologies and the kind of alignment. Particularly interestingly, this energy clearly distinguishes a fibril structure from other edge-on morphologies.

#### 4.9 LORENTZ CORRECTED SCATTERING PATTERNS

Mirroring the analysis done in experiments, we further reduce the 2D data to one-dimensional profiles in momentum transfer, Lorentz correcting to correct for all the area of  $q$ -space which were not captured by intersection with the Ewald sphere. This follows from the fact that although the scattering pattern is anisotropic, the sample itself is isotropic. The same scattering pattern could, in principle, be collected upon rotation of the sample to arbitrary  $\theta$  and  $\phi$  (although it may be experimentally impractical because the thin film allows scattering easily only with the beam close to normal to the film). To represent a 1D projection of this intensity vs.  $q$ , integrating around the sphere of Fourier space is necessary.

$$I_1(q, \lambda, \hat{E}) = \int_0^\pi d\phi q \sin(\theta) \int_0^{2\pi} d\theta q I(q, \theta, \phi, \lambda, \hat{E}) = 4\pi q^2 I(q, \lambda, \hat{E}) \quad (10)$$

$I_1(q)$  for non-resonant scattering from every model system is shown in Figure 4.6. The benefits of Lorentz scaling include it being straightforward to compare different frequency components present in the system, in a representation that matches the PSD calculated by real-space microscopies [176]. It does not overly favor low frequencies, and is representative of the total number of scattered photons in space. This form would be Fourier transformed back to real space to calculate a one-dimensional correlation function, or integrated to calculate a

scattering invariant. Viewing the scattering in this way often presents more directly interpretable information.

As a note, concerns about the combination of shape (form factor) and size (structure factor) commonly associated with Lorentz corrections are not a concern in systems of these

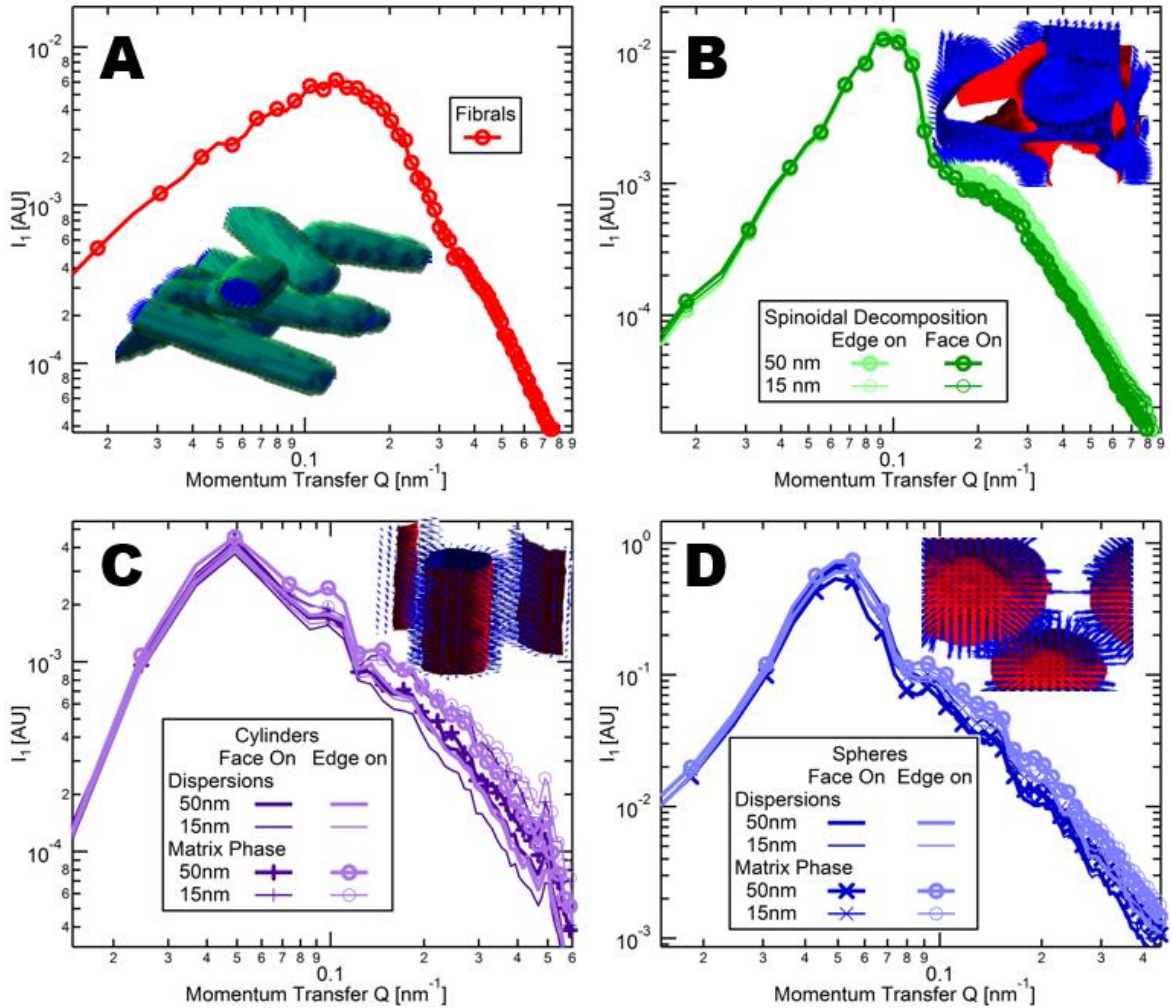


**Figure 4-6 Azimuthally Reduced Scattering**

Figure 6 Lorentz-corrected azimuthally integrated scattering profiles of A) a fibril network calculated only in the Edge-on orientation, as the crystal growth only allows for this orientation. B) 15 and 50 nm thick alignment in face-on and edge-on orientations in a Spinoidal decomposition. C) Spheres and D) cylinders with the same parameters, are additionally created with the aligned polymer in both the matrix and dispersion phase.

high volume fractions. The structure factor and form factor are both present but both contribute to the peak. This is easily seen in the spinodal decomposition case, when the form and structure factor are conceptually the same. In dispersive cases, as the volume fraction increases, the chord lengths within a dispersion become comparable to those in the matrix, and so treating the two as separate populations is no longer possible.

The scattering patterns shown in Figure 4.6 show the insensitivity of non-resonant scattering to the alignment properties, but only the density differences between which material is the dispersion or matrix. However, all of the scattering patterns in Figure 4.6 are largely even similar amongst the different morphologies, meaning that even the precise morphology is not clear from the reduced scattering pattern by itself. The insets in Figure 4.6 are meant to give an idea of the morphology, all of the alignment maps for every morphology is presented in the supplemental information.

#### 4.10 CALCULATING ANISOTROPIC SIGNAL

To examine in detail the anisotropy in all of the different morphologies at once, we calculate a one dimensional anisotropic signal  $A(q, \lambda, \hat{E})$ . Scattering patterns are calculated for each sample morphology at energies from 260 eV to 320 eV in 0.1 eV steps and  $A(q, \lambda, \hat{E})$  is calculated from 20 degree sectors parallel and perpendicular to the vector of the electric field polarization.

$$A(q, \lambda, \hat{E}) = \frac{I_{\perp\perp}(q, \lambda, \hat{E}) - I_{\perp\parallel}(q, \lambda, \hat{E})}{I_{\perp\perp}(q, \lambda, \hat{E}) + I_{\perp\parallel}(q, \lambda, \hat{E})} \quad (11)$$

Which, because  $I_1(q, \lambda, \hat{E}) > 0$  from its definition (4) and (10)

$$-1 < A(q, \lambda, \hat{E}) < 1. \quad (12)$$

$A = 0$  is an indication of isotropic signal, and deviations towards  $\pm 1$  indicate anisotropic scattering perpendicular or parallel to the polarization, respectively. Although looking at 20 degree sectors centered around 0 and 90 degrees does not capture all the information as shown in Figures 4.4 and 4.5, particularly the four fold symmetric patterns at 281.5 eV, it is a simple way to reduce this very complex scattering pattern to a form that can be quickly computed and compared. Although the full 2D scattering patterns contains much more information, this reduction is sufficient to quickly see major differences between morphologies and alignment patterns.

Anisotropy vs. momentum transfer and X-ray energy is shown in Figure 4.7 (face-on orientations) and Figure 4.8 (edge on orientations) for the q-range  $0.01 \text{ nm}^{-1}$  to  $1 \text{ nm}^{-1}$  and energy range 276 eV to 294 eV. Figure 4.7 A-E have 15 nm of alignment, while G-K have 50 nm of alignment in the same respective material systems. Figure 4.7F is a randomly aligned phase where the interfacial alignment energy in the Monte Carlo was set to zero, so only nearest

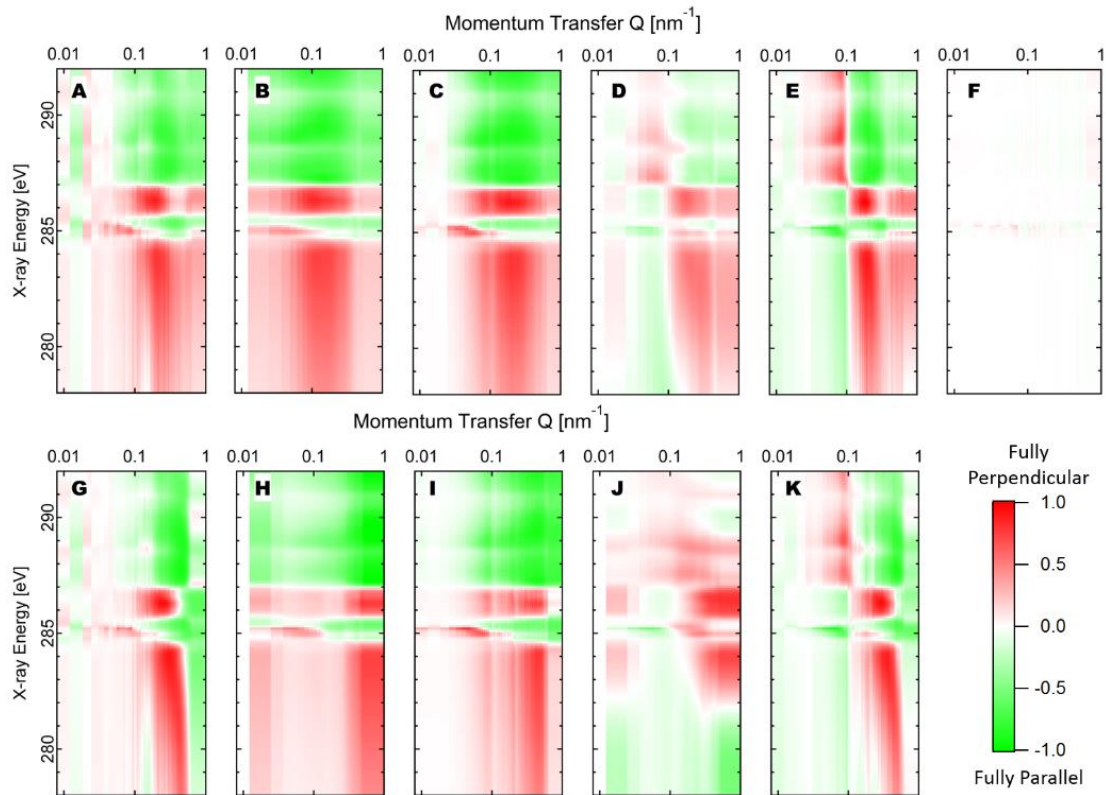


**Figure 4-7 Face On Anisotropy Maps**

Figure 7 Anisotropic Ratio vs. momentum transfer vs. X-ray energy maps A–E are 50 nm of face-on alignment, while G–K are 15 nm of face on alignment for A,G) spinodal decomposition, B,H) Cylinders with the alignment in the matrix phase surrounding the cylinders, C,I) spheres with the alignment in the matrix phase surrounding the spheres. D,J) Cylinders with alignment phase in the dispersed phase inside the cylinders, and E,K) Spheres with the aligned phase inside the spheres. F) A spinodal decomposition system in which there is no entropic cost of alignment and the interface does not affect the alignment, resulting in no anisotropy.

neighbor alignment matters. This creates a model where nearest neighbor alignment is the only concern, and there is little entropic cost to full alignment.

Figure 4.8A-G and G-K are the same  $\Phi_i(\vec{r})$  and alignment energies as in Figure 4.7, except in these Monte Carlo calculations, the energy of being aligned with the gradient at the interface is reversed, causing the lowest energy state to be perpendicular to the normal vector. This causes edge-on interfacial alignment, but because there are two ways to be edge on for a

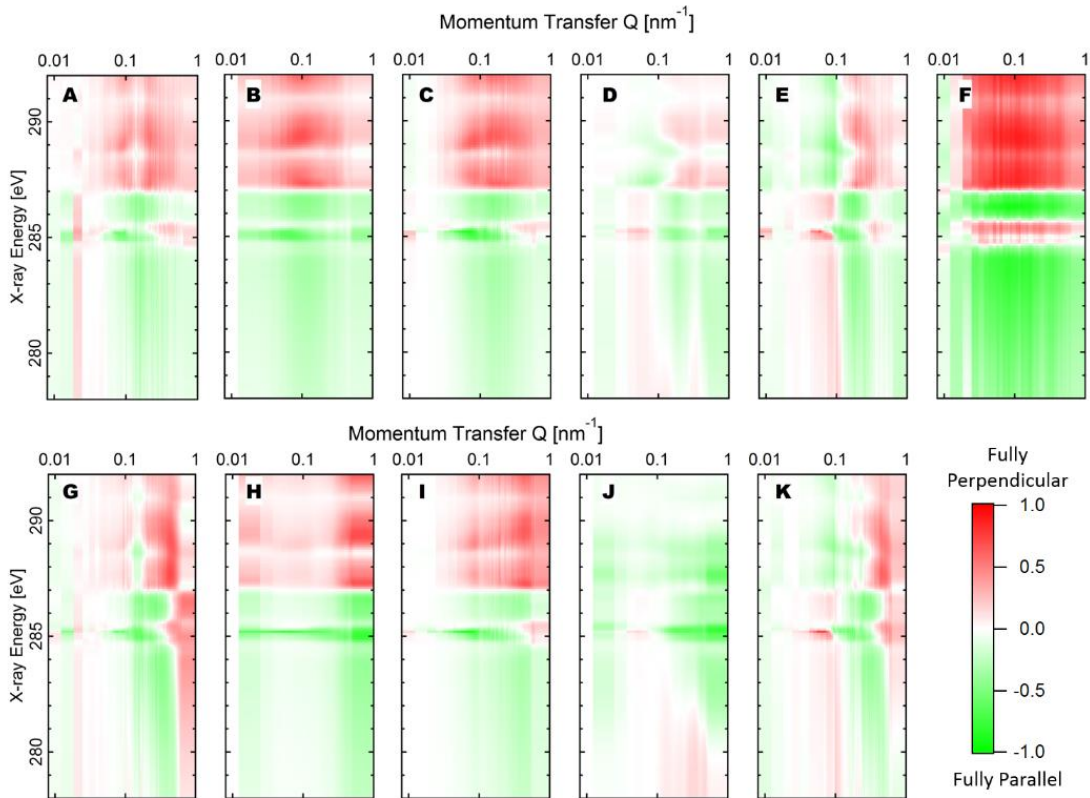


**Figure 4-8 Edge-on Alignment**

Figure 8 Anisotropic Ratio vs. momentum transfer vs. Energy maps A–E) are 15 nm of edge-on alignment, while G–K are 50 nm of edge on alignment for A,G) spinodal decomposition, B,H) Cylinders with the alignment in the matrix phase surrounding the cylinders, C,I) spheres with the alignment in the matrix phase. D,J) Cylinders with alignment phase in the dispersed phase inside the cylinders, and E,K) Spheres with the aligned phase in the dispersions. F) A Fibril network system in which all the alignment is within and along the axis of the largely in-plane fibrils.

single way to be face on, the anisotropic signals are not merely the opposite of those shown in Figure 4.8. In addition, Figure 4.8F is the fibril network, which is in a sense exclusively edge on because of the fibril growth direction is along the pi-stacking direction.

#### 4.11 DISCUSSION

The anisotropic patterns shown in figures 4.7 and 4.8 reveal that anisotropy can be a fingerprint of different morphologies. Changes in the bulk of the anisotropy vs. energy is a clear indication of the orientation at the interface of the heterojunction. In all cases, at  $\sim 284$  eV (the strongest contrast between PCBM and all alignments of P3HT but particularly that perpendicular to the E-field) anisotropy is highest parallel for edge on alignments, and perpendicular for face on alignments. Just knowing the alignment at the interface can help to explain charge splitting and recombination as the anisotropy in optical constants also creates a similar anisotropy in charge transport properties [177].

Additionally, the changes in scattering between matrix and dispersed phases is evident, shown by a switching in anisotropy at about the peak of scattering intensity (i.e. the dominant spatial frequency in the system). The alignment in one of the phases breaks the symmetry and so also breaks Babinet's principle.

The thickness of the aligned portion of material itself seems to change the  $q$  dependence of the anisotropy patterns presented. The thicker alignment (the upper rows of the figures) results in stronger anisotropy at lower  $q$  values, closer to the location of the scattering peak. Thinner alignment layers change the falloff of the peak at higher  $q$  values. This might be interpreted as changing the effective roughness of the interface. The scattering pattern of a randomly aligned system shown in figure 4.7F shows no anisotropic signal. This illustrates

how the correlation between alignment and morphology is critically necessary to break the symmetry and produce anisotropic scattering. On the other extreme, the case of fibrils is interesting in that the morphology allows only one possible anisotropic signature in the system. The simplest anisotropic pattern, fibrils exhibits high anisotropy across all q ranges.

Much of the energy dependence observed in Figures 4.6 and 4.7 is specific to our choice of P3HT and PCBM as the materials of interest. Different optical constants for different polymers will cause the details of the anisotropic maps to change, potentially dramatically, and so these alignment maps should not be used as a fingerprint for other material systems, but rather an indication of the variety of behavior to expect even in a relatively simple system. Increased understanding of crystal growth and alignment will also allow more complex treatment including moving beyond the uniaxial simplification in packing behavior as well as optical constants. A full tensor treatment of both alignment and optical behavior is a natural extension of this work.

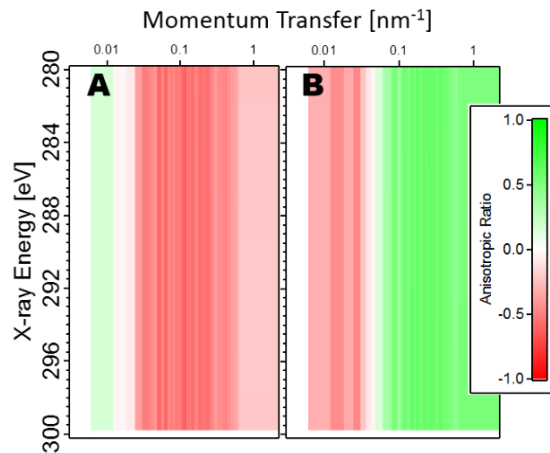


**Figure 4-9 Homopolymer Anisotropic Signal**

Figure 9 The anisotropic signal for pure P3HT systems. A) Fibrils B) radially face on Spherules. The anisotropy is identical across the full energy range.

An interesting note is that the same calculations can be done for the single material P3HT (Figure 4.9). In this case, the anisotropic ratio is constant at all energies. This follows directly from the uniaxial supposition, because, although the contrasts between alignments of p3ht change, they all change linearly relative to each other, so that for instance, p3ht parallel to the electric field will always have twice the contrast with amorphous than p3ht perpendicular to the electric field. Thus a homopolymer system, if it exhibits anisotropy, will exhibit the same anisotropy at all energies. Of course, when other sources of scatter are included in the system, the anisotropy may be washed out relative to a background isotropic signal, but the anisotropic signal will not change signs above and below the edge as the simulations with P3HT and PCBM do.

#### 4.12 CONCLUSION

We have presented a simple model to explain the anisotropic scattering patterns observed in organic systems with no morphological anisotropy. We show that templating morphology from a heterointerface, created either in the process of phase separation or nucleated realignment after phase separation has occurred explains the spontaneous breaking of symmetry in the scattering pattern. We show in three systems that interfacial alignment can explain a rich variety of anisotropic signals, and that that anisotropy can be used to gain new insight into the workings of important devices.

Even showing that with the same materials, between the scattering patterns and anisotropic signals, a myriad of unique morphological information is available. While it is true that real-space information may guide the choice of model, details of the anisotropy present a unique ability to distinguish between otherwise difficult or impossible to distinguish

morphologies and alignments, and give new insight into internal workings of these important devices.

We have identified several ways in which anisotropic signal originating from fibrils and interfacial alignment differ. Interfacial alignment in particular is important to many critical system properties. In the future, this model can be used to fit the level of alignment, give information about the depth of propagation into the bulk phase, and more details of the material specific morphology. In order to model these systems, anisotropic optical constants are necessary, and we present a simple model of calculating the extreme optical constants needed. We have presented criteria for using anisotropy to gain important insight into device morphology and molecular alignment, and we expect that these criteria will be useful in distinguishing between morphologies in these important systems.

#### 4.13 SUPPLEMENTAL INFORMATION

Figures S1-S6 present the results of the Monte Carlo and details about all the simulated morphologies.

Each morphology has a 3D director plot of alignment in 3 dimensions, and a two dimensional cut down the middle of the film, with alignment shown in the plane of the cut. If alignment is out of the plane of the cut, it is not shown. Thus for edge on morphologies, there are blank sections, which imply out of the plane alignment. In all cases, the aligned phase is P3HT, and the unaligned phase is PCBM, and alignment at the interface is set to full alignment along the direction of gradient. The exception is for the fibril sample, where creating the fibril and the alignment map was done in the same step, because alignment is always along the axis of the fibril.

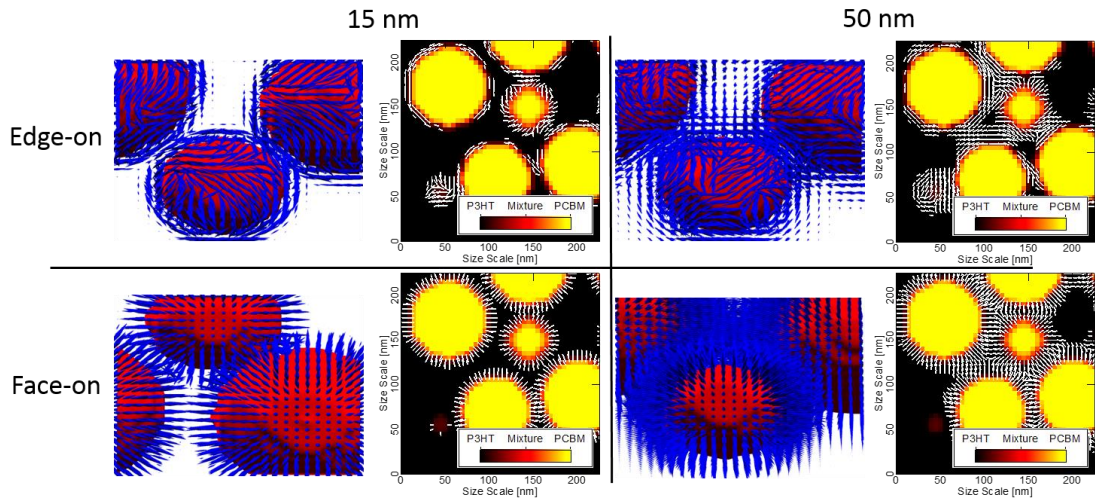


**Figure 4-10 Spheres Alignment Maps Matrix**  
 Figure S1 – Spheres with Alignment in the Matrix

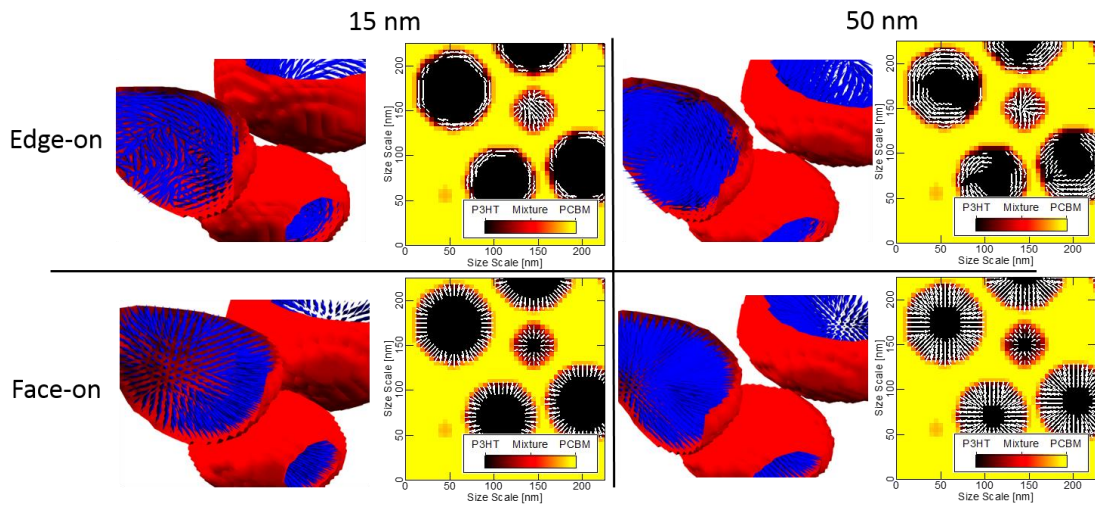


**Figure 4-11 Spheres Alignment Maps Dispersion**  
 Figure S2 – Spheres with Alignment in the Dispersion

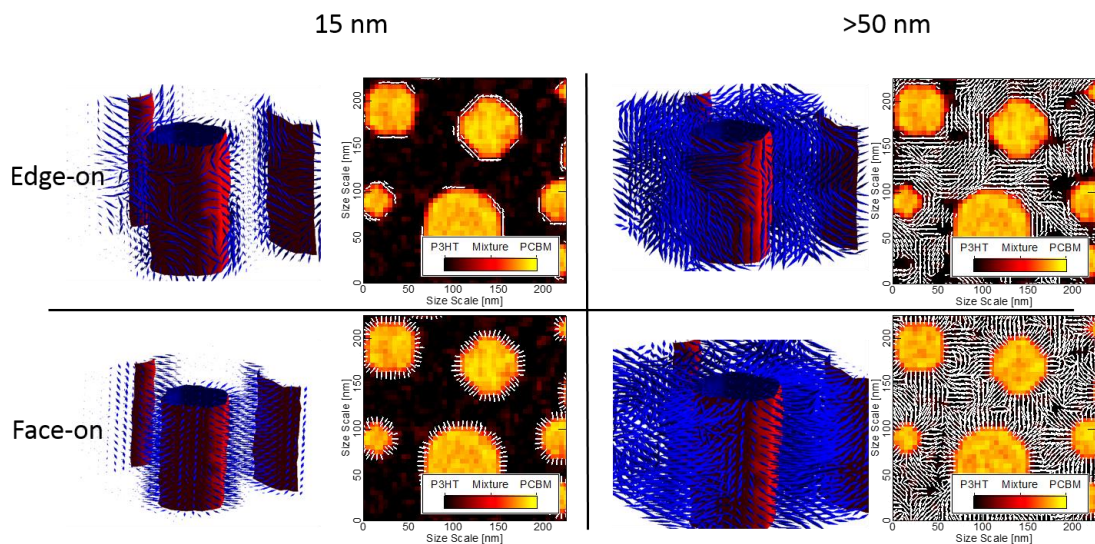


**Figure 4-12 Cylinders Alignment Maps Matrix**  
 Figure S3 – Cylinders with Alignment in the Matrix

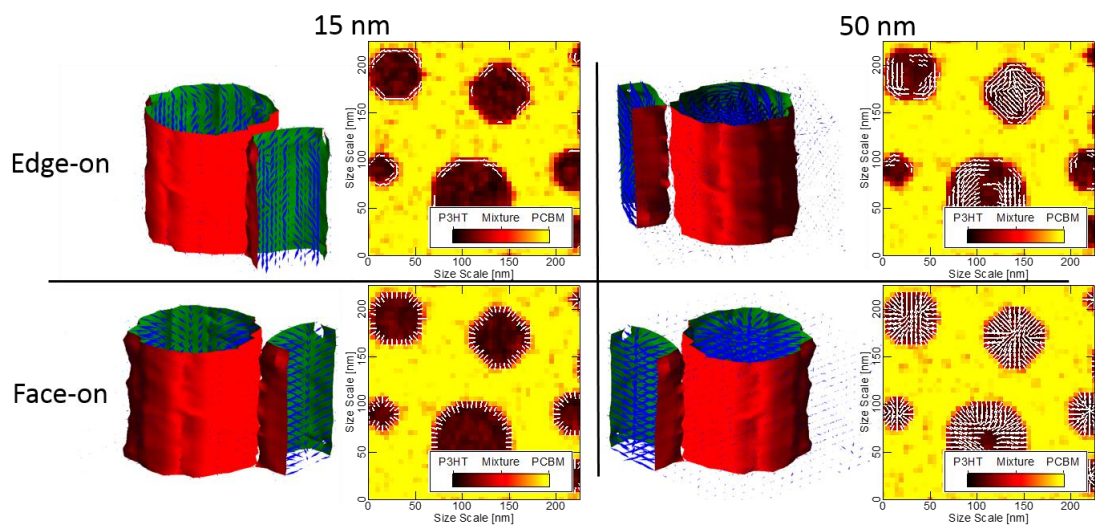


**Figure 4-13 Cylinders Alignment Maps Dispersions**  
 Figure S4 – Cylinders with Alignment in the dispersion

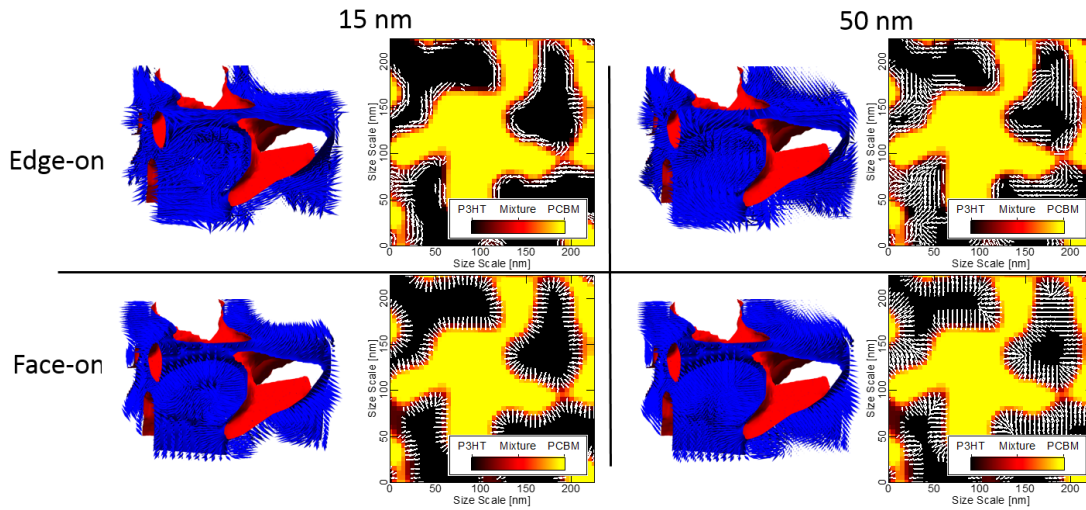


**Figure 4-14 Spinodal Decomposition Alignment Maps**

Figure S5 – Sample morphology created by Lattice Boltzmann method of two symmetric phases demixing.

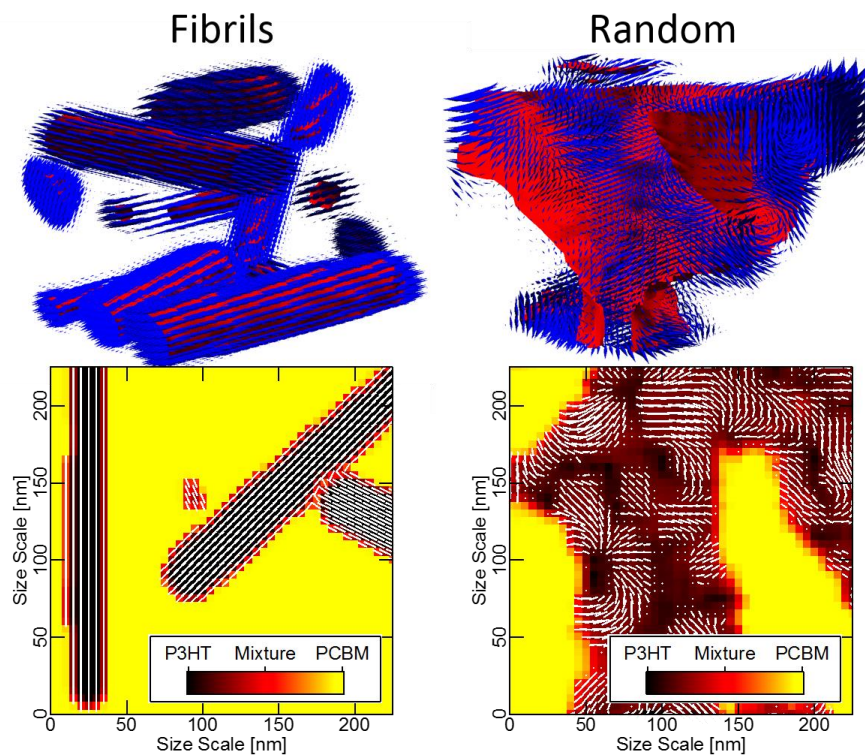


**Figure 4-15 Fibrils and Random Alignment Maps**

Figure S6 – Fibrils, with Alignment along the axis of the fibril

The noise in the cylinder sample (Figures S3 and S4) is exactly that, simulated noise in the concentration of each element. This simulates a slightly unstable system, where small amounts of one material are still present in the other. This is an effort to crudely simulate slightly miscible systems [21, 23, 167, 169]. This also creates small pockets of slightly random alignment, not associated with the interface. It was found that this added noise did not affect the anisotropic signal.

## *Chapter 5*

### **X-RAY CONTRAST VARIATION AND WAVE GUIDING REVEAL MESOSCALE STRUCTURE AT BURIED ORGANIC INTERFACES**

The following paper is a report prepared for Science. The goal of this project has been to develop GRSoXS, which we propose has the ability to look at buried interfaces and other internal thin film structure. It does this by a combination of GISAXS, and RSoXS, two relatively well established techniques which exploit different mechanisms, wave guiding and contrast variation, respectively. However no one had yet combined both of these effects at once. I collected the data Sept 2010 and July 2012 at the Advanced Light Source. The technique's experimental procedure and theoretical model was all my own creation. The first data set suffers from much of the initial normalization trouble, (before the work that lead to the publication in Chapter 2) which was fixed by the time the second dataset was collected. The initial conception of using grazing incidence X-rays in resonant conditions to look at buried interfaces, came from my advisor, Harald Ade, and his then grad student Cheng Wang. However these early efforts never panned out, both because procedures and equipment did not yet exist. Jaewook Seok helped me create the first sample, giving me the idea of using a cross linked polymer to mold the interface. Anne Watson helped with the theoretical development, particularly by writing a prototype version of the fitting code. John Tumbleston and Hongping Yan aided me with the collection of optical constants which are used in all the calculations. Justin Cochran under the supervision of Michael Chabinyk created the OFET sample.

## X-ray Contrast Variation and Wave Guiding Reveal Mesoscale Structure at Buried Organic Interfaces

Eliot Gann<sup>1\*</sup>, Anne Watson<sup>1,§</sup>, John R. Tumbleston<sup>1</sup>, Justin Cochran<sup>2</sup>, Hongping Yan<sup>1</sup>, Cheng Wang<sup>3</sup>, Jaewook Seok<sup>4,%</sup>, Michael Chabinyo<sup>2</sup>, Harald Ade<sup>1</sup>

<sup>1</sup> Department of Physics, NCSU, Raleigh, NC 27695-8202

<sup>2</sup> Materials Department University of California, Santa Barbara, CA 93106-5050

<sup>3</sup> Advanced Light Source, LBNL, Berkeley, CA 94795

<sup>4</sup> Department of Materials Science and Engineering, NCSU, Raleigh, NC 27695-8202

§ Department of Physics, Duke University, Durham, NC 27708

% Intel Corporation, Chandler AZ, 85226

\*Corresponding Author email: ehgann@ncsu.edu

### 5.1 ABSTRACT:

Internal thin film structures, particularly interfaces between different materials, are often critical to system properties and performance, but characterization of buried internal topography is typically unfeasible. Herein, we demonstrate Grazing Resonant Soft X-ray Scattering, a technique that measures diffusely scattered soft X-rays to selectively reveal the spatial frequency distribution of internal interfaces. Control of the electric field intensity throughout the depth of the film and scattering contrast between materials unambiguously identifies scattering from different sources. Specifically the selective measurement of the surface and buried interface show different topography and differing evolution upon annealing in the example of organic thin film transistors. The technique is demonstrated in two polymer-polymer systems but is readily expandable to any thin film systems with elemental or chemical contrasts exploitable at absorption edges.

## 5.2 REPORT

The properties and performance of thin films often stem from the physical morphology, particularly roughness and interdiffusion at interfaces between component materials [73, 178, 179]. By their very nature scanning probe methods can only characterize exposed surfaces [180]. Microscopies of buried interfaces can be powerful, but are inherently local and require preparation of cross sections [51, 179]. Similarly limited are specular reflectivity methods as

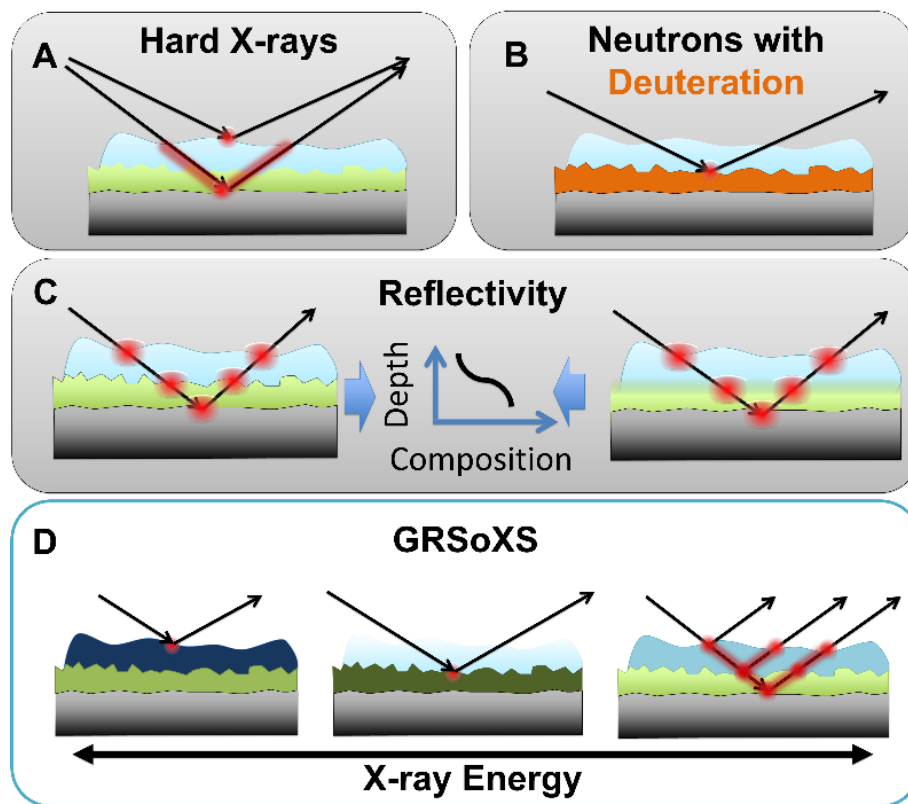


**Figure 5-1 GRSOXS Compared to Other Techniques**

An Illustration showing the difficulty of measuring a buried internal interface by established techniques using a bilayer as an example. Red highlighted areas illustrate the locations of sensitivity. A) Many grazing-incidence probes can isolate the surface and probe the bulk, but cannot distinguish individual layers. B) With modification of the lower layer by deuteration, it is possible to probe a buried interface, but the contrast is fixed. D) Soft X-ray and neutron reflectivity cannot reveal in-plane correlation lengths ( $\xi$ ) within a system. E) Using GRSOXS, the depth ( $z$ ) of scatter can be determined by choice of X-ray Energy.

they lack sensitivity to the nature of the in-plane structure [73, 181, 182] (Figure 4.1D). Complementary alternatives are diffuse, off-specular scattering methods [139, 183-185]. These conventional scattering techniques, for example by varying the incident angle in conventional grazing incidence x-ray scattering [139], control field intensity distribution to enhance or suppress scattering from certain locations within a system. However, these techniques rely on fixed refractive properties of materials. X-rays for example rely on electron density differences [95, 96], which often provides insufficient and unchangeable contrast in systems of similar density or organic systems composed of similar populations of low  $Z$  elements [96, 97]. Neutrons, on the other hand gain contrast by neutron scattering length differences in materials (Figure 4.1C) which can gain interfacial contrast. Unfortunately the neutron scattering lengths are not tunable in situ, but require isotopic substitution to vary contrast [96, 186]. As an alternative, resonant X-ray probes have demonstrated large, selective and variable contrast ( $|\Delta n|^2$ ) where X-rays of different energies selectively probe specific combinations of materials [75, 76]. However, current resonant scattering methods have not utilized field strength modulation to reveal internal interface structure below the upper surface, rather only using surface sensitivity at absorption peaks [187, 188] or only studying bulk properties [12, 79].

The technique presented in this work, Grazing Resonant Soft X-ray Scattering (GRSoXS), successfully combines tunable contrast of resonant soft X-rays, [105, 108] and control of the electric field intensity (EFI) that occurs at grazing angles [139, 189] to gain specific sensitivity to internal interfaces many nanometers below an exposed surface. The EFI of a probe soft X-ray beam consists of nodes, antinodes and exponential decays in the sample as the reflected and transmitted amplitudes interfere and photons are absorbed. Contrast control

distinguishes particular material pairs by exploiting differences in the molecular environment of particular elements, in this case carbon. Contrast and EFI both strongly depend on the index of refraction  $n(z)$  shown in Fig. 5.2A for two polymers near the carbon absorption edge. The simulated scattered amplitude ( $A_{sim}$ ) of a given feature or structure in a film is, to first order, proportional to the materials contrast  $|\Delta n(z)|^2$  (Fig. 5.2B) multiplied by the *EFI* at a given depth ( $z$ ), incident angle ( $\theta$ ) and X-ray energy ( $E$ ) (Fig. 5.2C) at that location.

$$A_{sim}(E, \theta, z) \equiv |\Delta n(z)|^2 * EFI(E, \theta, z) \quad (1)$$

Conceptually this is the product of the amount of probe beam that reaches a location and the probability of scattering. Thus the simulation requires a model consisting of the constituent materials, layer thicknesses and approximate RMS roughnesses in the system.

In order to validate the utility of GRSOXS, a bilayer sample was engineered to have a buried interface with a known RMS roughness and a designed dominant in-plane size scale  $\xi$ . A very thick substrate of polyethylene glycol was molded with the specific  $\xi \cong 35$  nm and crosslinked (see SI for details). The top layer of poly (methyl methacrylate) (PMMA) was applied to the PEG and melted to ensure the film surface had a low RMS roughness and a much larger  $\xi$  than the buried interface. The two polymers of this system were chosen because they

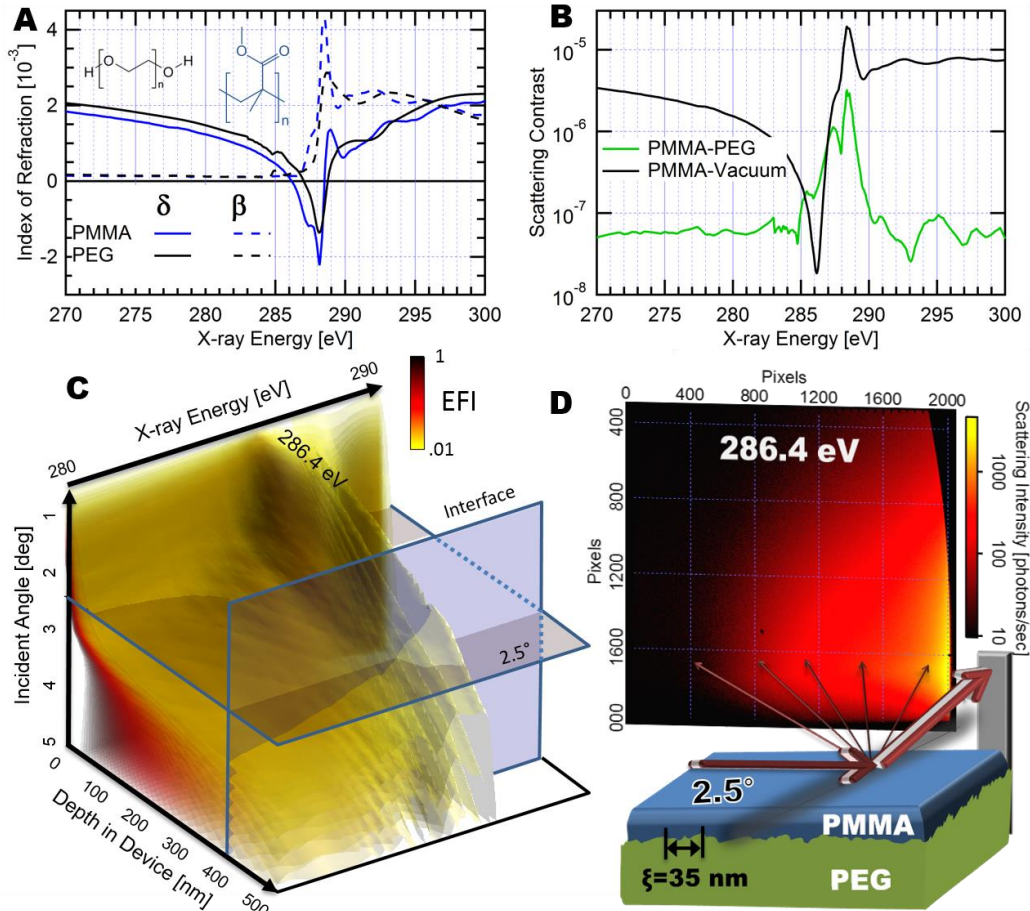


**Figure 5-2 PMMA/PEG Theory and Experimental Setup**

A) Real ( $\delta$ ) and imaginary ( $\beta$ ) part of the index of refraction for PMMA and PEG. Inset are molecular structures of (left) PEG and (right) PMMA B) Contrast ( $|\Delta n|^2$ ) for the top surface and interface. C) A 3D semitransparent isosurface plot of calculated EFI vs. energy, incident angle and depth for the PMMA/PEG system. Isosurface values are 1% (yellow) – 100% (black) of the incident intensity. The slices of this space corresponding to the interface (at a depth of 400nm) and 2.5 degrees incident angle are outlined. Detailed 2D cuts are provided in the supporting information. D) Schematic of acquisition geometry with example raw scattering pattern and the PMMA/PEG sample. The directly reflected X-rays are stopped by the beamstop, while the off specular scattering is captured in the 2D detector.

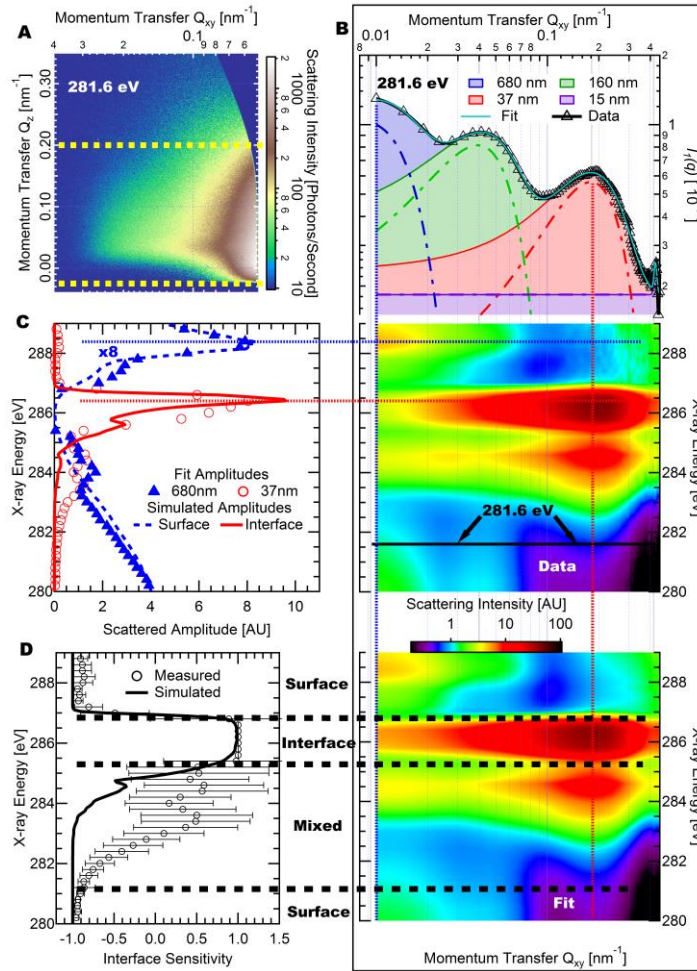
are amorphous, with low bulk scattering and for ease of sample creation, not for high scattering contrast. Indeed, the spectra of the two materials are relatively similar (Fig. 5.2A), and the contrast (Fig. 5.2B) is correspondingly small compared to other material combinations (see

Figure S5G). The overall layout of the experimental and sample geometry is shown in Fig. 5.2D.

Figure 5.3A shows in-plane diffusely scattered 281.6 eV X-rays. By summing over the out-of-plane dimension (between the dashed yellow lines) and Lorentz correcting [97] we produce  $I_1(q)$ , the distribution of in-plane spatial frequencies in Fig. 5.3B.

The experimental fit in Figure 5.3B uses constituent Gaussians corresponding to a physical  $\xi$  that must scatter with the same spatial frequency distribution only changing amplitude  $A_{exp}(E, \xi)$  with energy. The success of the fit in capturing the scattering features and reducing them to a manageable parameter space is evident by comparison of the data and fit vs. energy in the lower panels of Fig. 5.2B. Significantly, the two dimensional data readily shows two distributions, associated with specific energy ranges, which directly indicate a connection to the only two sources of scatter this sample, the surface and the interface.

To unambiguously identify the corresponding source,  $A_{exp}(E, \xi)$  of the most prominent  $\xi_s$  from the fit (37 nm and 680 nm) are plotted vs. energy in Fig. 5.2C along with simulated  $A_{sim}(E, z)$  from the surface and interface. The 160 nm Gaussian was found to have a similar



**Figure 5-3 PMMA PEG GRSoXS Results**

A) A normalized and background corrected exposure acquired at 281.6 eV at the high  $q_{xy}$  detector location. B)  $I_1(q, E)$  and Fit. (top panel) A slice of  $I_1(q, 281.6 \text{ eV})$  and Gaussian components corresponding to four dominant  $\xi_s$ , at an energy where all size scales contribute. (middle panel) measured  $I_1(q, E)$  and (bottom panel) resulting fit C)  $A_{exp}(E, 680 \text{ nm})$  and  $A_{exp}(E, 37 \text{ nm})$  with scaled  $A_{sim}(E, z_{surf})$  and  $A_{sim}(E, z_{int})$  calculated from equation (1). D) Measured and simulated interface sensitivity  $S(E)$  calculated from equations (2) and (3). Error bars are calculated from normalization uncertainty (see SI for systematic errors in 282-284.5 eV range). C and D are displayed with energy on the y axis for direct comparison with the data in B. Dotted red and blue lines are guides to the eye where the interface and surface scattering are highest in energy and momentum transfer. Dashed black lines across the bottom of the figure separate energy regions where the surface or

energy dependence, but lower intensity than the peak at 680 nm. Comparison of the experimental and simulated amplitudes allows definitive identification of dominant size scales at the surface and interface,  $\xi_{surf}=680$  nm and  $\xi_{int}=35$  nm respectively. Because in this system, there are only two major sources of scatter, we define a measured and simulated interface sensitivity  $S(E)$ , as the percentage difference between amplitudes measured and simulated at the buried interface and top surface (Fig. 5.3D).

$$S_{sim}(E) \equiv \frac{\gamma A_{sim}(E, z_{int}) - A_{sim}(E, z_{surf})}{\gamma A_{sim}(E, z_{int}) + A_{sim}(E, z_{surf})} \quad (2)$$

$$S_{exp}(E) \equiv \frac{A_{exp}(E, \xi_{int}) - A_{exp}(E, \xi_{surf})}{A_{exp}(E, \xi_{int}) + A_{exp}(E, \xi_{surf})} \quad (3)$$

To provide an informed comparison of the energy dependence between experiment and simulation, a scaling factor  $\gamma$  is found by scaling  $A_{sim}$  to the corresponding  $A_{exp}$  as in Fig. 5.3C. While the energy and angular dependence can be simulated accurately, the scale factor  $\gamma$  between amplitudes at the interface and surface must be set experimentally. Of interest are conditions such that  $S \approx \pm 100\%$  (for example  $S_{exp}(286.4 \text{ eV}) \approx 100\%$ ) where the interface and surface can be individually probed with high precision.

To demonstrate the utility for GRSOXS to answer vexing questions related to electronic devices, a model bilayer relevant to OTFTs with poly(styrene) (PS), a gate dielectric, on top of poly(2,5-bis(3-tetradecylthiophen-2-yl)thieno [3,2-b]thiophene) (PBTTT), a semiconductor, is characterized by following the methodology delineated above (see SI for raw GRSOXS data, as well as contrast and EFI calculations). Charge transport in OTFTs occurs solely at the interface between the semiconductor and the dielectric [5, 190]. The interface area, slope distribution, and molecular interdiffusion are critical to device performance, but

until now have not been measured directly and non-invasively in a completed or annealed bilayer. Measurements of the interface can guide control of its structure, potentially increasing performance.

The energy dependence of scattering amplitudes, (analog to Fig. 5.3C) are shown in Fig. 5.4A. Again, with these samples two distinct distributions are apparent, the surface consists of size scales at 1.3  $\mu\text{m}$  and 850 nm, while the interface has both 35 nm and 90 nm size scales. For this sample,  $S_{exp}(E)$  is calculated from the more prominent amplitudes where  $\xi_{int}=35$  nm and  $\xi_{surf}=1.3$   $\mu\text{m}$  and is shown along with the calculated sensitivity in Fig. 5.4B.

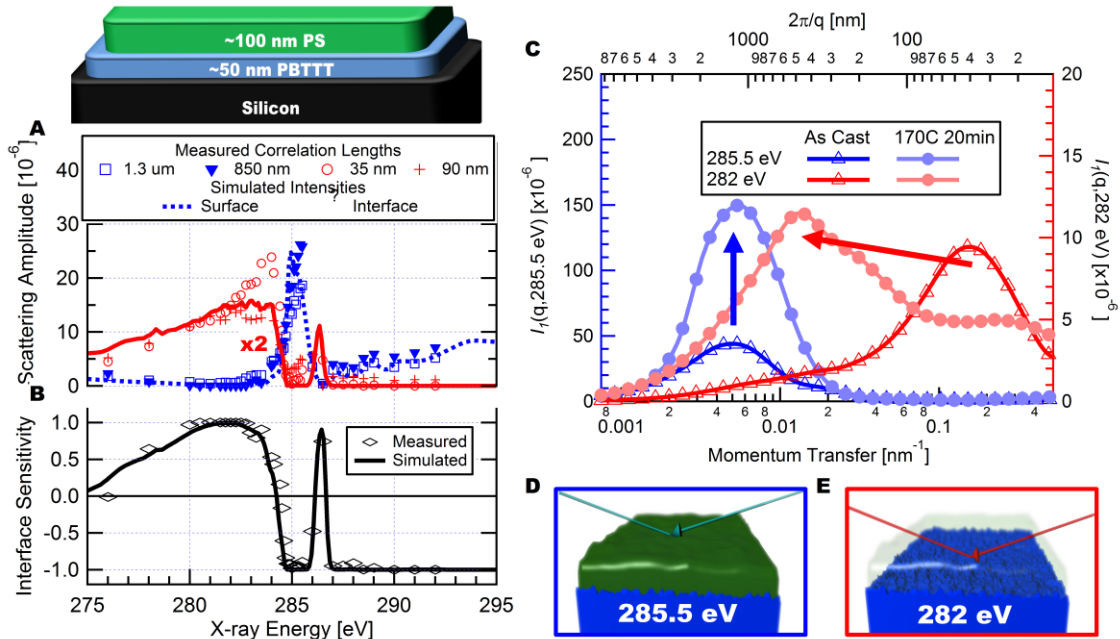


**Figure 5-4 GRSoXS Results for OFET Device**

A)  $A_{exp}(E, \xi)$  and scaled  $A_{sim}(E, z)$  for the PS/PBTTT sample B)  $S_{exp}(E)$  and  $S_{sim}(E)$  for the PS/PBTTT sample C)  $I_1(q, E_{int})$  and  $I_1(q, E_{surf})$  before and after annealing. D) For clarity, a 3D illustration of the surface sensitivity at 285.5 eV when X-rays cannot penetrate further into the sample than  $\sim 10$  nm and probe surface length scales, and E) 282 eV where the top surface is minimally scattering, leaving the signal from the interface maximized.

The higher degree of agreement between measured and simulated sensitivity and lower noise compared to Fig. 5.3D is due to greatly improved facility operating procedures for the later acquired PS/PBTTT data, leading to improved intensity normalization.

Because there are clear ranges of energies with high selectivity for the surface (at 285 eV  $S < -98\%$ ) or interface (at 282 eV  $S > 98\%$ ) we define  $E_{surf} = 285.5$  eV and  $E_{int} = 282$  eV and can examine the detailed spatial frequency distributions,  $I_1(q, E_{surf})$  and  $I_1(q, E_{int})$  respectively. Fig. 5.4C shows these distributions for the unannealed and annealed bilayer. The RMS roughness (proportional to the integrated  $I_1$ ) of the top surface increases significantly as the in-plane spatial frequency distribution stays largely unchanged. In contrast to this,  $I_1(q, E_{int})$  exhibits a complex redistribution of characteristic length scales upon annealing, on average increasing in size. Force microscopy measurements of PBTTT films have previously revealed that thermal annealing above the liquid crystal transition ( $\sim 145^\circ\text{C}$ ) increases the domain size of terraced, topological features [191-193], which is consistent with our result, but it has also been shown that annealing of PBTTT bilayers leads to a different bulk domain size than observed for annealing of free surface [1, 3]. These results thus underscore the necessity of the direct in-situ measurement of the interface topography presented here. Future experiments can use dynamic measurements of  $I_1$  with 5 second resolution. The range of length scales presently probed by GRSoXS is also highlighted by Fig. 5.4C, with sensitivity spanning three orders of magnitude readily achievable.

We have demonstrated the first use of GRSoXS to determine full in-plane spatial frequency distributions of buried polymer-polymer interfaces and measured the interface topography and its evolution upon processing in an OFET bilayer. A simple model matches

the measured amplitude of dominant spatial frequencies. Detailed structure-function relations can now be established for a wide range of thin film systems for which the buried structure critically determines function. The present work clearly illustrates the applicability to organic bilayer systems such as OTFTs and organic light emitting diodes [4], but the technique also has clear applications beyond planar interfaces, to examine detailed internal structure of bulk heterojunction type systems such as excitonic solar cells [11, 194]. There are numerous other systems with buried functional interfaces where optical properties at an absorption edge can be exploited. For example, complex transition metal oxide heterostructures have shown remarkably high-mobility 2D electron gas behavior [195, 196]. The origin of these observations is still debated and progress rests heavily on the ability to unambiguously establish the buried interface composition and structure. Looking further toward emerging device architectures, new heterostructures based on combining different layered materials like graphene, hexagonal boron nitride, and MoS<sub>2</sub> will require sensitive characterization of buried interfaces [197, 198]. We envision GRSoXS as an extremely versatile tool for establishing structure-function correlations at these device-relevant interfaces and devices in general.

### 5.2.1 ACKNOWLEDGMENTS

Data acquired at beamline 11.0.1.2 of the Advanced Light Source in Berkeley (25). The Advanced Light Source is supported by the Director, Office of Science, Office of Basic Energy Sciences, of the U.S. Department of Energy under Contract No. DE-AC02-05CH11231. Discussions and insights from D.B. Dougherty, A. Hexemer, J. Kortright, and A. Young are acknowledged. Research at NCSU supported by NSF (DMR-0906457 and 1207032), UCSB by NSF (DMR 0906224). E. Gann was partially supported by a GAANN Fellowship.

## 5.3 SUPPLEMENTAL INFORMATION

### 5.3.1 DATA ACQUISITION

Vertically polarized soft X-rays with energies between 270 and 300 eV and bandwidth of  $\sim 0.1$  eV were scattered from the samples at a  $\sim 2.5$  degree incident grazing angle at beamline 11.0.1.2 at the Advanced Light Source [79]. This angle was chosen because it ranges from well below (at low energies) to well above the critical angle of the surface and balances intensity of scattering, which favors lower scattering angles, and depth penetration, favoring higher angles. The scattered intensity was measured from the direct specular reflection to 20 degrees in the plane of the sample by tiling three exposures of the 2D CCD detector and combining the resulting scattering patterns into a one dimensional cut of roughly 1 degree around the yoneda peak (Fig. 5.3A). The averaging over  $q_z$  (out of plane momentum transfer) values in this cut was found to be irrelevant, as the in plane structure was the main source of scatter, meaning plots of  $q_{xy}$  (in plane momentum transfer) at different  $q_z$  values varied only by intensity, which indicates that the structure of the scattering is predominantly in-plane. This simplifies the analysis such that the correction for variation in the out of plane direction, as is common in the distorted wave born approximation, was not necessary. The variance of intensity vs.  $q_z$  component of scatter is often also interesting [188], containing vertical depth information, however this information is also accessible through the more developed method of soft X-ray reflectivity, and so is not discussed here. The unique information we present is the in-plane structure in the off-specular direction.

### 5.3.2 PMMA/PEG BILAYER PREPARATION

We produce an internal polymer-polymer interface by molding the lower layer, and setting its structure, then spin coating an upper layer of PMMA thick enough that the surface is relatively smooth. A suitable mold for the lower layer was found to be a thermally evaporated layer of Calcium Fluoride ( $\text{CaF}_2$ ) approximately 200  $\mu\text{m}$  thick [199], which has an RMS roughness of 5 nm and a characteristic shape including a dominant lateral feature size of 37 nm, illustrated in Fig. 5.2G and measured by Atomic Force Microscopy. A mixture of poly(ethylene glycol) diacrylate 84%, Trimethylpropane Epoxyate triaxcelate 15%, and a UV sensitive crosslinker 1% was drop cast on the thermally deposited Calcium Fluoride and exposed to a UV lamp for ~10 seconds producing a flexible ~1 mm thick solid film. This film was released from the substrate and the  $\text{CaF}_2$  was dissolved by water bath. The resulting film was vacuum dried for 24 hours after which, a ~400 nm thick PMMA film was deposited by spin coating in THF. The resulting bilayer was heated at 180°C (above the melting temperature of PMMA) for 24 hours, to smooth out any conformal type roughness at the top PMMA surface. The resulting surface roughness of bare substrate (with no PMMA spun on top), was measured with AFM to be ~5 nm RMS in height and ~35 nm in width, while the surface of the bilayer had a lower RMS height roughness (<1 nm) and a much larger lateral correlation length of ~1  $\mu\text{m}$  (Fig. S1). As discussed below, the X-ray scattering on the bare cross-linked PEG substrate confirmed the same ~35nm in-plane length scale as measured by AFM and index-matched x-ray scattering.

### 5.3.3 PS/PBTTT BILAYER PREPARATION:

The OTFT samples are produced on substrates of ~500  $\mu\text{m}$  thick N doped CZ Silicon <1-0-0> single side polished with 1-2 nm native oxide. Each substrate is cleaved to a 1.5 x 1.5 cm size and cleaned via standard protocols. Polystyrene (PS)  $M_w = 400,000$ , was purchased from Sigma Aldrich, GPC standard classification. Poly [2,5-bis(3-tetradecylthiophen-2-yl)thieno [3,2-*b*]thiophene] (PBTTT), was synthesized and donated by Dr. Martin Heeney of Imperial College and John Cowart, U.C.S.B., under the supervision of Dr. M. Heeney. PBTTT which was used had an  $M_n$  of ~16,000. All solvents were purchased from Sigma Aldrich and are the anhydrous versions, > 98% pure. PBTTT was dissolved at 8 mg/mL in a cosolvent mixture of chlorobenzene and orthodichlorobenzene at a ratio of 1:1. PS was dissolved at 20 mg/mL in toluene under a nitrogen atmosphere. Solutions were heated to 140 °C while stirring at 1000 rpm for 60 minutes then allowed to cool to 100 °C stirring at 300 rpm, then filtered with a 13 mm Whatman 0.2 $\mu\text{m}$  PTFE filter utilizing either a 3 mL glass or 1 mL NormJect syringe. Solutions were left overnight under Nitrogen and kept at 90 °C and stirring at 300 rpm. Thin films of PBTTT were spun onto clean dry substrates from solution using a glass pipette at 1000 rpm and an acceleration of 4000 rpm/sec under ambient conditions. Samples were then dried under nitrogen at 100 °C for 10 minutes to remove residual solvent. The PBTTT layer was ~50nm thick. The PBTTT films were allowed to dry under a nitrogen atmosphere and

slowly cool to room temperature. The upper layer PS films were spun directly onto the PBTTT film from a room temperature solution using a 1 mL NormJect syringe through a 13 mm Whatman 0.2um PTFE filter spinning at 2000 rpm at an acceleration of 6000 rpm/sec. This PS layer was roughly 100 nm thick. One of these bilayers was subsequently annealed at 170C for 20 minutes. Both the spincoating of the upper layer and the subsequent annealing likely altered the surface of the PBTTT.

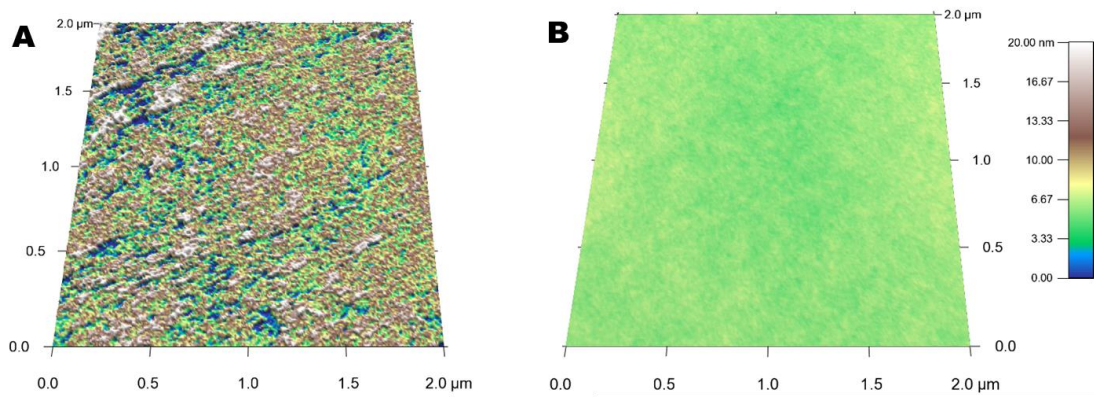


**Figure 5-5 AFM images**

Fig. S1 of A) bare molded interface of PEG showing ~35nm feature size and 5nm RMS roughness B) top surface of PMMA after heating with much larger feature size and <1nm RMS roughness. 3D views are shown in a 1:1:1 aspect ratio, and on the same scale.

#### 5.3.4 UNCERTAINTLY IN MEASUREMENT

For the PMMA/PEG sample, the deviation of onset in measured and simulated  $S_{int}$  from 282 – 284.5 is attributed to poor photon statistics and particularly poor normalization in this region due to the carbon dip [79]. Also, noise in optical constants is high in this region (Fig. 5.2A), which propagate into both the contrast (Fig. 5.2B) and EFI (Fig. 5.2C) calculations. These factors were improved upon considerably before acquisition of the OFET

data in figure 5.4. The apparent peak in intensity at  $\sim 284\text{eV}$  in the 2D scattering intensity is subject to a high level of systematic error, because the raw data in this region is very low intensity, while the normalization values are also low and uncertain. The resulting uncertainty is shown by the error bars in Figure 5.3D, calculated from the range of uncertainty in the normalization values. Fortunately this region of high uncertainty is not of experimental interest, because both the surface and interface have scattering contributions. Between this and the subsequent acquisition of scattering data from the PS/PBTTT sample, experimental protocols involving cross calibration of beam intensity measurements and normalization procedures including acquiring periodic raw beam currents, greatly improved this uncertainty, and low noise scattering intensities could be collected in the region of the carbon dip.

### 5.3.5 DETAILS OF DATA ANALYSIS:

The empirical fit (as shown in Fig. S2) makes several important assumptions which may not hold for different materials systems. First, it assumes each part of the sample scatters independently or incoherently, as correlations between roughnesses could add interferences, which we largely do not see in the data. Secondly, correlation lengths are assumed to be unique within the system. In systems with conformal roughness, the surface and interface roughness may have similar correlation lengths, and so independent energy dependencies may be very difficult to pick out. In that case, linearly fitting a combination of the surface and interface modeled scattering to separate out contributions to different correlation lengths would be necessary. In both of the cases presented in this work, there are two sources of scatter clearly separated in both energy and spatial frequency distribution. In cases where this is not the case, the sophisticated fitting procedures presented here would be even more critical to the

identification of different features. Finally, as shown in the fit of PS/PBTTT scattering (Fig. S2), two interface correlation lengths were found at 35 nm and 90 nm. The stronger correlation length, 35 nm has a large tail, which is fit with the second 90 nm correlation length. Thus the two different lengths are an artifact of the fitting function, and the real correlation length (taking a weighted average based on the fit intensities) is  $\sim 50$  nm. Both constituent Gaussians have the same basic energy dependence, so the higher of the two, 35 nm, is used in Fig. 5.4E interface sensitivity measurement. This doubling might be avoided in the future with different fitting functions (beyond simple Gaussians), but this concern may also be moot if we find an energy at which the interface sensitivity is close to 100%, in which case we can look directly at the shape of the interface as in Fig. 5.4E, and so the dominant correlation values from the fit

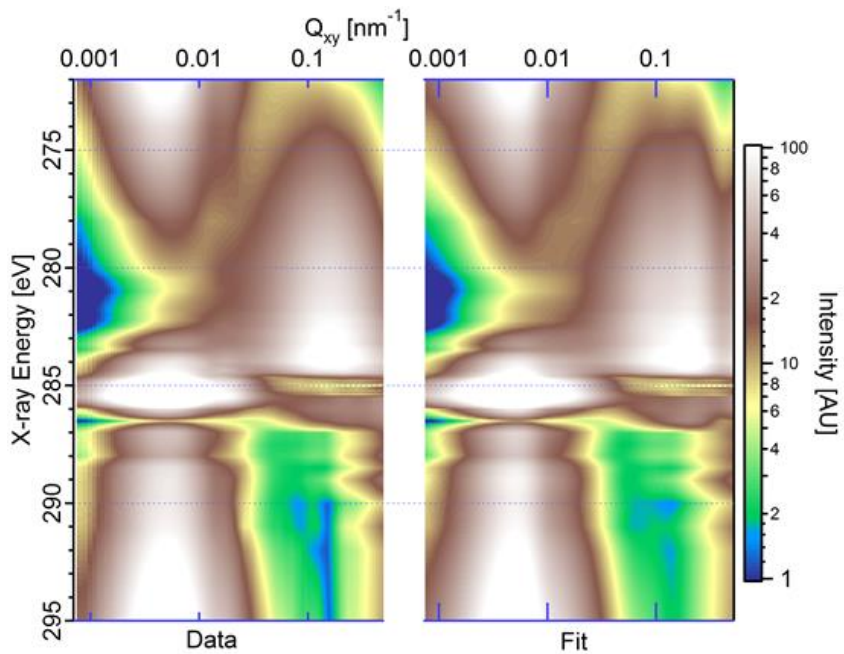


**Figure 5-6 Data and Fit of PS/PBTTT OFET sample**

Fig. S2 Data and Fit of PS/PBTTT OFET sample. Note the non-Gaussian form of roughness at the interface shown by the double peak at  $\sim 0.1 \text{ nm}^{-1}$  in the fit but not in the raw data. Also, again note the two major spatial frequency distributions with their own well defined energy distribution, again indicating two major sources of scatter.

become less important to the structural analysis. Likely principle value decomposition, combining the results of modeled intensities into the fitting routine will be necessary to fully deconstruct complex scattering-energy maps in some cases, particularly in cases of correlated or conformal roughnesses between layers [200].

Lorentz correction is appropriate in this case to correct for all of  $q$  space which does not match the elastic scattering condition. It is the same correction which would be done to find the noise power spectrum of the surface with a linear probe. If the absolute RMS roughness was desired then absolute scattering intensities would be needed, including knowing the incident flux accurately, and modeling the exit path of the x-rays to correct for absorption. Thus for the current experimental difficulties, the absolute RMS measurement is much better suited to a one dimensional reflectivity measurement, which we suggest be used in combination with GRSoXS to find this complementary information. Indeed, the results of the reflectivity measurement (thickness and RMS roughnesses) is exactly the information which should be fed into the simulation to calculate the EFI and parameters for maximal interface sensitivity, so a reflectivity measurement is a natural complement to GRSoXS.

In the two systems we present, we find a largely binary distribution of scattering peaks, which we are able to identify as the top surface and internal interface. In many cases, the scattering from each bulk layer and the substrate may also be substantial, and so much more sensitive fitting algorithms may be needed to pick out all the constituent correlation lengths. We can often discount contributions from a substrate such as Silicon by the simple argument that the correlation lengths of polished Silicon wafers are far smaller than the wavelength

limited resolution of soft X-rays (~4 nm at the Carbon edge). In this way, soft X-rays morphological measurement scale is inherently mesoscale.

As a check of how representative the index-matched scattering is to the actual interface, GRSOXS measurements of the bare substrate were taken as well, and compared to the index-matched location of 286.4 eV for the PMMA/PEG sample (Fig. S3). The Bare Substrate was created with a slightly thinner layer of CaF<sub>2</sub> (due to geometrical variation within the thermal

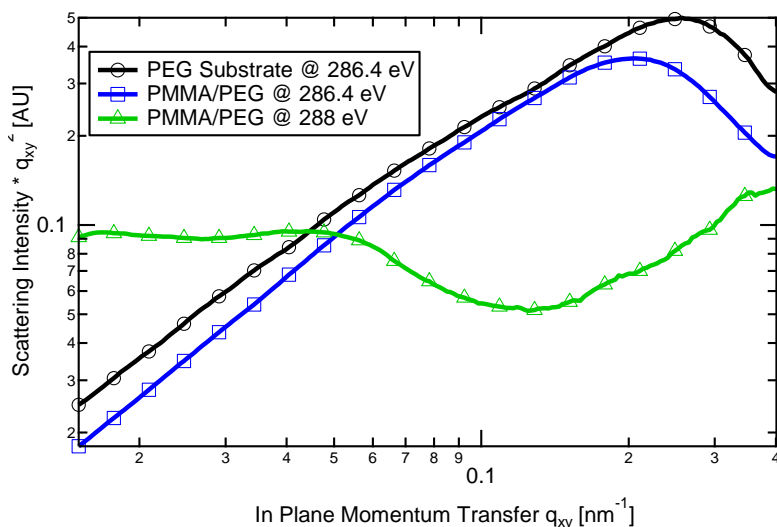


**Figure 5-7 Scattering patterns from the bare molded PEG**

Fig. S3 Scattering patterns from the bare molded PEG, the interface sensitive 286.4 eV and surface sensitive 288 eV scattering patterns of molded PEG covered with ~400 nm of PMMA.

evaporation chamber), leading to 15% smaller feature size. However, the relative intensities are accurate. The distinctive peak is evident in both scattering patterns, with or without the upper PMMA layer. Thus, we conclude that taking a measurement at 286.4 eV is equivalent to looking at the bare substrate, with any effect of the upper layer effectively minimized.

### 5.3.6 CONTRAST:

In the x-ray regime, the refractive index of organic materials is very close to 1, so that we split out the real ( $\delta$ ) and imaginary ( $\beta$ ) parts of the deviation from 1 as:

$$n(E) = 1 - \delta(E) + i \beta(E) \quad (1)$$

Whereas with hard x-rays we would relate  $\delta$  and  $\beta$  to the electron density ( $\rho$ ) within a material, and define the contrast to be proportional to  $\Delta\rho^2$ , with x-rays near absorption edge we instead leave it in terms of  $\Delta n^2$ . Thus to calculate the contrast of a feature composed of two elements with refractive indices  $n_1$  and  $n_2$  is  $(n_1 - n_2)^2$ , which from (1) is

$$|\Delta n|^2 = (\delta_1 - \delta_2)^2 + (\beta_1 - \beta_2)^2 \quad (2)$$

Plotting  $|\Delta n|^2$  vs. X-ray energy (Fig. 5.3F) for various material pairs through a model system, we can see that the interfacial contrast at high and low energies is lower than that of the surface, but in the carbon edge region the contrast varies quickly and has various peaks. Just looking at the contrast however is not sufficient to estimate what energy will be best to see the interface experimentally.

### 5.3.7 EFI CALCULATION:

Using Parratt's multilayer solution with a slicing algorithm, we simulate the EFI throughout a device. By proposing an effective material density for each material through a device (Fig. S4A and S5A), an effective index of refraction at every 1 Å thick layer is determined. At every interface we calculate the Fresnel reflectivity  $r_{ij}$  and transmission  $t_{ij}$ ,

$$r_{i,j} = \frac{k_{z,i} - k_{z,j}}{k_{z,i} + k_{z,j}} \quad (3)$$

$$t_{i,j} = \frac{2k_{z,i}}{k_{z,i} + k_{z,j}} \quad (4)$$

For each interface  $j = i \pm 1$  which allowing the transverse electric field component to remain constant (for s polarization of the X-rays) we can find the following recursive relationships between the electric field components in each layer.

$$E_{\uparrow i} = \frac{e^{ik_i d_i}}{t_{i,i+1}} \frac{1}{r_{(i,i+1)} E_{\downarrow i+1} + E_{\uparrow i+1}}, \quad (5)$$

$$E_{\downarrow i} = \frac{e^{-ik_i d_i}}{t_{i,i+1}} \frac{1}{E_{\downarrow i+1} + r_{(i,i+1)} E_{\uparrow i+1}} \quad (6)$$

Setting the boundary conditions to normalize for the incident beam  $E_{\downarrow}(0) = 1$ , and setting no electric field travelling up from within the substrate itself  $E_{\uparrow}(n) = 0$ , the electric field of both the incoming (direct) and outgoing (reflected) electric field components can be recursively solved within every layer. The results for a bilayer of PS (200 nm) on PBT (100 nm) shown Fig. 5.3C. At every energy, the effective real  $\delta_i(E)$  and imaginary  $\beta_i(E)$  indices of refraction change dramatically, so by picking a depth or region (i.e. the interfacial region) of interest, we can create an energy-angle map of electric field intensities (shown for the interface in Fig. 5.1D and S4).

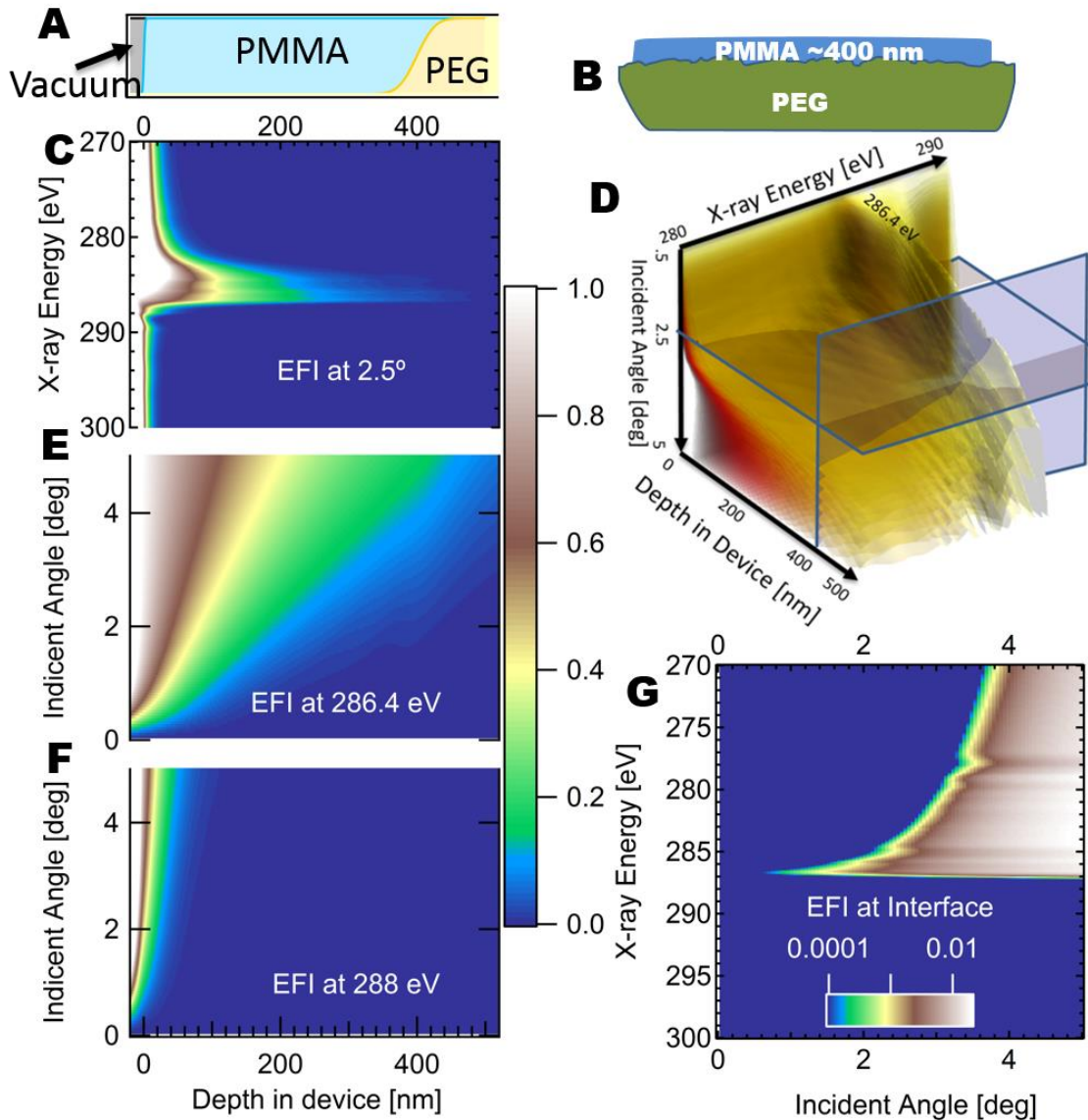


**Figure 5-8 EFI of PMMA/PEG Device**

Fig. S4 Calculated EFI for PMMA/PEG sample A) Material vs. depth in device B) Illustration of device for clarity C) EFI slice at 2.5 degrees D) 3D representation of EFI vs. depth, energy, and incident angle. Isosurfaces are at from 1% (yellow) to 100% (black) of incident beam E) The slice of EFI at 286.4 eV, when X-rays are most penetrating. F) The slice of EFI at 288 eV when the x-rays are least penetrating. G) The integrated EFI in the interfacial region vs. energy and depth.

Modeled EFI for the PMMA PEG sample is shown with various slices to help visualize the 3d data set in Fig. S4. This sample has only one internal interface, and the optical constants

are such that nodes and antinodes formed from interference patterns do not show up, as they do in the OFET sample in the next figure. Although there are no antinodes to take advantage

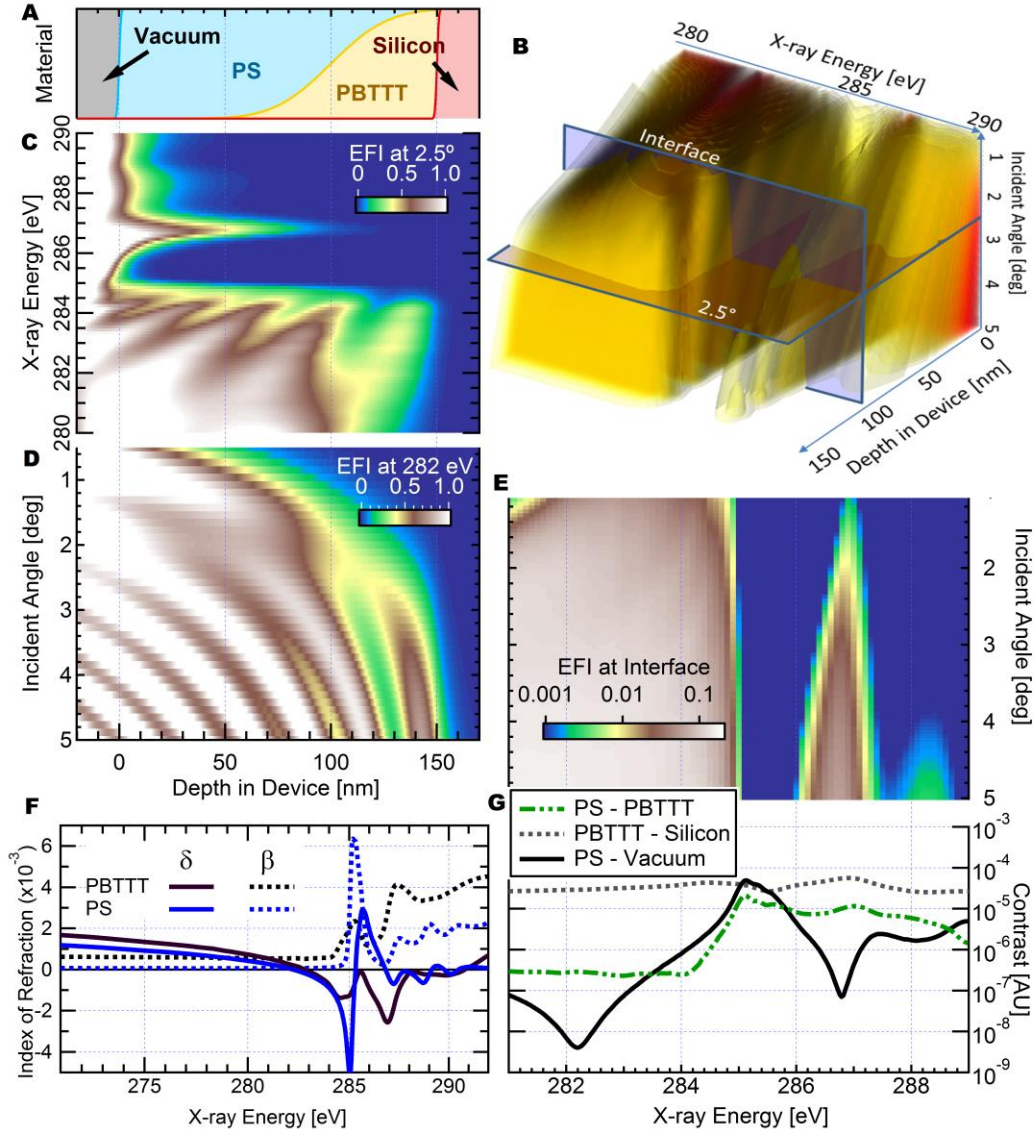


**Figure 5-9 EFI and Contrast of OFET**

Fig. S5 Calculated EFI and contrast of PS/PBTTT sample A) Schematic of device. B) 3D representation of EFI vs. depth, energy, and incident angle. Isosurfaces are at from 1% (yellow) to 100% (black) of incident beam C) The slice of EFI at 2.5 degrees incident angle. D) the slice of EFI at 282 eV vs. depth and angle. E) The integrated EFI through the interfacial region vs. energy and depth. F) The index of refraction of PBTTT and PS. G) The calculated scattering contrast of the different components and thus locations in the sample.

of, the penetration varies dramatically on energy, and this is enough to vary the signal from the interface and obtain an energy signature to match the theory.

Modeled EFI, equivalent to that shown in Fig. S4, but for the OFET PS/PBTTT sample is presented in Fig. S5. With an additional sharp Si substrate layer, standing wave nodes and anti-nodes are much more evident, complicating the choice of energy at which  $S_{int}$  is maximized. The large roughness is likely the result of the toluene, the solvent for PS, during the second spin coating partially dissolving already applied PBTTT layer.

### 5.3.8 ADEQUACY OF PRESENT MODEL

The present model performs exceedingly well in identifying both the energy dependence of scattering from different depths and characteristic energies at which  $|S|$  is maximized. The assumptions made are the same as the distorted wave born approximation (DWBA) [184]. We combine a dynamical theory (allowing multiple interactions between the X-ray and the sample) used to find the EFI within the film, along with a simple perturbation theory (the Born Approximation), assuming the scatter is tiny compared to this established field. If the contrasts within the system were significantly larger double scattering events and more would need to be considered. Additionally, in-plane features will scatter differently from upward and downward traveling fields, and the scattered x-rays will have very different paths out of the sample. We find that in these two simplified systems, these higher order concerns are not necessary to accurately explain the data, however in applying this technique to more complex systems, these further refinements may be necessary.

### 5.3.9 INTERFACE TRACKING DISCUSSION:

The results define guidelines for measuring buried interfaces in thin films systems using GRSOXS. As an example of a simple rule of thumb which can be used to generally enhance the scattering from an internal interface, we here present a method to match the index of the top material to vacuum. This is done at the zero crossing of the real part of the index of refraction ( $\delta$ ). These “index-matched” energies in both the presented cases are also the maxima of interface sensitivity: Fig. 5.2A shows  $\delta$  of PMMA crossing zero at 286.4 eV while Fig. S5F shows PS crosses near 282 eV.

This index-matching is so effective because the first zero crossing of  $\delta$  is lower in energy than the lowest energy peak in  $\beta$ . This is not a coincidence and must generally be the case because of Kramers-Kronig relations governing the relationship between  $\delta$  and  $\beta$  [61]. At this zero crossing then, both elements of the index of refraction are closely matched to vacuum, and effects of the covering layer are minimized. This leaves the buried interface to be probed with minimum background scattering and maximum flux (as depicted in Fig. 5.4). In both of the cases presented, the contrast of the lower layer at these energies is not maximized, but even the low contrast is amplified by the EFI intensity, such that the product is maximized.

Finding such an energy window almost exclusively depends on the composition of this covering layer. Poly(styrene) may generally be a more ideal covering layer. This can be seen by its large low energy range where  $S > 0$  and the huge dip in contrast at 282 eV, an energy that is far below many carbon absorption peaks, meaning absorption effects including beam damage and fluorescence for the whole system are minimized. This energy is so low that for many polymers (including PMMA and PEG), it is still below the critical angle for reasonable

grazing angles of  $\sim 2$  degrees. This means that total internal reflection may be possible from the internal interface in future GRSOXS applications, although in the systems presented in this paper, this was not the case.

To monitor the surface, 285.5 eV, an energy at which the penetration depth of the incident X-rays in PS is limited to  $< 10$  nm is chosen which necessarily limits scattering to the upper surface. Also effective would choosing an energy and angle at which the incident beam is below the critical angle of the surface layer, ensuring total reflection from the surface, and likewise confining the scattering beam to the upper  $\sim 10$  nm of the film. This can be seen by in the EFI penetration at low angles in Fig. S4G and S5G and experimentally for PMMA by comparing in Fig. 5.3B, 280 eV and 288.5 eV and in the Fig. S2, 285 eV, 295 eV and 272 eV. The scattering patterns are all similar at these energies, because they are all high surface sensitivity, although the reason for the lower energies' sensitivity (total reflection) is very different from that of the higher energies (high absorption). Careful care should be made in the comparison of these two regions, because shadowing from slope variations of a few degrees for a top surface will effectively allow X-rays to penetrate a rough top layer even when the beam is below the critical angle on average. Thus the absorption edge, while more damaging for the system is generally a safer experimental choice for isolation of the top surface.

### 5.3.10 EXPERIMENTAL FITTING DISCUSSION

It is interesting to consider the implications of the fitting method presented in this work. The method provides a framework for model free analysis of complex contrast variation datasets, beyond specifically GRSOXS. Even the X-ray energy dependencies were found in the fit, thus no structure or chemistry was presumed. Both the shapes of the Gaussians, (mean

location and width) and the energy dependence of the Gaussians were simultaneously fit. This means that both the size scale and chemistry were simultaneously obtained. In a simpler transmission type system, one could imagine this type of fit giving both the structure of the thin film being probed along with the chemical structure of the constituent materials simultaneously. This is an exciting advance in model free analysis of thin films. Improvements to this method may include, instead of any set functions, an algorithm to find a minimal linear decomposition of scattering vs. energy maps into a set of distributions of spatial frequencies, and their chemical structure.

#### 5.3.11 FUTURE APPLICATIONS

Recently in the field of oxide heterostructures, investigations of the metal L edges have suggested a rumpled morphology at  $\text{LaAlO}_3\text{:SrTiO}_3$  interfaces [201] that might be unambiguously accessed by GRSoXS. In addition, contrast near the oxygen absorption edge using GRSoXS can reveal how variations in oxygen binding environments (e.g.  $\text{OH}^-$ ,  $\text{O}^{2-}$ , or O vacancies) correlate with exotic electronic transport as suggested by studies of oxide-vacuum interfaces [202, 203].

## *Chapter 6*

### **CONCLUSIONS AND OUTLOOK**

This dissertation has presented several methods using resonant soft X-rays to characterize mesoscale structure in thin film organic electronics. A novel synchrotron beamline was presented, which is capable of collecting normalized and quantified scattering patterns from thin films. The theory of scattering in high volume fraction experiments was examined in depth, arriving at several very useful general principles in determining critical factors like domain size and spacing. The use of measured anisotropy when scattering from conjugated polymers with polarized x-rays was explored in depth, revealing that this new phenomenon can provide valuable insight into the structure of thin films. And finally, the development and first results from GRSOXS experiments were described. This chapter will present the outlook for these techniques, and the potentials of extending their power by combining benefits of different techniques to answer critical scientific questions.

#### **6.1 BEYOND CARBON**

Each of these efforts present the community with valuable new tools and understanding for characterizing novel systems. Although they are all presented on organic electronics, and with those structures in mind, the principles are applicable to other organic systems, and by going to other absorption edges, to systems based on other elements as well. Any system that has bonding configurations that have strong resonant resonances at certain X-ray energies can be probed at those energies to exploit similar effects. Possibilities for the oxygen absorption edge are presented in chapter 5, particularly the case for GRSOXS to aid the characterization

of oxide heterostructures. Other examples include L edges in the range of 200-1000 eV range including selenium, titanium, vanadium, chromium, iron, manganese, cobalt, copper, nickel and zinc.

## 6.2 COMBINING POLARIZATION AND GRAZING INCIDENCE

Chapters 4 and 5 detail the use of polarization to probe anisotropy at the molecular scale and the use of grazing incidence and resonance to probe within thin films. These two techniques have the potential to be combined to simultaneously determine molecular orientation, composition, structure, and depth. This possibility promises to help the characterization of thin film transistors to an even greater degree than just knowing structure and composition vs. depth. Because the anisotropic conduction properties are so important in common organic electronics, determining the precise alignment and structure at the interface simultaneously will be a much more powerful use of GRSoXS.

### 6.3 POLARIZED DEPTH-SENSITIVE REFLECTIVITY

Reflectivity is a powerful technique for finding the out-of-plane structure of thin films systems, as described in the introduction. The EFI calculation code I wrote for the theory section of GRSOXS, as a side benefit is identical to the code that would be used to calculate reflectivity with depth and polarization sensitivity. This is one of the simplest extensions of this work to immediately useful experiments. All that is necessary is to implement a fitting

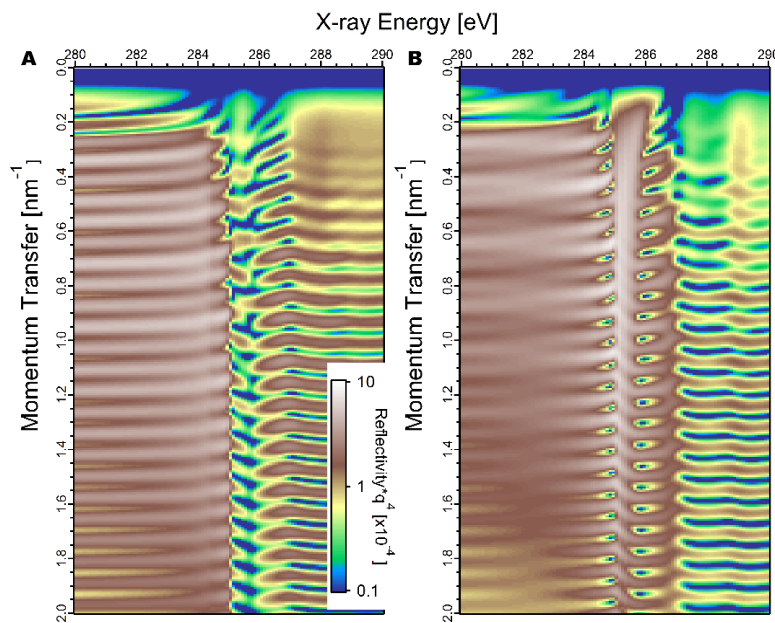


**Figure 6-1 Reflectivity vs Energy and Momentum Transfer**

A) Reflectivity  $\times q^4$  vs energy for a simulated sample of 50 nm of P3HT on top of 30 nm of PS with 3 nm of roughness between the polymer layers. B) Reflectivity  $\times q^4$  vs energy for a simulated sample of 50 nm of PS on top of 30 nm of P3HT with 3 nm of roughness between the polymer layers.

routine with realistic constraints on the depth composition, and a depth profile can be obtained, similar to recent work by Werzer et al [58], but instead of just electron density vs. depth, we could solve for complex index of refraction vs. depth.

The added dimension of X-ray energy in these experiments will allow fits of complex structures to be well constrained. Although currently only sparse energy data may be able to be collected in the time of a typical experiment, it is possible that by shifting resolution from angular space to energy space, (more steps in energy, fewer in angle), necessary data can be collected efficiently.

#### 6.4 OUT-OF-PLANE GRSOXS

The rich data set obtained in GRSOXS experiments was described in depth in Chapter 5, but there we focused on only the in-plane information. The out of plane information, as shown in a data set in Figure 6.2, collected from a bilayer of  $C_{60}$  and Copper Phthalocyanine, contains a rich interference pattern, which is similar to reflectivity, although offset by some

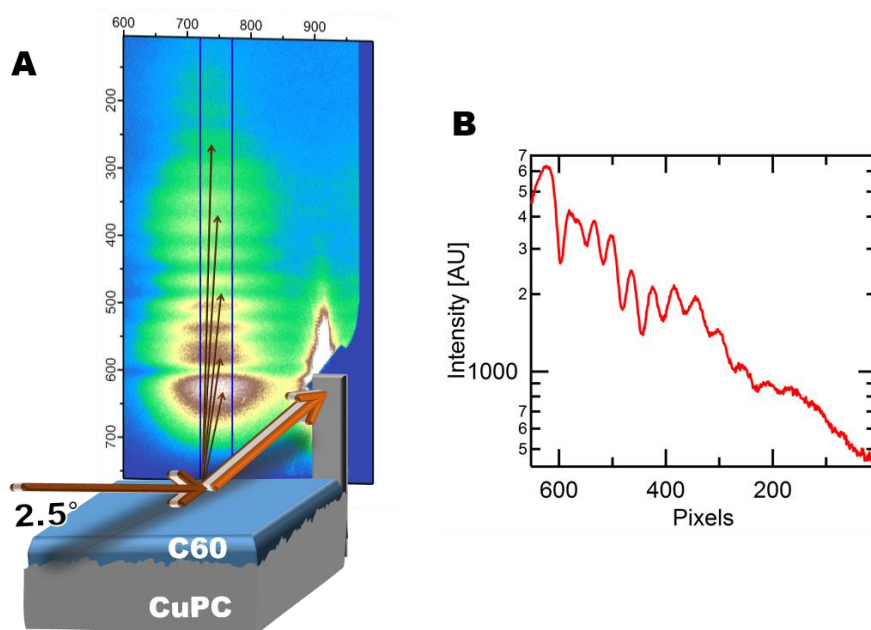


**Figure 6-2 Out of Plane GRSOXS**

A) Out of Plane Grazing resonant scattering pattern and experimental schematic. B) A Line profile taken between the blue vertical lines in A

factor because of refraction. If this can be corrected for accurately, this single scattering pattern may be used in place of a time intensive reflectivity measurement, to solve for the out of plane structure of the thin film simultaneously to the in-plane information measured by the off specular scattering. This, when combined with the depth sensitive reflectivity with energy sensitivity discussed in the last section, may allow the out of plane GRSoXS data to be used to solve for the model parameters, which are then used to predict the in-plane scattering intensity from different depths, thus allowing both the calibration and data to be taken in a single acquisition. It should be noted that the range of momentum transfer able to be captured in a single image is limited geometrically to about ten degrees, far less than the 60 which is common in X-ray reflectivity experiments. This limited momentum transfer range might be made up for by collecting many energies quickly and simultaneously fitting all energies.

## 6.5 RECIPROCAL SPACE PRINCIPLE COMPONENT ANALYSIS

As commonly done in STXM experiments, a stack of real-space images taken at different energies can be decomposed and the energy dependence for each pixel can be fit to a known absorption spectrum of the materials composing the film. In this way, a real space point by point material composition map can be created. One of the exciting possibilities that had yet to be accomplished is to do this same point by point principle component analyses with scattered images. This was done with the Lorentz corrected and averaged data as I've shown in Chapter 5, but this analysis should be applicable to more traditional transmission scattering experiments as well. Rather than a material map (as we get in real space), however, the result would consist of a materials contrast map. This means scattering could be isolated to scattering from pairs of materials.

## 6.6 MODEL FREE ANALYSIS – SOLVING FOR CHEMISTRY AND STRUCTURE SIMULTANEOUSLY

A more complicated version of this principle component analysis is when one of the components is not known.

As has been discussed several times in the thesis (Chapters 3 and 5) there is an exciting possibility with soft X-ray scattering of using a model free analysis to link structure and chemistry of unknown components. Using scattering patterns taken at many energies, the contrasts and structure of different pairs of materials can be both simultaneously solved for. This can provide a clear link between contrast and a spatial frequency distribution within a device. Although going from this contrast to optical constants is not straightforward, if the optical constants of several components are known, then the optical constants of a third material can be solved for.

It is easiest to think about this problem in two dimensions, of the real and imaginary parts of the index of refraction, at a single energy (Figure 6.3). A material (or particular orientation of a material, if considering polarization) is a point in this two dimensional space, having a known delta and beta. The problem of finding the index of refraction of an unknown component can reduce to finding where it lies in this space. Contrast between two elements  $|\Delta n|^2$  is a squared magnitude distance between two of these points. So knowing the contrast between a known material and an unknown material can determine the index of refraction of the unknown material to a circle of potential indices of refraction (Fig. 6.3A), centered at the index of refraction of the known material. Adding another piece of information, perhaps the contrast between vacuum (which is at the origin of this two dimensional space) and the

unknown material will reduce the potential indices of refraction to two or one possibilities, depending on whether there are one or two places where these circles intersect (Figure 6.3B). Of course, other knowledge can help guide this determination, particularly betas that are less than zero (Figure 6.3C) should not generally be allowed. So knowing a vacuum contrast will result in a semi circle of possible indices of refraction, not a complete circle.

A third contrast can constrain the unknown refractive index further, one may think removing ambiguity as in figure 6.3D, but unfortunately the problem may become more

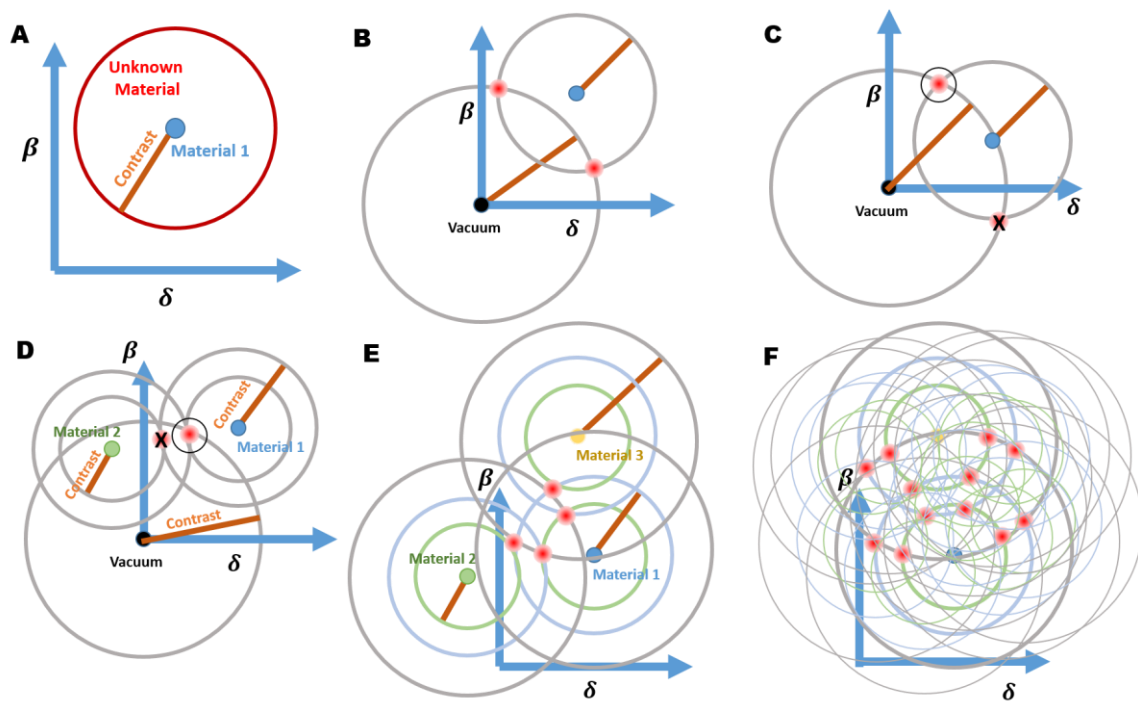


**Figure 6-3 Solving for Unknown Refractive Indices from Contrast**

A) From knowing the absolute scattering contrast, an unknown material can be constrained to a indices of refraction represented by a circle in delta-beta space. B) Two materials and contrasts are known, the unknown refractive index can be reduced to the intersections of two circles. C) Negative beta values are not allowed. D) the case of two known materials and two contrasts, with vacuum contrast. E) Three materials and three contrasts have more intersections. F) If there are two unknowns, then contrasts may be from the two unknown materials as well (shown with finer lines). Red indicates potential indices of refraction in all cases. Contrasts fix the radius of all the circles, and are presumed to be measured by experiment.

difficult. Neither component of a measured contrast is known in general. So, unless a contrast can be constrained by some other knowledge (vacuum contrast is higher below and above the absorption edge, for instance), every contrast must be considered between each possible pair of components. In the two-dimensional picture, then each known material is circled by all unknown contrasts (as in Figure 6.3E), and if there is a unique location a circle of each contrast uniquely crosses, then that can be assigned to the unknown material. The problem quickly becomes unmanageable as more unknown materials are added (Figure 6.3F). If a system of  $m$  known materials has two unknown components, then there are  $2m$  unknown contrasts which must be simultaneously solved, and finding a unique solution of two indices of refraction to explain all the contrasts may very well not be possible.

Complicating this still further, very good measurement of absolute scattering intensities would be needed to solve for absolute contrasts, making the problem currently untenable although still an interesting thought experiment for when the data necessary is experimentally obtainable.

## 6.7 CONCLUSION

Each of these applications are based on the simple principles of obtaining quantitatively normalized data (chapter 2), understanding intricacies of contrast mechanisms (chapters 1,3,4), analyzing Fourier space scattering data correctly (chapters 3,5), and utilizing potential depth sensitivity (chapter 5). GRSOXS in a sense combines all of these elements and reveals how, by orchestrating them carefully, the particular interfacial roughness of polymer bilayers can be isolated out and measured in situ. It is clear that use and further development of the

fundamental soft X-ray scattering building blocks presented in this work, in combinations including those described above, will answer important scientific questions.

## REFERENCES

- [1] B.A. Collins, J.E. Cochran, H. Yan, E. Gann, C. Hub, R. Fink, C. Wang, T. Schuettfort, C.R. McNeill, M.L. Chabiny, H. Ade, Polarized X-ray scattering reveals non-crystalline orientational ordering in organic films, *Nat. Mater.*, 11 (2012) 536–543.
- [2] H.G. Craighead, Nanoelectromechanical systems, *Science*, 290 (2000) 1532-1535.
- [3] M.L. Chabiny, M.F. Toney, R.J. Kline, I. McCulloch, M. Heeney, X-ray scattering study of thin films of poly(2,5-bis(3-alkylthiophen-2-yl)thieno[3,2-b]thiophene), *Journal of the American Chemical Society*, 129 (2007) 3226-3237.
- [4] M.T. Bernius, M. Inbasekaran, J. O'Brien, W.S. Wu, Progress with light-emitting polymers, *Adv Mater*, 12 (2000) 1737-1750.
- [5] R.J. Kline, M.D. McGehee, M.F. Toney, Highly oriented crystals at the buried interface in polythiophene thin-film transistors, *Nat. Mater.*, 5 (2006) 222-228.
- [6] C. Tanase, P.W.M. Blom, D.M. de Leeuw, E.J. Meijer, Charge carrier density dependence of the hole mobility in poly(p-phenylene vinylene), *Phys Status Solidi A*, 201 (2004) 1236-1245.
- [7] F. Garnier, R. Hajlaoui, A. Yassar, P. Srivastava, All-Polymer Field-Effect Transistor Realized by Printing Techniques, *Science*, 265 (1994) 1684-1686.
- [8] H. Yan, Z. Chen, Y. Zheng, C. Newman, J.R. Quinn, F. Dötz, M. Kastler, A. Facchetti, A high-mobility electron-transporting polymer for printed transistors, *Nature*, 457 (2009) 679-686 %U <http://www.nature.com/doi/10.1038/nature07727>.
- [9] J.Y. Kim, K. Lee, N.E. Coates, D. Moses, T.Q. Nguyen, M. Dante, A.J. Heeger, Efficient tandem polymer solar cells fabricated by all-solution processing, *Science*, 317 (2007) 222-225.
- [10] M. Granstrom, K. Petritsch, A.C. Arias, A. Lux, M.R. Andersson, R.H. Friend, Laminated fabrication of polymeric photovoltaic diodes, *Nature*, 395 (1998) 257-260.
- [11] G. Yu, J. Gao, J.C. Hummelen, F. Wudl, A.J. Heeger, Polymer photovoltaic cells - enhanced efficiencies via a network of internal donor-acceptor heterojunctions, *Science*, 270 (1995) 1789-1791.
- [12] B.A. Collins, Z. Li, J.R. Tumbleston, E. Gann, C.R. McNeill, H. Ade, Absolute measurement of domain composition and nanoscale size distribution explains performance in PTB7:PC71BM solar cells, *Adv. Energy Mater.*, 3 (2013) 65-74.

- [13] H. Koezuka, A. Tsumura, T. Ando, Field-Effect Transistor with Polythiophene Thin-Film, *Synthetic Metals*, 18 (1987) 699-704.
- [14] H. Sirringhaus, P.J. Brown, R.H. Friend, M.M. Nielsen, K. Bechgaard, B.M.W. Langeveld-Voss, A.J.H. Spiering, R.A.J. Janssen, E.W. Meijer, P. Herwig, D.M. De Leeuw, Two-dimensional charge transport in self-organized, high-mobility conjugated polymers, *Nature*, 401 (1999) 685–688.
- [15] S.Y. Park, M. Park, H.H. Lee, Cooperative polymer gate dielectrics in organic thin-film transistors, *Appl. Phys. Lett.*, 85 (2004) 2283-2285.
- [16] D.M. DeLongchamp, R.J. Kline, E.K. Lin, D.A. Fischer, L.J. Richter, L.A. Lucas, M. Heeney, I. McCulloch, J.E. Northrup, High carrier mobility polythiophene thin films: Structure determination by experiment and theory, *Adv Mater*, 19 (2007) 833-+.
- [17] R.J. Kline, D.M. DeLongchamp, D.A. Fischer, E.K. Lin, M. Heeney, I. McCulloch, M.F. Toney, Significant dependence of morphology and charge carrier mobility on substrate surface chemistry in high performance polythiophene semiconductor films, *Appl. Phys. Lett.*, 90 (2007) 062117-062117.
- [18] N.S. Sariciftci, L. Smilowitz, A.J. Heeger, F. Wudl, Photoinduced Electron Transfer from a Conducting Polymer to Buckminsterfullerene, *Science*, 258 (1992) 1474-1476 %U <http://www.sciencemag.org.www.lib.ncsu.edu:2048/cgi/content/abstract/1258/5087/1474>.
- [19] R. Po, M. Maggini, N. Camaioni, Polymer Solar Cells: Recent Approaches and Achievements, *The Journal of Physical Chemistry C*, 114 (2010) 695-706 %U <http://dx.doi.org/610.1021/jp9061362>.
- [20] J. You, C.-C. Chen, Z. Hong, K. Yoshimura, K. Ohya, R. Xu, S. Ye, J. Gao, G. Li, Y. Yang, 10.2% Power Conversion Efficiency Polymer Tandem Solar Cells Consisting of Two Identical Sub-Cells, *Adv Mater*, (2013) n/a-n/a.
- [21] B.A. Collins, E. Gann, L. Guignard, X. He, C.R. McNeill, H. Ade, Molecular Miscibility of Polymer-Fullerene Blends, *J. Phys. Chem. Lett.*, 1 (2010) 3160-3166.
- [22] M.T. Dang, L. Hirsch, G. Wantz, P3HT:PCBM, Best Seller in Polymer Photovoltaic Research, *Adv. Mater.*, 23 (2011) 3597-3602.
- [23] B.A. Collins, J.R. Tumbleston, H. Ade, Miscibility, Crystallinity, and Phase Development in P3HT/PCBM Solar Cells: Toward an Enlightened Understanding of Device Morphology and Stability, *J. Phys. Chem. Lett.*, 2 (2011) 3135-3145.
- [24] A. Haugeneder, M. Neges, C. Kallinger, W. Spirkel, U. Lemmer, J. Feldmann, U. Scherf, E. Harth, A. Gugel, K. Mullen, Exciton diffusion and dissociation in conjugated polymer fullerene blends and heterostructures, *Phys Rev B*, 59 (1999) 15346-15351.

- [25] I. Riedel, V. Dyakonov, Influence of electronic transport properties of polymer-fullerene blends on the performance of bulk heterojunction photovoltaic devices, *physica status solidi (a)*, 201 (2004) 1332-1341 %U <http://dx.doi.org.libproxy.lib.unc.edu/1310.1002/pssa.200404333>.
- [26] A.L. Ayzner, C.J. Tassone, S.H. Tolbert, B.J. Schwartz, Reappraising the Need for Bulk Heterojunctions in Polymer-Fullerene Photovoltaics: The Role of Carrier Transport in All-Solution-Processed P3HT/PCBM Bilayer Solar Cells, *The Journal of Physical Chemistry C*, 113 (2009) 20050-20060.
- [27] C.C. Oey, A.B. Djuricic, H. Wang, K.K.Y. Man, W.K. Chan, M.H. Xie, Y.H. Leung, A. Pandey, J.M. Nunzi, P.C. Chui, Polymer-TiO<sub>2</sub> solar cells: TiO<sub>2</sub> interconnected network for improved cell performance, *Nanotechnology*, 17 (2006) 706-713.
- [28] C. Yang, J.G. Hu, A.J. Heeger, Molecular Structure and Dynamics at the Interfaces within Bulk Heterojunction Materials for Solar Cells, *Journal of the American Chemical Society*, 128 (2006) 12007-12013 %U <http://dx.doi.org/12010.11021/ja063707f>.
- [29] C. Wang, A. Garcia, H. Yan, K.E. Sohn, A. Hexemer, T.Q. Nguyen, G.C. Bazan, E.J. Kramer, H. Ade, Interfacial Widths of Conjugated Polymer Bilayers, *Journal of the American Chemical Society*, 131 (2009) 12538-+.
- [30] L.S.C. Pingree, B.A. MacLeod, D.S. Ginger, The Changing Face of PEDOT:PSS Films: Substrate, Bias, and Processing Effects on Vertical Charge Transport†, *The Journal of Physical Chemistry C*, 112 (2008) 7922-7927 %U <http://dx.doi.org/7910.1021/jp711838h>.
- [31] C.J. Brabec, S.E. Shaheen, C. Winder, N.S. Sariciftci, P. Denk, Effect of LiF/metal electrodes on the performance of plastic solar cells, *Appl. Phys. Lett.*, 80 (2002) 1288-1290.
- [32] V.D. Mihailetschi, P.W.M. Blom, J.C. Hummelen, M.T. Rispens, Cathode dependence of the open-circuit voltage of polymer : fullerene bulk heterojunction solar cells, *J Appl Phys*, 94 (2003) 6849-6854.
- [33] F.J.J. Janssen, A.W. Denier van der Gon, L.J. van Ijzendoorn, R. Thoelen, M.J.A. de Voigt, H.H. Brongersma, The influence of surface treatments on cathode formation and stability in polymer light emitting diodes, *Appl Surf Sci*, 241 (2005) 335-351.
- [34] D. Chen, F. Liu, C. Wang, A. Nakahara, T.P. Russell, Bulk Heterojunction Photovoltaic Active Layers via Bilayer Interdiffusion, *Nano Lett.*, 11 (2011) 2071-2078.
- [35] N.D. Treat, M.A. Brady, G. Smith, M.F. Toney, E.J. Kramer, C.J. Hawker, M.L. Chabynyc, Interdiffusion of PCBM and P3HT Reveals Miscibility in a Photovoltaically Active Blend, *Adv. Energy Mater.*, 1 (2011) 82-89.

- [36] D.R. Kozub, K. Vakhshouri, L.M. Orme, C. Wang, A. Hexemer, E.D. Gomez, Polymer Crystallization of Partially Miscible Polythiophene/Fullerene Mixtures Controls Morphology, *Macromolecules*, 44 (2011) 5722-5726.
- [37] S.S.v. Bavel, E. Sourty, G.d. With, J. Loos, Three-Dimensional Nanoscale Organization of Bulk Heterojunction Polymer Solar Cells, *Nano Letters*, 9 (2009) 507-513 %U <http://dx.doi.org/510.1021/nl8014022>.
- [38] S.J. Lou, J.M. Szarko, T. Xu, L.P. Yu, T.J. Marks, L.X. Chen, Effects of Additives on the Morphology of Solution Phase Aggregates Formed by Active Layer Components of High-Efficiency Organic Solar Cells, *Journal of the American Chemical Society*, 133 (2011) 20661-20663.
- [39] M.R. Hammond, R.J. Kline, A.A. Herzing, L.J. Richter, D.S. Germack, H.W. Ro, C.L. Soles, D.A. Fischer, T. Xu, L.P. Yu, M.F. Toney, D.M. DeLongchamp, Molecular Order in High-Efficiency Polymer/Fullerene Bulk Heterojunction Solar Cells, *Acs Nano*, 5 (2011) 8248-8257.
- [40] J. You, L. Dou, K. Yoshimura, T. Kato, K. Ohya, T. Moriarty, K. Emery, C.-C. Chen, J. Gao, G. Li, Y. Yang, A polymer tandem solar cell with 10.6% power conversion efficiency, *Nat. Commun.*, 4 (2013) 1446.
- [41] S.C. Price, A.C. Stuart, L. Yang, H. Zhou, W. You, Fluorine substituted conjugated polymer of medium band gap yields 7% efficiency in polymer–fullerene solar cells, *J. Am. Chem. Soc.*, 133 (2011) 4625-4631.
- [42] J. Vura-Weis, S.H. Abdelwahed, R. Shukla, R. Rathore, M.A. Ratner, M.R. Wasielewski, Crossover from Single-Step Tunneling to Multistep Hopping for Molecular Triplet Energy Transfer, *Science*, 328 (2010) 1547-1550 %U <http://www.sciencemag.org/cgi/content/abstract/1328/5985/1547>.
- [43] D.S. Ginger, R. Giridharagopal, G. Rayermann, O. Reid, D. Moore, G.Z. Shao, Time-resolved electrostatic force microscopy on conjugated polymer blends, *Abstr Pap Am Chem S*, 242 (2011).
- [44] A.H. Rice, R. Giridharagopal, S.X. Zheng, F.S. Ohuchi, D.S. Ginger, C.K. Luscombe, Controlling Vertical Morphology within the Active Layer of Organic Photovoltaics Using Poly(3-hexylthiophene) Nanowires and Phenyl-C-61-butyric Acid Methyl Ester, *Acs Nano*, 5 (2011) 3132-3140.
- [45] R. Giridharagopal, D.S. Ginger, Characterizing Morphology in Bulk Heterojunction Organic Photovoltaic Systems, *J. Phys. Chem. Lett.*, 1 (2010) 1160-1169.
- [46] F. Piersimoni, S. Chambon, K. Vandewal, R. Mens, T. Boonen, A. Gadisa, M. Izquierdo, S. Filippone, B. Ruttens, J. D'Haen, N. Martin, L. Lutsen, D. Vanderzande, P.

Adriaenssens, J.V. Manca, Influence of Fullerene Ordering on the Energy of the Charge-Transfer State and Open-Circuit Voltage in Polymer:Fullerene Solar Cells, *The Journal of Physical Chemistry C*, 115 (2011) 10873-10880 %U <http://dx.doi.org/10810.11021/jp110982m>.

- [47] W. Yin, M. Dadmun, A New Model for the Morphology of P3HT/PCBM Organic Photovoltaics from Small-Angle Neutron Scattering: Rivers and Streams, *Acs Nano*, 5 (2011) 4756-4768.
- [48] B.V. Andersson, S. Masich, N. Solin, O. Inganäs, Morphology of organic electronic materials imaged via electron tomography, *Journal of Microscopy*, 247 (2012) 277-287.
- [49] M.A. Ruderer, S. Guo, R. Meier, H.Y. Chiang, V. Korstgens, J. Wiedersich, J. Perlich, S.V. Roth, P. Müller-Buschbaum, Solvent-Induced Morphology in Polymer-Based Systems for Organic Photovoltaics, *Adv. Funct. Mater.*, 21 (2011) 3382-3391.
- [50] J. Wang, C. Morin, L. Li, A.P. Hitchcock, A. Scholl, A. Doran, Radiation damage in soft X-ray microscopy, *J Electron Spectrosc*, 170 (2009) 25-36.
- [51] D.A. Chen, A. Nakahara, D.G. Wei, D. Nordlund, T.P. Russell, P3HT/PCBM Bulk Heterojunction Organic Photovoltaics: Correlating Efficiency and Morphology, *Nano Letters*, 11 (2011) 561-567.
- [52] L. Willner, A. Poppe, J. Allgaier, M. Monkenbusch, D. Richter, Time-resolved SANS for the determination of unimer exchange kinetics in block copolymer micelles, *Europhys Lett*, 55 (2001) 667-673.
- [53] N.N. Pellegrini, R.J. Composto, K.I. Winey, Investigating polymer blend miscibility with forward recoil spectrometry, *J. Polym. Sci., Part B: Polym. Phys.*, 38 (2000) 1547-1552.
- [54] P. Müller-Buschbaum, E. Metwalli, J.F. Moulin, V. Kudryashov, M. Haese-Seiller, R. Kampmann, Time of flight grazing incidence small angle neutron scattering, *The European Physical Journal Special Topics*, 167 (2009) 107-112.
- [55] J.S. Moon, J.K. Lee, S. Cho, J. Byun, A.J. Heeger, "Columnlike" Structure of the Cross-Sectional Morphology of Bulk Heterojunction Materials, *Nano Letters*, 9 (2009) 230-234.
- [56] C. Wang, D.H. Lee, A. Hexemer, M.I. Kim, W. Zhao, H. Hasegawa, H. Ade, T.P. Russell, Defining the Nanostructured Morphology of Triblock Copolymers Using Resonant Soft X-ray Scattering, *Nano Letters*, 11 (2011) 3906-3911.
- [57] A. Hexemer, W. Bras, J. Glossinger, E. Schaible, E. Gann, R. Kirian, A. MacDowell, M. Church, B. Rude, H. Padmore, A SAXS/WAXS/GISAXS beamline with multilayer monochromator, *J. Phys. Conf. Ser.*, 247 (2010) 012007.

- [58] O. Werzer, R. Resel, Model-Independent X-ray Reflectivity Fitting for Structure Analysis of Poly(3-hexylthiophene) Films, *Macromolecules*, 46 (2013) 3529-3533.
- [59] S.H. Kim, S. Natarajan, G.M. Liu, Photochemical synthesis of oligothiophene thin films and nano-patterns in condensed multilayer films of 2,5-diiodothiophene - Effects of surface chemistry of substrates, *Catal Today*, 123 (2007) 104-112.
- [60] O. Dhez, H. Ade, S.G. Urquhart, Calibrated NEXAFS spectra of some common polymers, *J Electron Spectrosc*, 128 (2003) 85-96.
- [61] H. Yan, C. Wang, A.R. McCarn, H. Ade, Accurate and Facile Determination of the Index of Refraction of Organic Thin Films Near the Carbon 1s Absorption Edge, *Phys Rev Lett*, 110 (2013) 177401.
- [62] H. Ade, J. Kirz, S. Hulbert, E. Johnson, E. Anderson, D. Kern, A Scanning Photoelectron Microscope (SPEM) at the NSLS, *Phys. Scri.*, 41 (1990) 737.
- [63] H. Ade, J. Kirz, S. Hulbert, E. Johnson, E. Anderson, D. Kern, Scanning Photoelectron Microscope with a Zone Plate Generated Microprobe, *Nucl. Instr. Meths. in Phys. Res. A*, 291 (1990) 126-131.
- [64] H. Ade, J. Kirz, S.L. Hulbert, E.D. Johnson, E. Anderson, D. Kern, X-ray Spectromicroscopy with a Zone Plate Generated Microprobe, *Appl. Phys. Lett.*, 56 (1990) 1841-1843.
- [65] J. Kirz, H. Ade, E. Anderson, D. Attwood, C. Buckley, S. Hellman, M. Howells, C. Jacobsen, D. Kern, L. S., I. McNulty, M. Oversluizen, H. Rarback, M. Rivers, S. Rothman, D. Sayre, D. Shu, X-ray Microscopy with the NSLS Soft X-ray Undulator, *Phys. Scri.*, T31 (1990) 12-17.
- [66] C.R. McNeill, B. Watts, L. Thomsen, H. Ade, N.C. Greenham, P.C. Dastoor, X-ray microscopy of photovoltaic polyfluorene blends: Relating nanomorphology to device performance, *Macromolecules*, 40 (2007) 3263-3270.
- [67] C.R. McNeill, B. Watts, L. Thomsen, W.J. Belcher, N.C. Greenham, P.C. Dastoor, H. Ade, Evolution of Laterally Phase-Separated Polyfluorene Blend Morphology Studied by X-ray Spectromicroscopy, *Macromolecules*, 42 (2009) 3347-3352.
- [68] B.A. Collins, H. Ade, Quantitative compositional analysis of organic thin films using transmission NEXAFS spectroscopy in an X-ray microscope, *J. Electron. Spectrosc. Relat. Phenom.*, 185 (2012) 119-128.
- [69] M. Dierolf, A. Menzel, P. Thibault, P. Schneider, C.M. Kewish, R. Wepf, O. Bunk, F. Pfeiffer, Ptychographic X-ray computed tomography at the nanoscale, *Nature*, 467 (2010) 436-439.

- [70] H. Ade, C. Wang, A. Garcia, H. Yan, K.E. Sohn, A. Hexemer, G.C. Bazan, T.Q. Nguyen, E.J. Kramer, Characterization of multicomponent polymer trilayers with resonant soft X-ray reflectivity, *Journal of Polymer Science Part B: Polymer Physics*, 47 (2009) 1291-1299.
- [71] C.R. McNeill, H. Ade, Soft X-ray characterisation of organic semiconductor films, *J. Mater. Chem. C*, 1 (2013) 187 - 201.
- [72] H. Ade, Characterization of organic thin films with resonant soft X-ray scattering and reflectivity near the carbon and fluorine absorption edges, *European Physical Journal-Special Topics*, 208 (2012) 305-318.
- [73] H. Yan, C. Wang, A. Garcia, S. Swaraj, Z. Gu, C.R. McNeill, T. Schuettfort, K.E. Sohn, E.J. Kramer, G.C. Bazan, T.-Q. Nguyen, H. Ade, Interfaces in organic devices studied with resonant soft x ray reflectivity, *J. Appl. Phys.*, 110 (2011) 102220.
- [74] T. Araki, H. Ade, J.M. Stubbs, D.C. Sundberg, G. Mitchell, J.B. Kortright, A.L.D. Kilcoyne, Soft X-ray Resonant Scattering of Structured Polymer Nanoparticles, *Appl. Phys. Lett.*, 89 (2006) 124106.
- [75] J.M. Virgili, Y.F. Tao, J.B. Kortright, N.P. Balsara, R.A. Segalman, Analysis of order formation in block copolymer thin films using resonant soft X-ray scattering, *Macromolecules*, 40 (2007) 2092-2099.
- [76] S. Swaraj, C. Wang, H. Yang, B. Watts, J. Lüning, C.R. McNeill, H. Ade, Nanomorphology of Bulk Heterojunction Photovoltaic Thin Films Probed with Resonant Soft X-ray Scattering, *Nano Lett.*, 10 (2010) 2863-2869
- [77] S. Swaraj, C. Wang, T. Araki, G. Mitchell, L. Liu, S. Gaynor, B. Deshmukh, H. Yan, C.R. McNeill, H. Ade, The utility of resonant soft x-ray scattering and reflectivity for the nanoscale characterization of polymers, *The European Physical Journal - Special Topics*, 167 (2009) 121-126.
- [78] C. Wang, A. Hexemer, J. Nasiatka, E.R. Chan, A.T. Young, H.A. Padmore, W.F. Schlotter, J. Lüning, S. Swaraj, B. Watts, E. Gann, H. Yan, H. Ade, Resonant Soft X-ray Scattering of Polymers with a 2D Detector: Initial Results and System Developments at the Advanced Light Source, *IOP Conference Series: Materials Science and Engineering*, 14 (2010) 012016-012016.
- [79] E. Gann, A. Young, B.A. Collins, H. Yan, J. Nasiatka, H.A. Padmore, H. Ade, A. Hexemer, C. Wang, Soft x-ray scattering facility at the advanced light source with real-time data processing and analysis, *Rev. Sci. Instrum.*, 83 (2012) 045110.
- [80] M.A. Brady, G.M. Su, M.L. Chabynyc, Recent progress in the morphology of bulk heterojunction photovoltaics, *Soft Matter*, 7 (2011) 11065-11077.

- [81] A.C. Stuart, J.R. Tumbleston, H. Zhou, W. Li, S. Liu, H. Ade, W. You, Fluorine substituents reduce charge recombination and drive structure and morphology development in polymer solar cells, *J. Am. Chem. Soc.*, (2013) DOI: 10.1021/ja309289u.
- [82] J.R. Tumbleston, A.C. Stuart, E. Gann, H. Yan, B.A. Collins, W. You, H. Ade, Fluorinated polymer yields high organic solar cell performance for wide range of morphologies, *Adv. Funct. Mater.*, (2013) DOI: 10.1002/adfm.201300093.
- [83] L. Yang, J.R. Tumbleston, H. Zhou, H. Ade, W. You, Disentangling the impact of side chains and fluorine substituents of conjugated donor polymers on the performance of photovoltaic blends, *Energy Environ. Sci.*, 6 (2013) 316-326.
- [84] W. Ma, X. Guo, J. Hou, H. Ade, The control of surface and bulk morphology in organic solar cell with additives: Further improvement of Voc and Jsc/FF respectively., (2013) (in preparation).
- [85] W. Ma, X. Guo, J.R. Tumbleston, J. Hou, H. Ade, A novel strategy to design efficient materials: Predictable domain size/purity with polymer/fullerene miscibility in organic solar cells, *JACS*, (2013) (in preparation).
- [86] W. Ma, L. Ye, J. Hou, H. Ade, The roles of interface roughness between donor/acceptor and domain purity in high efficiency BHJ organic solar cells, (2013) (in preparation).
- [87] J.R. Tumbleston, L. Yang, B.A. Collins, A.C. Stuart, E. Gann, W. Ma, W. You, H. Ade, Control of molecular orientation at organic heterojunctions yields high performance solar cells, (2013) (under review).
- [88] H. Yan, B.A. Collins, E. Gann, C. Wang, H. Ade, C.R. McNeill, Correlating the Efficiency and Nanomorphology of Polymer Blend Solar Cells Utilizing Resonant Soft X-ray Scattering, *ACS Nano*, 6 (2012) 677-688.
- [89] J.R. Tumbleston, Y. Liu, E.T. Samulski, R. Lopez, Interplay between Bimolecular Recombination and Carrier Transport Distances in Bulk Heterojunction Organic Solar Cells, *Adv. Energy Mater.*, 2 (2012) 477-486.
- [90] L.C. Sawyer, D.T. Grubb, *Polymer Microscopy*, Chapman and Hill, New York, 1987.
- [91] H. Ade, X. Zhang, S. Cameron, C. Costello, J. Kirz, S. Williams, Chemical Contrast in X-ray Microscopy and Spatially Resolved XANES Spectroscopy of Organic Specimens, *Science*, 258 (1992) 972-975.
- [92] H. Ade, B. Hsiao, X-ray Linear Dichroism Microscopy, *Science*, 262 (1993) 1427-1429.
- [93] X. Zhang, S.D. Hudson, D.M. DeLongchamp, D.J. Gundlach, M. Heeney, I. McCulloch, In-Plane Liquid Crystalline Texture of High-Performance Thienothiophene Copolymer Thin Films, *Advanced Functional Materials*, 20 (2010) 4098-4106.

- [94] N.D. Browning, M.F. Chisholm, S.J. Pennycook, Atomic-Resolution Chemical-Analysis Using a Scanning-Transmission Electron-Microscope, *Nature*, 366 (1993) 143-146.
- [95] O. Glatter, O. Kratky, *Small Angle X-Ray Scattering*, Academic Press, New York, 1982.
- [96] R.J. Roe, *Methods of X-Ray and Neutron Scattering in Polymer Science*, Oxford University Press, New York, 2000.
- [97] N. Stribeck, *X-Ray Scattering of Soft Matter* Springer, Berlin, Berlin, 2007.
- [98] R.F. Pasternack, P.J. Collings, Resonance Light-Scattering - a New Technique for Studying Chromophore Aggregation, *Science*, 269 (1995) 935-939.
- [99] W. Doster, S. Cusack, W. Petry, Dynamical Transition of Myoglobin Revealed by Inelastic Neutron-Scattering, *Nature*, 337 (1989) 754-756.
- [100] S. Lee, M.J. Bluemle, F.S. Bates, Discovery of a Frank-Kasper sigma Phase in Sphere-Forming Block Copolymer Melts, *Science*, 330 (2010) 349-353.
- [101] S. Lee, M.J. Bluemle, F.S. Bates, Discovery of a Frank-Kasper  $\sigma$  Phase in Sphere-Forming Block Copolymer Melts, *Science*, 330 (2010) 349-353.
- [102] Y.S. Ding, S.R. Hubbard, K.O. Hodgson, R.A. Register, S.L. Cooper, Anomalous Small-Angle X-Ray-Scattering from a Sulfonated Polystyrene Ionomer, *Macromolecules*, 21 (1988) 1698-1703.
- [103] B. Guilleaume, J. Blaul, M. Ballauff, M. Wittemann, M. Rehahn, G. Goerigk, The distribution of counterions around synthetic rod-like polyelectrolytes in solution - A study by small-angle X-ray scattering and by anomalous small-angle X-ray scattering, *European Physical Journal E*, 8 (2002) 299-309.
- [104] G.E. Mitchell, B.G. Landes, J. Lyons, B.J. Kern, M.J. Devon, I. Koprinarov, E.M. Gullikson, J.B. Kortright, Molecular bond selective x-ray scattering for nanoscale analysis of soft matter, *Appl. Phys. Lett.*, 89 (2006) 044101.
- [105] H. Ade, A.P. Hitchcock, NEXAFS microscopy and resonant scattering: Composition and orientation probed in real and reciprocal space, *Polymer*, 49 (2008) 643-675.
- [106] C. Wang, T. Araki, H. Ade, Soft x-ray resonant reflectivity of low-Z material thin films, *Appl. Phys. Lett.*, 87 (2005) 214109-214103.
- [107] C. Wang, T. Araki, B. Watts, S. Harton, T. Koga, S. Basu, H. Ade, Resonant Soft X-ray Reflectivity of Organic Thin Films: Capabilities and Limitations, *J. Vac. Sci. Technol. A*, 25 (2007) 575-586.

- [108] B. Watts, S. Swaraj, D. Nordlund, J. Luning, H. Ade, Calibrated NEXAFS Spectra of Common Conjugated Polymers, *J. Chem. Phys.*, 134 (2011) 024702.
- [109] M. Mezger, B. Jérôme, J. Kortright, M. Valvidares, E. Gullikson, A. Giglia, N. Mahne, S. Nannarone, Molecular Orientation in Soft Matter Thin Films Studied by Resonant Soft X-ray Reflectivity, *Phys. Rev. B*, 83 (2011) 155406.
- [110] M.S. Pierce, R.G. Moore, L.B. Sorensen, S.D. Kevan, O. Hellwig, E.E. Fullerton, J.B. Kortright, Quasistatic X-Ray Speckle Metrology of Microscopic Magnetic Return-Point Memory, *Phys. Rev. Lett.*, 90 (2003) 175502.
- [111] S. Eisebitt, J. Lüning, W.F. Schlotter, M. Lorgen, O. Hellwig, W. Eberhardt, J. Stöhr, Lensless imaging of magnetic nanostructures by X-ray spectro-holography, *Nature*, 432 (2004) 885-888.
- [112] H.N. Chapman, A. Barty, M.J. Bogan, S. Boutet, M. Frank, S.P. Hau-Riege, S. Marchesini, B.W. Woods, S. Bajt, H. Benner, R.A. London, E. Plonjes, M. Kuhlmann, R. Treusch, S. Dusterer, T. Tschentscher, J.R. Schneider, E. Spiller, T. Moller, C. Bostedt, M. Hoener, D.A. Shapiro, K.O. Hodgson, D. Van der Spoel, F. Burmeister, M. Bergh, C. Caleman, G. Huldt, M.M. Seibert, F. Maia, R.W. Lee, A. Szoke, N. Timneanu, J. Hajdu, Femtosecond diffractive imaging with a soft-X-ray free-electron laser, *Nature Physics*, 2 (2006) 839-843.
- [113] P. Thibault, M. Dierolf, A. Menzel, O. Bunk, C. David, F. Pfeiffer, High-resolution scanning x-ray diffraction microscopy, *Science*, 321 (2008) 379-382.
- [114] J.H. Underwood, E.M. Gullikson, High-resolution, high-flux, user friendly VLS beamline at the ALS for the 50-1300 eV energy region, *J Electron Spectrosc*, 92 (1998) 265-272.
- [115] K. Nusser, S. Neueder, G.J. Schneider, M. Meyer, W. Pyckhout-Hintzen, L. Willner, A. Radulescu, D. Richter, Conformations of Silica-Poly(ethylene-propylene) Nanocomposites, *Macromolecules*, 43 (2010) 9837-9847.
- [116] T. Warwick, W. McKinney, E. Domning, A. Doran, H. Padmore, An Energy-Stabilized Varied-Line-Space-Monochromator Undulator Beam Line for PEEM Illumination and Magnetic Circular Dichroism, *AIP Conference Proceedings*, 879 (2007) 469-472.
- [117] S. Sasaki, Analyses for a Planar Variably-Polarizing Undulator, *Nucl Instrum Meth A*, 347 (1994) 83-86.
- [118] A.T. Young, E. Arenholz, S. Marks, R. Schlueter, C. Steier, H.A. Padmore, A.P. Hitchcock, D.G. Castner, Variable linear polarization from an X-ray undulator, *J Synchrotron Radiat*, 9 (2002) 270-274.

- [119]R. Gilles, U. Keiderling, P. Strunz, A. Wiedenmann, H. Fuess, Silver behenate as a standard for instrumental resolution and wavelength calibration for small angle neutron scattering, *Mater Sci Forum*, 321-3 (2000) 264-269.
- [120]R. Gilles, U. Keiderling, A. Wiedenmann, Silver behenate powder as a possible low-angle calibration standard for small-angle neutron scattering, *J Appl Crystallogr*, 31 (1998) 957-959.
- [121]J. Ilavsky, Nika - package for 2D area detectors data reduction, in, *Advanced Photon Source*, Chicago, 2011, pp. "Nika" package of 2D -> 1D SAS data reduction macros for Igor Pro.
- [122]H. Ade, A.P. Smith, H. Zhang, G.R. Zhuang, J. Kirz, E. Rightor, A. Hitchcock, X-ray Spectromicroscopy of Polymers and Tribological Surfaces at Beamline X1A at the NSLS, *J. Electron Spectrosc. Relat. Phenom.*, 84 (1997) 53-71.
- [123]B. Watts, L. Thomsen, P.C. Dastoor, A simple polarimeter for quantifying synchrotron polarization, *J Electron Spectrosc*, 151 (2006) 208-214.
- [124]K. Boller, R.P. Haelbich, H. Hogrefe, W. Jark, C. Kunz, Investigation of Carbon Contamination of Mirror Surfaces Exposed to Synchrotron Radiation, *Nucl Instrum Methods*, 208 (1983) 273-279.
- [125]T. Koide, S. Sato, T. Shidara, M. Niwano, M. Yanagihara, A. Yamada, A. Fujimori, A. Mikuni, H. Kato, T. Miyahara, Investigation of Carbon Contamination of Synchrotron Radiation Mirrors, *Nucl Instrum Meth A*, 246 (1986) 215-218.
- [126]P. Instruments, PI-MTE, in, 2011.
- [127]W. Chen, T. Xu, F. He, W. Wang, C. Wang, J. Strzalka, Y. Liu, J. Wen, D.J. Miller, J. Chen, K. Hong, L. Yu, S.B. Darling, Hierarchical Nanomorphologies Promote Exciton Dissociation in Polymer/Fullerene Bulk Heterojunction Solar Cells, *Nano Letters*, 11 (2011) 3707-3713.
- [128]R.W.C. Hansen, M. Bissen, D. Wallace, J. Wolske, T. Miller, Ultraviolet/Ozone Cleaning of Carbon-Contaminated Optics, *Appl. Opt.*, 32 (1993) 4114-4116.
- [129]M. Malinowski, P. Grunow, C. Steinhaus, M. Clift, L. Klebanoff, Use of molecular oxygen to reduce EUV-induced carbon contamination of optics, *Emerging Lithographic Technologies V*, 4343 (2001) 347-356.
- [130]E.D. Johnson, R.F. Garrett, *In situ* reactive cleaning of X-ray optics by glow discharge, *Nucl. Instr. Method.*, A266 (1988) 381.

- [131]D. Papineau, B.T. De Gregorio, G.D. Cody, J. O'Neil, A. Steele, R.M. Stroud, M.L. Fogel, Young poorly crystalline graphite in the >3.8-Gyr-old Nuvvuagittuq banded iron formation, *Nature Geosci*, 4 (2011) 376-379.
- [132]B. Van Waeyenberge, A. Puzic, H. Stoll, K.W. Chou, T. Tyliczszak, R. Hertel, M. Fähnle, H. Brückl, K. Rott, G. Reiss, I. Neudecker, D. Weiss, C.H. Back, G. Schütz, Magnetic vortex core reversal by excitation with short bursts of an alternating field, *Nature*, 444 (2006) 461-464.
- [133]S. Zhu, Y. Liu, M.H. Rafailovich, J. Sokolov, D. Gersappe, D.A. Winesett, H. Ade, Confinement Induced Miscibility in Polymer Blends, *Nature*, 400 (1999) 49-51.
- [134]C.K. Boyce, M.A. Zwieniecki, G.D. Cody, C. Jacobsen, S. Wirick, A.H. Knoll, N.M. Holbrook, Evolution of xylem lignification and hydrogel transport regulation, *P Natl Acad Sci USA*, 101 (2004) 17555-17558.
- [135]D. Zhu, M. Guizar-Sicairos, B. Wu, A. Scherz, Y. Acremann, T. Tyliczszak, P. Fischer, N. Friedenberger, K. Ollefs, M. Farle, J.R. Fienup, J. Stöhr, High-Resolution X-Ray Lensless Imaging by Differential Holographic Encoding, *Phys Rev Lett*, 105 (2010) 043901-043901.
- [136]E. Pavlopoulou, S.H. Anastasiadis, J.B. Kortright, W. Bras, G. Portale, Investigation of the Micellization in Thin Films Using Resonant Soft X-Ray Scattering, *IOP Conference Series: Materials Science and Engineering*, 14 (2010) 012017.
- [137]H. Yan, C. Wang, A.R. McCarn, H. Ade, A practical and accurate method for determining the index of refraction of organic thin films near the carbon 1s absorption edge, *Phys. Rev. Lett.*, 110 (2013) 177401.
- [138]J.D. Jackson, *Classical Electrodynamics*, New York: Wiley, 1975.
- [139]Z. Jiang, D.R. Lee, S. Narayanan, J. Wang, S.K. Sinha, Waveguide-enhanced grazing-incidence small-angle x-ray scattering of buried nanostructures in thin films, *Phys Rev B*, 84 (2011).
- [140]A.J. Parnell, A.J. Cadby, O.O. Mykhaylyk, A.D.F. Dunbar, P.E. Hopkinson, A.M. Donald, R.A.L. Jones, Nanoscale Phase Separation of P3HT PCBM Thick Films As Measured by Small-Angle X-ray Scattering, *Macromolecules*, 44 (2011) 6503-6508.
- [141]D. Deirmendjian, *Electromagnetic scattering on spherical polydispersions*, American Elsevier Pub. Co., New York,, 1969.
- [142]J.W. Kiel, A.P.R. Eberle, M.E. Mackay, Nanoparticle Agglomeration in Polymer-Based Solar Cells, *Phys. Rev. Lett.*, 105 (2010) 168701.

- [143] Y. Vaynzof, D. Kabra, L.H. Zhao, L.L. Chua, U. Steiner, R.H. Friend, Surface-Directed Spinodal Decomposition in Poly[3-hexylthiophene] and C-61-Butyric Acid Methyl Ester Blends, *Acs Nano*, 5 (2011) 329-336.
- [144] W. Ma, J.R. Tumbleston, M. Wang, E. Gann, F. Huang, H. Ade, Domain purity, miscibility, and molecular orientation at donor/acceptor interfaces in high performance organic solar cells: Paths to further improvement, *Adv. Energy Mater.*, (2013) DOI: 10.1002/aenm.201200912.
- [145] M. Teubner, R. Strey, Origin of the scattering peak in microemulsions, *J. Chem. Phys.*, 87 (1987) 3195-3200.
- [146] C. Wang, D.H. Lee, A. Hexemer, M.I. Kim, W. Zhao, H. Hasegawa, H. Ade, T.P. Russell, Defining the Nanostructured Morphology of Triblock Copolymers Using Resonant Soft X-ray Scattering, *Nano Letters*, 11 (2011) 3906-3911.
- [147] C. Guo, D.R. Kozub, S.V. Kesava, C. Wang, A. Hexemer, E.D. Gomez, Signatures of Multiphase Formation in the Active Layer of Organic Solar Cells from Resonant Soft X-ray Scattering, *Acs Macro Lett*, 2 (2013) 185-189.
- [148] E.L. Huston, J.W. Cahn, J.E. Hilliard, Spinodal Decomposition during Continuous Cooling, *Acta Metall Mater*, 14 (1966) 1053-&.
- [149] J.W. Cahn, J.E. Hilliard, On the Equilibrium Segregation at a Grain Boundary, *Acta Metall Mater*, 7 (1959) 219-221.
- [150] J.W. Cahn, J.E. Hilliard, Free Energy of a Nonuniform System .1. Interfacial Free Energy, *J Chem Phys*, 28 (1958) 258-267.
- [151] B.P. Lyons, N. Clarke, C. Groves, The relative importance of domain size, domain purity and domain interfaces to the performance of bulk-heterojunction organic photovoltaics, *Energy Environ. Sci.*, 5 (2012) 7657-7663.
- [152] Y.R. Shen, Surface-Properties Probed by 2nd-Harmonic and Sum-Frequency Generation, *Nature*, 337 (1989) 519-525.
- [153] M. Born, E. Wolf, Principles of optics : electromagnetic theory of propagation, interference and diffraction of light, Pergamon Press, Oxford ; New York, 1980.
- [154] H. Sirringhaus, Mobility enhancement in conjugated polymer field-effect transistors through chain alignment in a liquid-crystalline phase, *Appl. Phys. Lett.*, 77 (2000) 406.
- [155] L. Pasquali, F. Terzi, R. Seeber, B.P. Doyle, S. Nannarone, Adsorption geometry variation of 1,4-benzenedimethanethiol self-assembled monolayers on Au(111) grown from the vapor phase, *J Chem Phys*, 128 (2008).

- [156] C.H. Wang, S. Mukherjee, A.K.M.M. Islam, Y.W. Yang, M. Mukherjee, Role of Interfacial Interaction in Orientation of Poly(N-isopropylacrylamide) Chains on Silicon Substrate, *Macromolecules*, 44 (2011) 5750-5757.
- [157] B. O'Connor, R.J. Kline, B.R. Conrad, L.J. Richter, D. Gundlach, M.F. Toney, D.M. DeLongchamp, Anisotropic Structure and Charge Transport in Highly Strain-Aligned Regioregular Poly(3-hexylthiophene), *Advanced Functional Materials*, 21 (2011) 3697-3705.
- [158] U. Frisch, B. Hasslacher, Y. Pomeau, Lattice-Gas Automata for the Navier-Stokes Equation, *Phys Rev Lett*, 56 (1986) 1505-1508.
- [159] H.D. Chen, S.Y. Chen, W.H. Matthaeus, Recovery of the Navier-Stokes Equations Using a Lattice-Gas Boltzmann Method, *Phys Rev A*, 45 (1992) R5339-R5342.
- [160] Y.H. Qian, D. Dhumieres, P. Lallemand, Lattice Bgk Models for Navier-Stokes Equation, *Europhys Lett*, 17 (1992) 479-484.
- [161] X.Y. He, L.S. Luo, Theory of the lattice Boltzmann method: From the Boltzmann equation to the lattice Boltzmann equation, *Phys Rev E*, 56 (1997) 6811-6817.
- [162] X.W. Shan, H.D. Chen, Lattice Boltzmann Model for Simulating Flows with Multiple Phases and Components, *Phys Rev E*, 47 (1993) 1815-1819.
- [163] K.N. Premnath, J. Abraham, Three-dimensional multi-relaxation time (MRT) lattice-Boltzmann models for multiphase flow, *J Comput Phys*, 224 (2007) 539-559.
- [164] M.L. Porter, E.T. Coon, Q. Kang, J.D. Moulton, J.W. Carey, Multicomponent interparticle-potential lattice Boltzmann model for fluids with large viscosity ratios, *Phys Rev E*, 86 (2012).
- [165] N. Gonzalez-Segredo, M. Nekovee, P.V. Coveney, Three-dimensional lattice-Boltzmann simulations of critical spinodal decomposition in binary immiscible fluids, *Phys Rev E*, 67 (2003).
- [166] T. Kowalewski, K.A. Singh, T. Young, R.D. McCullough, L.M. Porter, Planarization of Polymeric Field-Effect Transistors: Improvement of Nanomorphology and Enhancement of Electrical Performance, *Advanced Functional Materials*, 20 (2010) 2216-2221.
- [167] B.A. Collins, Z. Li, C.R. McNeill, H. Ade, Fullerene-dependent miscibility in the silole-containing copolymer PSBTBT-08, *Macromolecules*, 44 (2011) 9747-9751.
- [168] A. Gadisa, J.R. Tumbleston, D.H. Ko, M. Aryal, R. Lopez, E.T. Samulski, The role of solvent and morphology on miscibility of methanofullerene and poly(3-hexylthiophene), *Thin Solid Films*, 520 (2012) 5466-5471.

- [169]X. He, B.A. Collins, B. Watts, H. Ade, C.R. McNeill, Studying polymer/fullerene intermixing and miscibility in laterally-patterned films with x-ray spectromicroscopy, *Small*, 8 (2012) 1920–1927.
- [170]W.A. Goddard, *Advances in Quantum-Chemistry and Molecular-Dynamics - Applications to Catalysis and Materials*, Abstr Pap Am Chem S, 203 (1992) 14-Catl.
- [171]K.P. Hermann, L. G. M.; Casida, M. E.; Daul, C.; Goursot, A.; Koester, A.; Proynov, E.; St-Amant, A.; Salahub, D. R.; Contributing authors: Carravetta, V.; Duarte, H.; Friedrich, C.; Godbout, N.; Guan, J.; Jamorski, C.; Leboeuf, M.; Leetmaa, M.; Nyberg, M.; Patchkovskii, S.; Pedocchi, L.; Sim, F.; Triguero, L.; Vela, A., StoBe-deMon version 3.0, in, 2007.
- [172]N. Godbout, D.R. Salahub, J. Andzelm, E. Wimmer, Optimization of Gaussian-Type Basis-Sets for Local Spin-Density Functional Calculations .1. Boron through Neon, Optimization Technique and Validation, *Can J Chem*, 70 (1992) 560-571.
- [173]J.C. Slater, *Advances in Quantum Chemistry*, Academic, New York, 1972.
- [174]S. Huzinaga, Gaussian-Type Functions for Polyatomic Systems .I., *J Chem Phys*, 42 (1965) 1293-&.
- [175]S.K. Sinha, M. Tolan, A. Gibaud, Effects of partial coherence on the scattering of x rays by matter, *Phys Rev B*, 57 (1998) 2740-2758.
- [176]S.J. Fang, S. Haplepete, W. Chen, C.R. Helms, H. Edwards, Analyzing atomic force microscopy images using spectral methods, *J Appl Phys*, 82 (1997) 5891-5898.
- [177]M.J. Lee, D. Gupta, N. Zhao, M. Heeney, I. McCulloch, H. Sirringhaus, Anisotropy of Charge Transport in a Uniaxially Aligned and Chain-Extended, High-Mobility, Conjugated Polymer Semiconductor, *Advanced Functional Materials*, 21 (2011) 932-940.
- [178]H. Lüth, *Solid surfaces, interfaces and thin films*, 5th ed., Springer, Heidelberg ; New York, 2010.
- [179]S.J. Haigh, A. Gholinia, R. Jalil, S. Romani, L. Britnell, D.C. Elias, K.S. Novoselov, L.A. Ponomarenko, A.K. Geim, R. Gorbachev, Cross-sectional imaging of individual layers and buried interfaces of graphene-based heterostructures and superlattices, *Nature Materials*, 11 (2012) 764-767.
- [180]T.R. Albrecht, P. Grutter, D. Horne, D. Rugar, Frequency-Modulation Detection Using High-Q Cantilevers for Enhanced Force Microscope Sensitivity, *J Appl Phys*, 69 (1991) 668-673.

- [181] J.W. Kiel, B.J. Kirby, C.F. Majkrzak, B.B. Maranville, M.E. Mackay, Nanoparticle concentration profile in polymer-based solar cells, *Soft Matter*, 6 (2010) 641-646.
- [182] P. Gupta, A.K. Sinha, M.H. Modi, S.M. Gupta, P.K. Gupta, S.K. Deb, Resonant soft X-ray reflectivity as a sensitive probe to investigate polished zinc sulphide surface, *Appl Surf Sci*, 257 (2010) 210-214.
- [183] S.K. Sinha, X-Ray Diffuse-Scattering as a Probe for Thin-Film and Interface Structure, *J Phys Iii*, 4 (1994) 1543-1557.
- [184] G. Renaud, R. Lazzari, F. Leroy, Probing surface and interface morphology with Grazing Incidence Small Angle X-Ray Scattering, *Surface Science Reports*, 64 (2009) 255-380.
- [185] G. Renaud, R. Lazzari, C. Revenant, A. Barbier, M. Noblet, O. Ulrich, F. Leroy, J. Jupille, Y. Borensztein, C.R. Henry, J.P. Deville, F. Scheurer, J. Mane-Mane, O. Fruchart, Real-time monitoring of growing nanoparticles, *Science*, 300 (2003) 1416-1419.
- [186] J.P. Simon, O. Lyon, D. Defontaine, A Comparison of the Merits of Isotopic-Substitution in Neutron Small-Angle Scattering and Anomalous X-Ray-Scattering for the Evaluation of Partial Structure Functions in a Ternary Alloy, *J Appl Crystallogr*, 18 (1985) 230-236.
- [187] P. Andreatza, H. Khelfane, O. Lyon, C. Andreatza-Vignolle, A.Y. Ramos, M. Samah, Trends in anomalous small-angle X-ray scattering in grazing incidence for supported nanoalloyed and core-shell metallic nanoparticles, *European Physical Journal-Special Topics*, 208 (2012) 231-244.
- [188] M.A. Ruderer, C. Wang, E. Schaible, A. Hexemer, T. Xu, P. Müller-Buschbaum, Morphology and Optical Properties of P3HT:MEH-CN-PPV Blend Films, *Macromolecules*, (2013).
- [189] M. Tolan, X-ray scattering from soft-matter thin films : materials science and basic research, Springer, Berlin ; New York, 1999.
- [190] H. Yan, T. Schuettfort, C.R. McNeill, H.W. Ade, Correlation of interfacial width and device characteristics in thin film transistors based on P(NDI2OD-T2), *Appl. Phys. Lett.*, 101 (2012) 093308.
- [191] I. McCulloch, M. Heeney, C. Bailey, K. Genevicius, M. I. M. Shkunov, D. Sparrowe, S. Tierney, R. Wagner, W.M. Zhang, M.L. Chabinyc, R.J. Kline, M.D. McGehee, M.F. Toney, Liquid-crystalline semiconducting polymers with high charge-carrier mobility, *Nature Materials*, 5 (2006) 328-333.
- [192] D.M. DeLongchamp, R.J. Kline, D.A. Fischer, L.J. Richter, M.F. Toney, Molecular Characterization of Organic Electronic Films, *Adv Mater*, 23 (2011) 319-337.

- [193] T. Schuettfort, B. Watts, L. Thomsen, M. Lee, H. Sirringhaus, C.R. McNeill, Microstructure of Polycrystalline PBTBT Films: Domain Mapping and Structure Formation, *Acs Nano*, 6 (2012) 1849-1864.
- [194] G. Li, R. Zhu, Y. Yang, Polymer solar cells, *Nature Photonics*, 6 (2012) 153-161.
- [195] J. Mannhart, D.G. Schlom, Oxide Interfaces-An Opportunity for Electronics, *Science*, 327 (2010) 1607-1611.
- [196] P. Zubko, S. Gariglio, M. Gabay, P. Ghosez, J.M. Triscone, Interface Physics in Complex Oxide Heterostructures, *Annu Rev Condens Ma P*, 2 (2011) 141-165.
- [197] L. Britnell, R.V. Gorbachev, R. Jalil, B.D. Belle, F. Schedin, A. Mishchenko, T. Georgiou, M.I. Katsnelson, L. Eaves, S.V. Morozov, N.M.R. Peres, J. Leist, A.K. Geim, K.S. Novoselov, L.A. Ponomarenko, Field-Effect Tunneling Transistor Based on Vertical Graphene Heterostructures, *Science*, 335 (2012) 947-950.
- [198] H. Yang, J. Heo, S. Park, H.J. Song, D.H. Seo, K.E. Byun, P. Kim, I. Yoo, H.J. Chung, K. Kim, Graphene Barristor, a Triode Device with a Gate-Controlled Schottky Barrier, *Science*, 336 (2012) 1140-1143.
- [199] T. Kerle, Z.Q. Lin, H.C. Kim, T.P. Russell, Mobility of polymers at the air/polymer interface, *Macromolecules*, 34 (2001) 3484-3492.
- [200] Y.S. Seo, T. Koga, J. Sokolov, M.H. Rafailovich, M. Tolan, S. Sinha, Deviations from liquidlike behavior in molten polymer films at interfaces, *Phys Rev Lett*, 94 (2005) 157802.
- [201] M. Salluzzo, S. Gariglio, X. Torrelles, Z. Ristic, R. Di Capua, J. Drnec, M.M. Sala, G. Ghiringhelli, R. Felici, N.B. Brookes, Structural and Electronic Reconstructions at the LaAlO<sub>3</sub>/SrTiO<sub>3</sub> Interface, *Adv Mater*, 25 (2013) 2333-2338.
- [202] A.F. Santander-Syro, O. Copie, T. Kondo, F. Fortuna, S. Pailhes, R. Weht, X.G. Qiu, F. Bertran, A. Nicolaou, A. Taleb-Ibrahimi, P. Le Fevre, G. Herranz, M. Bibes, N. Reyren, Y. Apertet, P. Lecoeur, A. Barthelemy, M.J. Rozenberg, Two-dimensional electron gas with universal subbands at the surface of SrTiO<sub>3</sub>, *Nature*, 469 (2011) 189-193.
- [203] W. Meevasana, P.D.C. King, R.H. He, S.K. Mo, M. Hashimoto, A. Tamai, P. Songsiriritthigul, F. Baumberger, Z.X. Shen, Creation and control of a two-dimensional electron liquid at the bare SrTiO<sub>3</sub> surface, *Nature Materials*, 10 (2011) 114-118.